

A methodology to reproduce postbuckling in composite panels to study skin stringer separation

Kootte, Luc

DOI

[10.4233/uuid:cfccc1dc-df8a-4a49-8c1a-c2ebad7a1867](https://doi.org/10.4233/uuid:cfccc1dc-df8a-4a49-8c1a-c2ebad7a1867)

Publication date

2023

Document Version

Final published version

Citation (APA)

Kootte, L. (2023). *A methodology to reproduce postbuckling in composite panels to study skin stringer separation*. [Dissertation (TU Delft), Delft University of Technology]. <https://doi.org/10.4233/uuid:cfccc1dc-df8a-4a49-8c1a-c2ebad7a1867>

Important note

To cite this publication, please use the final published version (if applicable). Please check the document version above.

Copyright

Other than for strictly personal use, it is not permitted to download, forward or distribute the text or part of it, without the consent of the author(s) and/or copyright holder(s), unless the work is under an open content license such as Creative Commons.

Takedown policy

Please contact us and provide details if you believe this document breaches copyrights. We will remove access to the work immediately and investigate your claim.



TU Delft

Luc Kootte

A methodology

to reproduce

postbuckling

in composite

panels to study

skin-stringer

separation

A methodology to reproduce postbuckling in composite panels to study skin-stringer separation

Luc Kootte

A METHODOLOGY TO STUDY SKIN-STRINGER SEPARATION IN COMPOSITE PANELS DUE TO POSTBUCKLING CONDITIONS

Dissertation

for the purpose of obtaining the degree of doctor
at Delft University of Technology
by the authority of the Rector Magnificus Prof. dr. ir. T.H.J.J. van der Hagen
chair of the Board for Doctorates
to be defended publicly on
Friday 7 July 2023 at 10:00 o'clock

by

Lucas Johan KOOTTE

Master of Science in Aerospace Engineering, Delft University of Technology, the
Netherlands
born in Breda, the Netherlands.

This dissertation has been approved by the promotor.

Composition of the doctoral committee:

Rector Magnificus,	chairperson
Prof. dr. C. Bisagni,	Delft University of Technology, promotor
Prof. dr. C. Kassapoglou,	Delft University of Technology, promotor

Independent members:

Prof.dr.ir. L.J. Sluys	Delft University of Technology
Prof.dr. C.A. Featherston	Cardiff University, UK
Prof.dr. B. Castanié	INSA Toulouse, France
Dr. C.G. Dávila	NASA Langley, USA
Prof.dr.ir. R. Benedictus	Delft University of Technology, reserve member

Other members:

Dr. V. Ranatunga	AFRL Wright Patterson AFB, USA
------------------	--------------------------------

The advancement of research presented in this dissertation is sponsored by the Air Force Research Laboratory (AFRL) and the European Office of Aerospace Research and Development (EOARD) of the United States Air Force.



Keywords: Skin-stringer separation, Building block approach, Stiffened panels, Post-buckling, Thermoset composites, Fracture toughness, Component testing

Printed by: Gildeprint

Cover: Designed by Luc Kootte. A composition of all the specimens that were manufactured and tested by the author.

Copyright © 2023 by L.J. Kootte
ISBN 978-94-6366-703-6

An electronic version of this dissertation is available at
<http://repository.tudelft.nl/>.

*Ik draag mijn thesis op aan mijn oudste broer Bob en schoonzus Nienke,
omdat ik weet hoe trots jullie zouden zijn.*

CONTENTS

Summary	ix
Samenvatting	xiii
1 Introduction	1
1.1 State of the art	2
1.1.1 Building block pyramid	2
1.1.2 Initiation and onset of delaminations	5
1.1.3 Material characterization for interface delamination	6
1.1.4 Skin-stringer separation testing and modelling	6
1.1.5 Summary list of technological gaps	8
1.2 Dissertation outline	8
2 Methodology	11
2.1 Introduction of the overall approach	12
2.2 Building block pyramid	13
2.3 Numerical framework	15
2.3.1 Meshing structural and interface elements	15
2.3.2 Load cases and test configurations	21
2.3.3 Analyses and post-processing	26
2.4 A configuration to approximate the postbuckling shape	33
2.5 Preparations and procedures for testing	35
2.5.1 Manufacturing	35
2.5.2 An adaptive multi-point test equipment	37
2.5.3 Test procedure	39
2.5.4 Measurement techniques	39
2.6 Case study	42
2.6.1 Properties	42
2.6.2 Design	43
3 Coupon tests for cross-ply interface characterization	45
3.1 Introduction	46
3.2 Coupon design and manufacturing	46
3.3 Coupon testing	49
3.3.1 Mode I: Double Cantilever Beam	49
3.3.2 Mode II: End-Notched Flexure	52
3.3.3 Mode I+II: Mixed-Mode Bending	55
3.3.4 Investigation of the delamination surface of the coupon specimens	59
3.3.5 Overview of the coupon test results and mixed-mode relation	60

3.4	Determination of the trilinear law	61
3.4.1	The critical fracture toughness	62
3.4.2	The secondary mode I interface strength	63
3.4.3	The secondary mode I penalty stiffness.	64
3.4.4	The secondary mode II interface strength and stiffness	65
3.5	Final properties	66
3.6	Discussion	67
3.6.1	Mixed-mode implementation of the trilinear law.. . . .	67
3.6.2	Mode II secondary interface strength effect on mixed-mode trilinear law.	68
3.6.3	Mode II interface toughness effect on mixed-mode trilinear law.	69
3.6.4	Discussion on the validity of the constant mixed-mode assumption	69
3.7	Conclusion.	71
4	A semi-analytical approach to identify initiation of bending separation	73
4.1	Introduction	74
4.2	The semi-analytical approach	74
4.3	Implementation and verification of the semi-analytical criterion	77
4.3.1	Representative verification model	77
4.3.2	Finite element implementation	79
4.3.3	Mesh sensitivity of the semi-analytical criterion	81
4.3.4	Verification of the criterion against cohesive initiation	83
4.4	Initiation of separation in a four-stringer panel.	84
4.4.1	Thick stringer panel: bending failure	85
4.4.2	Thin stringer panel: twisting failure	88
4.5	Conclusions	91
5	A seven-point bending configuration to capture skin-stringer separation	93
5.1	Introduction	94
5.2	Determining the single-stringer specimen configuration	94
5.3	Predicting separation through cohesive zone modelling	97
5.4	Testing of skin-stringer separation	103
5.5	Numerical-experimental comparison.	108
5.6	Initiation and propagation of separation in the four-stringer panel.	110
5.6.1	Initiation of separation and force/moment distribution.	111
5.6.2	Propagation and shape of separation.. . . .	113
5.7	Conclusions	115
6	A four-point twisting configuration to capture skin-stringer separation	117
6.1	Introduction	118
6.2	Single-stringer specimen design	118
6.3	Predicting skin-stringer separation through cohesive zone modelling	120
6.4	Testing of the skin-stringer separation	124
6.5	Numerical-experimental comparison.	131
6.6	Initiation and propagation of separation in the four-stringer panel.	133
6.6.1	Initiation of separation and force/moment distribution	133
6.6.2	Propagation and shape of separation	135

6.7	Conclusions	137
7	Conclusions and recommendations	139
7.1	Conclusions	140
7.2	Observations throughout the building block pyramid	142
7.3	Recommendations for future research	143
	Bibliography	145
	Glossary	157
	List of Publications	159
	Acknowledgments	161
	Biographical note	165

SUMMARY

Using composite materials in the design of an aircraft structure has the potential to reduce weight compared to using more conventional metals. Yet, the aircraft's weight can be reduced even further if more of the material's load-carrying capabilities are utilised. Commonly, skin buckling, where the skin between stringers deforms out of their plane in a wavelike manner, is often avoided as it has the possibility to lead to structural collapse. One common cause of the collapse in stiffened panels can be the separation of stringers from the skin due to postbuckling deformations. To allow buckling, first, a better understanding of the interaction between buckling deformations and material failure during skin-stringer separation is required.

A building block pyramid is used to design a composite aircraft structure, combining tests and analyses, using stiffened panels, single-stringer specimens and coupons. Analyzing postbuckling-induced failure can be costly, especially when manufacturing and testing stiffened panels. Numerical models can aid in reducing experimental costs, but these models still take considerable time to develop, verify, and execute. Separation is complex, involving matrix cracks, fibre bridges, and delamination migrations. This thesis covers these three levels of the building block approach and expands on the single-stringer level, as relevant tests that cover postbuckling-induced skin-stringer separation have not been standardized. First, a material characterization is performed on the coupon level. These properties are applied to a stiffened panel model to identify critical postbuckling regions. Then a single-stringer specimen is designed that combines the material complexities of the coupon level and the geometrical complexities of the panel by mimicking the postbuckling shape.

The fracture toughness of the interface is determined through coupon tests. In this thesis, the coupon design represents the skin of the panels. The different modes (I: opening, II: sliding, and I+II: mixed-mode) are characterised. It was found that the fracture toughness increases linearly with the delamination length, referred to as the R-curve effect, until it reaches a steady state. These results are reduced to a set of interface properties that can be used in the numerical models of the single-stringer specimens. An existing method of superposing cohesive elements is adapted to make the toughening behaviour independent of the initiation behaviour. Furthermore, a thermodynamic consistency was added to the superposed set of cohesive elements. The numerical coupon models correlate with the mode I tests but failed for mixed-mode due to changing mixed-mode conditions for long delamination lengths.

Two different panel designs are considered: 1) with the stringer laminate the same thickness as the skin referred to as the thin-stringer design; 2) with the stringer laminate twice the thickness of the skin referred to as the thick-stringer design. An energy-based criterion in a semi-analytical framework is designed to predict initiation of separation in these panels. The input of the criterion, mainly the bending moment, is taken from the output of the finite element models to calculate the strain energy release rate. For

a panel with four thicker stringers, the criterion indicates that separation occurs at the maximum out-of-plane deformation, away from the stringer flange. In a panel with four thin stringers, separation did not occur due to bending of the skin. A cohesive model showed that separation can occur due to twisting at the inflection points of a postbuckling wave.

The region of a multi-stringer panel where separation might occur is approximated using the single-stringer specimen in an adaptive multi-point test configuration. Out-of-plane loads directly impose a postbuckling-like deformation via a set of supports and load points. By studying the placement of these points, a configuration can be obtained that best represents the actual postbuckling shape. Two segments of a postbuckling wave can be identified: the minima of the wave, where skin bending occurs, and the inflection point between the minima and maxima of the wave, where there is skin twisting. By changing the number of points in the test configuration, either a region of high bending via a seven-point bending configuration or high twisting via a four-point twisting configuration can be imitated.

For the thick-stringer panel, a single-stringer specimen in a seven-point bending configuration is designed. Separation is studied using a combination of numerical models and experimental tests. Initiation of separation is captured by the maximum force in the central support normalized to the total applied load. The subsequent separation growth can be approximated with an ellipse to quantify the separation response. During testing, the load distribution is monitored through load cells, the deformation through digital image correlation and the interface separation with C-scan. When the separation size is above 50% of the total flange width, separation tends to become unstable. The separation shapes predicted by the numerical models resemble those obtained from the C-scan. However, in the tests, delamination migration, where the path of separation growth is perpendicular to the adjacent fibres, influences the elliptical shape. These results provide insight into the behaviour of the panel. The energy-based semi-analytical criterion to identify initiation can be adapted from these single-stringer specimen results. Instead of energy-based, the maximum bending moment observed in the skin of the single-stringer specimen is used as the allowable, resulting in an improved indication of initiation. Furthermore, it can be illustrated again that the bending and twisting moment distribution in the single-stringer specimen matched the panel and, consequently, as was observed, the resulting separation shape.

The approach is repeated for the thin-stringer design, where a four-point twisting configuration is developed to reproduce the inflection point between the minimum and maximum of a buckling halfwave. The edge crack torsion test for mode III interface characterisation is used as a basis for the design strategy. Two supports and load points in opposing corners create this anti-symmetric deformation shape. Separation in the numerical models with cohesive elements is primarily due to mode II+III. The pure twisting separation also follows an elliptical shape. The same phenomena are observed in the four-point twisting tests. The shape can not directly be compared between the models and tests, but the speed of propagation comparison does show that the currently used interface properties give a conservative prediction of separation. The separation length in the four-stringer panel with cohesive elements was shorter than in the single-stringer specimen for the same separation width. Furthermore, the separation length triggered by

twisting in the thin-stringer panel was much shorter than separation due to bending in the thick-stringer panel, despite the longer halfwaves in the thin-stringer panel.

The guidelines for modelling and testing in the seven-point bending can assist in standardising this test method. Furthermore, the four-point twisting test can be further developed to also be included in the building block pyramid such that bending and twisting separation can be characterised separately. Simultaneously, the numerical and experimental framework is comprehensive and the proposed methodology can aid in the development of structures that can operate past their buckling point. A combination of numerical models and the smaller single-stringer specimens should reduce the cost and development time of such a structure. In the end, if postbuckling is allowed, displacements 3-5x higher than the buckling point can be achieved before skin-stringer separation happens.

SAMENVATTING

Het gebruik van composietmaterialen bij het ontwerp van een vliegtuigconstructie heeft het potentieel om het gewicht te verminderen in vergelijking met het gebruik van meer conventionele metalen. Toch kan het gewicht van het vliegtuig nog verder worden vermindert als het materiaal dichter bij z'n maximum wordt belast. Gewoonlijk wordt huidknik, waarbij de huid tussen verstijvers op een golfachtige manier uit hun vlak vervormt, vermeden omdat dit kan leiden tot structurele instorting. Een veelvoorkomende oorzaak van het instorten van verstijfde panelen kan zijn dat de liggers losraken van de huid als gevolg van postknik-vervormingen. Om knikken mogelijk te maken, is ten eerste een beter begrip van de interactie tussen knikvervormingen en materiaalfalen tijdens het scheiden van de huid en de stringer vereist.

Een bouwsteenpiramide wordt gebruikt om een vliegtuigconstructie te ontwerpen, waarbij testen en modellen worden gecombineerd, waarbij gebruik wordt gemaakt van verstijfde panelen, exemplaren met één verstijver en coupons. Het analyseren van door knikken veroorzaakte falen kan kostbaar zijn, vooral bij het vervaardigen en testen van verstijfde panelen. Numerieke modellen kunnen helpen bij het verlagen van experimentele kosten, maar het kost nog steeds veel tijd om deze modellen te ontwikkelen, te verifiëren en uit te voeren. Loslating is complex en omvat matrixscheuren, vezelbruggen en delaminatiemigraties. Dit proefschrift behandelt deze drie niveaus van de bouwsteenpiramide en breidt het middelste niveau uit, aangezien relevante testen die betrekking hebben op postknik-geïnduceerde huid-verstijver-loslating niet gestandaardiseerd zijn. Eerst wordt een materiaalkarakterisatie uitgevoerd op coupon niveau. Deze eigenschappen worden toegepast op een verstijfd paneel model om kritieke postknik-gebieden te identificeren. Vervolgens wordt een enkelverstijfd paneel ontworpen dat de materiële complexiteit van het couponniveau en de geometrische complexiteit van het paneel combineert door de postknik-vorm na te bootsen.

De breuktaaiheid van de tussenlaag, tussen huid en verstijver, wordt bepaald door middel van coupon testen. In dit proefschrift vertegenwoordigt het coupon ontwerp de huid van de panelen. De verschillende modi (I: openen, II: schuiven en I+II: gemengde modus) worden gekarakteriseerd. De breuktaaiheid neemt lineair toe met de delaminatie lengte, ook wel het R-curve effect genoemd, totdat deze een stabiele toestand bereikt. Deze resultaten zijn teruggebracht tot een reeks tussenlaag eigenschappen die kunnen worden gebruikt in de numerieke modellen van de enkelverstijfde panelen. Een bestaande methode om cohesieve elementen op elkaar te plaatsen is aangepast om het taaiheidsgedrag onafhankelijk te maken van het initiatiegedrag. Bovendien werd een thermodynamische consistentie toegevoegd aan de boven elkaar geplaatste reeks cohesieve elementen. De numerieke couponmodellen correleren met de modus I-tests, maar faalden voor gemengde modus vanwege veranderende omstandigheden voor lange delaminatie lengtes.

Er worden twee verschillende paneel ontwerpen overwogen: 1) met de verstijverlaminaat met dezelfde dikte als de huid waarnaar wordt verwezen als het dunne-verstijver-

ontwerp; 2) met het verstijver-laminaat tweemaal de dikte van de huid, ook wel het dikke verstijver-ontwerp genoemd. Een op energie gebaseerd criterium in een semi-analytisch framework is ontworpen om het begin van loslating in deze panelen te voorspellen. Het criterium gebruikt het buigmoment, berekend door de eindige-elementenmodellen, om de spanningsenergieafgiftesnelheid te berekenen. Voor een paneel met vier dikkere verstijvers geeft het criterium aan dat scheiding optreedt bij de maximale vervorming, weg van de verstijvervoet. Bij een paneel met vier dunne verstijvers trad geen scheiding op door verbuiging van de huid. Een cohesieve model toonde aan dat scheiding kan optreden als gevolg van torsie op de buigpunten van een postknik-golf.

Het gebied van een paneel met meerdere stringers waar scheiding kan optreden, wordt benaderd met behulp van het monster met één stringer in een adaptieve meerpuntstestconfiguratie. Belastingen buiten het vlak leggen direct een postknik-achtige vervorming op via een reeks ondersteuning en belastingspunten. Door de plaatsing van deze punten te bestuderen, kan een configuratie worden verkregen die het beste de daadwerkelijke postknik-vorm weergeeft. Er kunnen twee segmenten van een postknik-golf worden geïdentificeerd: de minima van de golf, waar huidbuiing optreedt, en het buigpunt tussen de minima en maxima van de golf, waar huidverdraaiing optreedt. Door het aantal punten in de testconfiguratie te wijzigen, kan ofwel een gebied met hoge buiging via een zevenpunts buigconfiguratie of een hoge torsie via een vierpunts torsieconfiguratie worden nagebootst.

Voor het paneel met dikke verstijvers is een exemplaar met één verstijver in een zevenpunts buigconfiguratie ontworpen. Scheiding wordt bestudeerd met behulp van een combinatie van numerieke modellen en experimentele tests. Het begin van de loslating wordt vastgelegd door de maximale kracht in de centrale ondersteuningspunt genormaliseerd op de totale uitgeoefende belasting. De daaropvolgende loslatingsgroei kan worden benaderd met een ellips om de scheidingsrespons te kwantificeren. Tijdens het testen wordt de belastingsverdeling gecontroleerd door middel van belastingscellen, de vervorming door middel van digitale beeldcorrelatie en de loslating met C-scan. Wanneer de loslatingsbreedte groter is dan 50% van de totale voetbreedte, heeft de loslating de neiging instabiel te worden. De door de numerieke modellen voorspelde loslatingsvormen lijken op die van de C-scan. In de testen beïnvloedt delaminatie migratie, waarbij het pad van scheidingsgroei loodrecht staat op de aangrenzende vezels, echter de elliptische vorm. Deze resultaten geven inzicht in het gedrag van het paneel. Het op energie gebaseerde semi-analytische criterium om initiatie te identificeren kan worden aangepast aan de hand van de resultaten van deze enkelverstijfde panelen. In plaats van op energie gebaseerd, wordt het maximale buigmoment waargenomen in de huid van het enkelverstijfd paneel gebruikt als het maximale toelaatbare waarde, wat resulteert in een verbeterde indicatie van initiatie. Verder kan opnieuw worden geïllustreerd dat de verdeling van het buig- en torsiemoment in het exemplaar met één verstijver overeenkwam met het paneel en met de resulterende loslatingsvorm.

De benadering wordt herhaald voor het dunne verstijver-ontwerp, waarbij een vierpunts-torsieconfiguratie wordt ontwikkeld om het buigpunt tussen het minimum en het maximum van een halve knikgolf te reproduceren. De edge crack torsion test voor modus III-karakterisering wordt gebruikt als basis voor de ontwerpstrategie. Twee steunpunten en belastingspunten in tegenoverliggende hoeken creëren deze antisymmetrische vervorming. Loslating in de numerieke modellen met cohesieve elementen is voornamelijk te

wijten aan modus II+III. De pure torsie scheiding volgt ook een elliptische vorm. Dezelfde verschijnselen worden ook waargenomen bij de vierpuntstorsie proeven. De vorm kan niet direct worden vergeleken tussen de modellen en tests, maar de vergelijking van de groeisnelheid laat wel zien dat de momenteel gebruikte tussenlaag-eigenschappen een conservatieve voorspelling van de loslating geven. De loslatingslengte in het paneel met vier verstijvers met cohesieve elementen was korter dan in het exemplaar met één verstijver voor dezelfde loslatingsbreedte. Bovendien was de loslatingslengte veroorzaakt door draaien in het paneel met dunne verstijvers veel korter dan de loslating als gevolg van buigen in het paneel met dikke verstijvers, ondanks de langere halve golven in het paneel met dunne verstijvers.

De richtlijnen voor het modelleren en testen in de zevenpuntsbuiging kunnen helpen bij het standaardiseren van deze testmethode. Verder kan de vierpunts torsieproef doorontwikkeld worden om ook opgenomen te worden in de bouwsteenpiramide zodat buiging en torsiescheiding afzonderlijk gekarakteriseerd kunnen worden. Tegelijkertijd is het numerieke en experimentele raamwerk alomvattend en kan de voorgestelde methodologie helpen bij de ontwikkeling van constructies die voorbij hun knikpunt kunnen werken. Een combinatie van numerieke modellen en de kleinere enkelverstijfde panelen zou de kosten en ontwikkelingstijd van een dergelijke structuur moeten verminderen. Uiteindelijk, als postknik is toegestaan, kunnen verplaatsingen 3-5x hoger dan het knikpunt worden bereikt voordat scheiding tussen de huid en de verstijver plaatsvindt.

1

INTRODUCTION

The structural weight of an aircraft is an essential feature; A lower weight can reduce fuel consumption. This increase in efficiency is needed to balance the increasing demand for intercontinental tourism and climate concerns due to emitted greenhouse gases. For the newer generation of aircraft, metal is gradually replaced by composite materials wherever possible. Composite materials can be fully tailored for the applied loads, a fundamental advantage over metals. The most common example of composite material in aircraft structures is a combination of continuous carbon fibre bundles embedded in an epoxy matrix. The carbon epoxy is first formed into a sheet, where the fibres are all in the same plane and oriented in a single direction, called a lamina or ply. The lamina is primarily able to carry the load in the direction of the fibres and is weakest orthogonal to the fibres. When laminae are stacked in different orientations, a laminate is formed that can withstand the forces in all directions for which it is designed. Laminates are often shell-type structures, which means they are thin compared to their in-plane dimensions.

These types of structures can either fail by exceeding strength tolerances or by stability failure. Buckling is a form of stability failure, which occurs when a shell structure is subjected to a high in-plane load[1]. In the postbuckling phase, the out-of-plane displacement can be a few times greater than the in-plane displacement, and is accompanied by a large loss in stiffness. In order to retain the load-carrying capabilities, the shell, often referred to as the skin, is stiffened. The skin between the stringers can still buckle (local buckling), which is illustrated in figure 1.1a, but global buckling events that can lead to the collapse of the structure are prevented. The stringers are also a composite laminate and can be bonded or co-cured to the skin. With co-curing, the skin and stringers are manufactured simultaneously in the autoclave (a pressurized oven), resulting in a continuous structure.

In a stiffened composite structure, excessive local buckling can trigger strength failure. An important failure mode is the formation of delaminations between the skin and stringer that causes skin-stringer separation. When the stringers have separated completely from the skin, the skin is again allowed to go into global buckling, which results in a loss of the load-carrying capacity. [2–8]. Local buckling of the skin produces bending and twisting moments at the edge of the stringers, leading to interlaminar stresses at the skin-stringer interface. Exceeding the stress allowable of the material can cause delamination, a

separation between the laminae. Furthermore, composites have numerous other complex failure mechanisms[9] that interact with delamination, such as fibre kinking[10]/breakage and matrix cracking[11], which are illustrated in figure 1.1b. The combined complexity of buckling and separation[6, 12–14] leads to a design that is not allowed to operate past the buckling load.

"Wide exploitation of advanced composites in stability critical structural designs depends to a large degree on the ability of composites to support loads well beyond the initial buckling level. Unquestionably, the high stiffness-to-weight ratio of composites renders them potentially attractive up to initial buckling. However, since postbuckling design has been established over several decades for certain types of conventional metallic alloy construction, it should be anticipated that composites demonstrate a similar capability."(Chapter 5 page 79 [15])

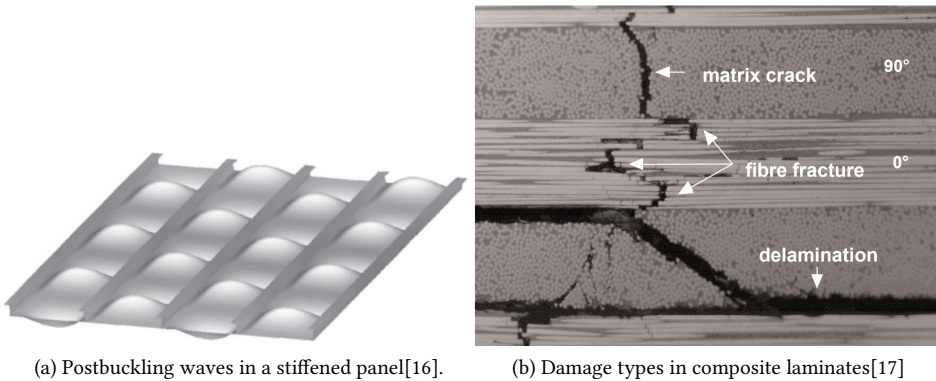


Figure 1.1: a) Postbuckling deformation in a panel typically 100-1000 mm in length, with possible out-of-plane deformations of 1-10 mm; b) common failure modes in (stiffened) composite panels. Generally, the ply thickness is around 0.05-0.2 mm.

A deeper understanding of the interactions between structural and material response is necessary to design aeronautical structures that can operate in postbuckling without the risk of unstable skin-stringer separation. This knowledge must be based on a more precise material and structural characterization that can only be achieved using a combination of advanced numerical methods and experimental evaluations of structural specimens[18].

1.1 STATE OF THE ART

The section on state-of-the-art is divided into the building block approach, analytical criteria for delamination initiation and onset, composite interface characterization, and modelling and testing of skin-stringer separation.

1.1.1 BUILDING BLOCK PYRAMID

A building block approach is used during the development of composite structures following a pyramid such as shown in figure 1.2 presented in the composite military handbook[15]. The essential content of handbook[15] is summarized in this section.

The first three blocks correspond to the development of the material properties. Numerous small coupon tests are performed to obtain the general behaviour of a material system. Most of these tests are part of Block 3. Sometimes a limited number of tests in blocks 4/5 are performed that can dictate further investigation of critical properties in block 3. Due to the small costs of the coupons, properties with statistical significance can be obtained. However, these properties are configuration dependent.

In blocks 4 and 5, design values are developed that correspond to the structure instead of the material itself. However, these may be so specific that they cannot be used for other dissimilar structures. In block 4, the structural elements are used, which is a local structural detail such as a skin with a single stiffener. On these types of structures, crippling, strength failure of a stiffener section, and stiffener pull-off are tested. "Present analytical capability cannot reliably predict this failure mode, and the development of detail test data is essential." [15]

In block 5, more structural detail is added and the subcomponent size and complexity are often larger compared to the elements. At this level, multi-stringer panels in compression are tested, for example. During these tests, load redistribution is considered when a local damage is present. Out-of-plane failure modes are typically assessed here as well.

In the last block, Block 6, a very limited number of tests are performed at the end of the certification process. The results of these tests are primarily used to verify the analytical and numerical models and to verify the design and analysis methodology.

Climbing the pyramid is accompanied by a reduction in number of tests. In block 3, thousands of specimens are tested, in block 4 hundreds, and in block 5 dozens. A good building block approach will limit the amount of full-scale tests that need to be performed. The remaining load cases can be cleared by the numerical analyses or by comparison of element test results.

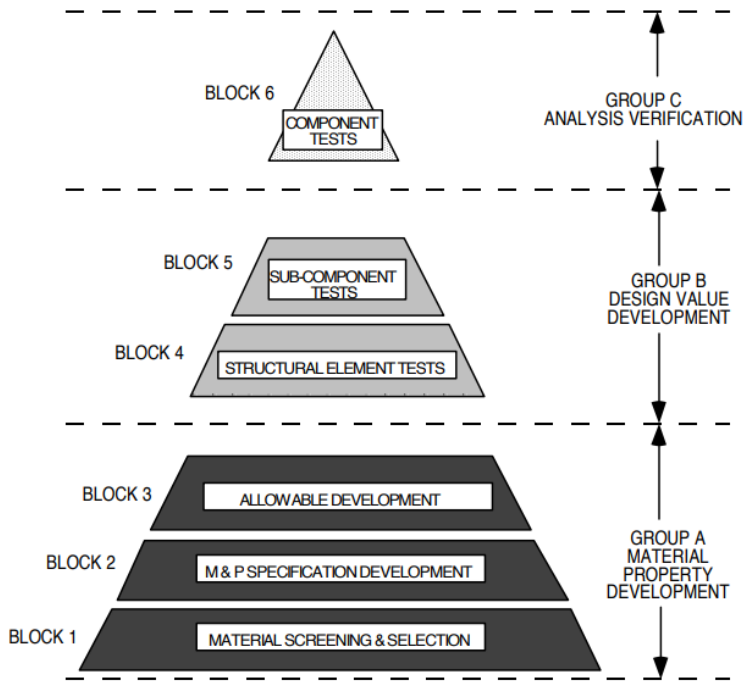


FIGURE 4.4.3.2 Building block approach.

Figure 1.2: Building block approach from the composite handbook for the military (CHM)[15].

1.1.2 INITIATION AND ONSET OF DELAMINATIONS

In order to investigate a wide variety of design configurations to optimize the load-carrying capabilities of the structure fully, it is crucial to have a tool that can quickly assess skin-stringer separation. The design parameters such as structural geometry and dimensions may considerably affect the skin-stringer separation [19, 20]. For example, a change in stringer spacing or stacking sequence can alter the postbuckling deformation and cause a significantly different strain distribution on the panel. Additionally, other factors such as geometrical imperfections of the panel [21] or the conditions that affect the interlaminar normal or shear stresses along the flange edge can delay the separation [22] as well.

The most common failure criterion for initiation of delamination is the quadratic stress criterion [23]; When the strength is exceeded a crack will form. The criterion considers a combination of a normal and a shear stress acting on the matrix. The normal stress allowable is characterized using a transverse tensile test. During this test the matrix is directly loaded until failure, based on the maximum force and the cross-section the allowable can be calculated. For shear a +45/-45 tensile test is used. There is no clear point of failure, instead as a standard the strength at 5% shear strain is taken as the allowable. This strength based criterion only dictates possible formation of cracks, but do not indicate if the cracks will actually propagate.

In an energy based criterion, an initial crack can possibly propagate if a certain energy threshold is exceeded. Cosentino and Weaver [24] based on the work of Williams [25] showed a fracture mechanics approach to predict debonding of the skin and stringer. An analytical method focusing on stringer runout locations was used to obtain the out-of-plane behaviour of a postbuckled stiffened panel. Subsequently the bending moments can be obtained from which the energy components can be calculated. However, fully analytical methods that require the calculation of the postbuckling shape can take time to implement.

The Royal Dutch Aerospace Centre (NLR) proposed a failure criterion that depends directly on the running loads and moments along the stringers of a panel [26, 27]. This criterion was developed using the seven-point bending test introduced by the NLR [28]. The criterion relies on loads and moments calculated using the classical laminate theory with the assumption of no shear strain acting in the longitudinal stringer direction at the skin-stringer interface, because it focuses on the location of high-skin bending. However, only a limited amount of data is available from this study.

Numerical methods exist to determine the initiation of skin-stringer separation, for example, through cohesive zone modelling. How to implement cohesive elements and their theory are discussed in the methodology in section 2.3. However, developing and verifying multi-stringer panel models requires significant time. Furthermore, employing cohesive elements everywhere as the location of initiation is unknown results in a high computational time. Using a global-local approach, the analysis time can be reduced [29–32]. This is done by analyzing a global model of a multi-stringer panel in postbuckling and imposing the local conditions on a smaller model with a cohesive zone model. Although the analysis time is reduced, the model complexity and, therefore, the development time is increased. Especially when also propagation is considered through a two-way approach [33–35], where the stiffness of the global model is updated based on the analysis of the local models.

1.1.3 MATERIAL CHARACTERIZATION FOR INTERFACE DELAMINATION

There are several methods[36] to characterize interlaminar properties of composite lay-ups and can be categorized in three separate modes[37] or a combination of these, which are illustrated in figure 1.3.

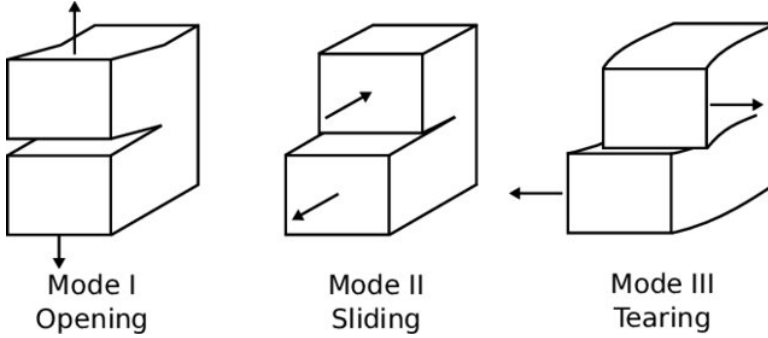


Figure 1.3: Fracture opening modes in composites [38].

The properties are obtained using simple coupon specimens such as the Double Cantilever Beam (DCB)[39] for mode I, End-Notched Flexure (ENF)[40] for mode II and the Mixed-Mode Bending (MMB)[41–43] for mode I + II. Additionally, for mode III, the Edge-Crack Torsion (ECT) test exists, but it is anno 2022 not considered a standardized coupon test. A known limitation is the dependency of the initial insert length on the measured strain energy release rate[44]. Furthermore, only near the centre energy is released under pure mode III, whereas closer to the edge spurious modes II are present. Lastly, due to non-linearity prior to the maximum load it is difficult to determine the point of initiation, resulting in a large range of fracture toughness values, for example, $850\text{--}1100\text{ J/m}^2$ in the work of Morais et al.[45].

All these properties were originally assumed to be constant for a material system; thus, the characterization tests were only performed for unidirectional coupons. However, it was found that the stacking sequence and the loading conditions influence the effective properties, and the standardized tests got adapted in recent studies[46–64]. Mainly the interface toughness increases during the propagation of the interface delamination, often referred to as the Resistance curve (R-curve) effect. For three different interfaces, this is exemplified in figure 1.4. These studies attributed these effects to fibre bridging, matrix cracking and delamination migration. An accurate and efficient way of implementing this R-curve effect in a numerical model is a popular research topic[56, 58–60, 64–67].

1.1.4 SKIN-STRINGER SEPARATION TESTING AND MODELLING

A more complex test that aims to capture the interaction of actual postbuckling-like bending conditions and skin-stringer interfaces is the Single-Stringer Compression (SSC) test[5, 21, 35, 68–78]. A specimen is loaded in compression into postbuckling such that high out-of-plane deformation occurs. The resulting different failure mechanisms in the skin and stringers due to postbuckling are shown in figure 1.5. However, the postbuckling shape depends on geometrical and loading imperfections in the SSC test. This means that

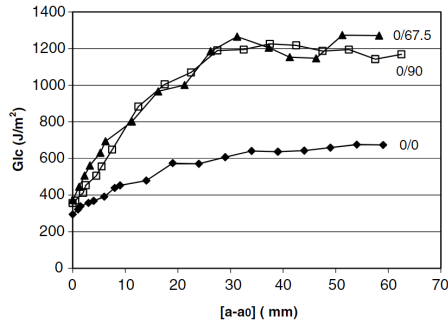


Figure 1.4: Toughening of the interface with increasing delamination lengths for different interfaces [52].

testing the same design can lead to different postbuckling shapes and, consequently, a change in the outcome of the test.

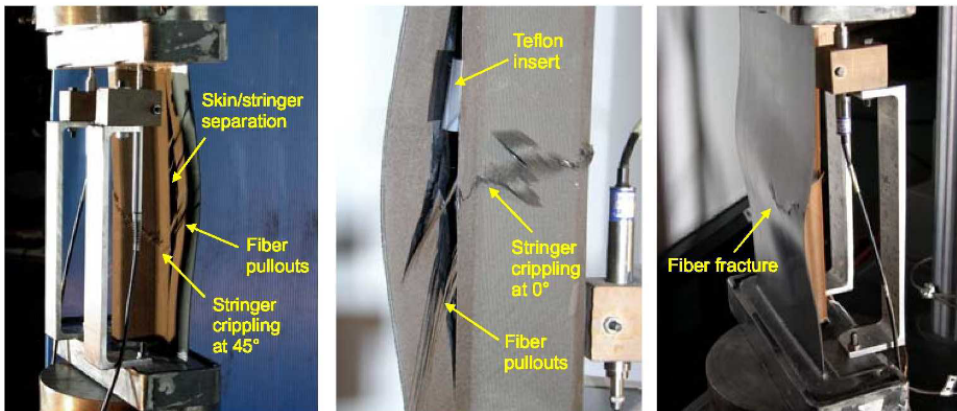


Figure 1.5: Failure modes in a postbuckled single-stringer specimen[71].

The Seven-Point Bending (7PB)[28, 79–83] test has been introduced by the NLR[28]. They noticed that the results of a Three-Point Bending (3PB) [22, 82, 84, 85]/Four-Point Bending (4PB)[86] doubler test were influenced by the presence of a free edge. The additional supports in the corner of the specimen ensure that separation initiates at the centre of the specimen and is not influenced by free edges. With five supports and two loading points, out-of-plane deformation is applied to the skin of a single-stringer specimen. This creates an approximation of the symmetric buckling shape that results from the compression of a stiffened panel or the skewed buckling shape from the shearing of a panel [79]. Recently, NASA performed seven-point bending tests as part of the Advanced Composite Project to validate a progressive damage analysis software (CompDam) and to study the sequence of events, e.g. matrix cracking, initiation, propagation and delamination migration [87]. Additionally, the test can be used to crack specimens to ensure the initial delamination size[88].

Lastly, tests can be performed on larger sub-structures, such as a skin with multiple stringers[2, 3, 7, 79, 89–91]. These tests can be costly and time-consuming. Additionally, only limited data can be obtained from the test during an unstable separation event. Although separation might occur at maximum bending or maximum twisting, most research focuses on separation driven by skin bending. However, separation may occur due to the mode III[13, 79, 92–94], when significant skin twisting is present. The availability of single-stringer tests that consider twisting separation is limited.

1.1.5 SUMMARY LIST OF TECHNOLOGICAL GAPS

1. There is a lack of standardization in the element level of the building block pyramid for skin-stringer separation.
2. There is a lack of understanding and data on the dependency of the layup on strength and stability failures.
3. There is limited knowledge on mode III delaminations at the inflection point of postbuckled panels.
4. Computational time to study postbuckling-induced skin-stringer separation is high, due to the primary use of panel-level models.
5. Criteria for delamination onset in postbuckled stiffened panels are difficult and/or time-consuming to implement.
6. Current tests considering postbuckling deformation do not guarantee the desired postbuckling shape as the shape is dependent on the geometrical/loading imperfections and (pre-)damages.

1.2 DISSERTATION OUTLINE

The main objective of this thesis is to develop a methodology for designing a loading configuration to study skin-stringer separation in a single-stringer specimen representing the postbuckling shape of composite multi-stringer panels. More details on this interaction can be obtained by studying this phenomenon in a single-stringer specimen, both numerically and experimentally. Specimens are developed that are less expensive to model, manufacture and test than the corresponding multi-stringer panel. Within these specimens, the twisting and bending failure are considered independently.

Another objective is to characterize the interface properties on the coupon level, representing the layup and thus interface of the single- and multi-stringer panel. A third objective is to have a semi-analytical framework that makes it possible to quickly identify the critical regions of a multi-stringer panel. Both these objectives are discussed first in the thesis as they lay the foundation of the main objective regarding the single-stringer specimen.

The dissertation will follow the building block approach of figure 1.2 and the outline is presented in figure 1.6. The content of each chapter are listed below.

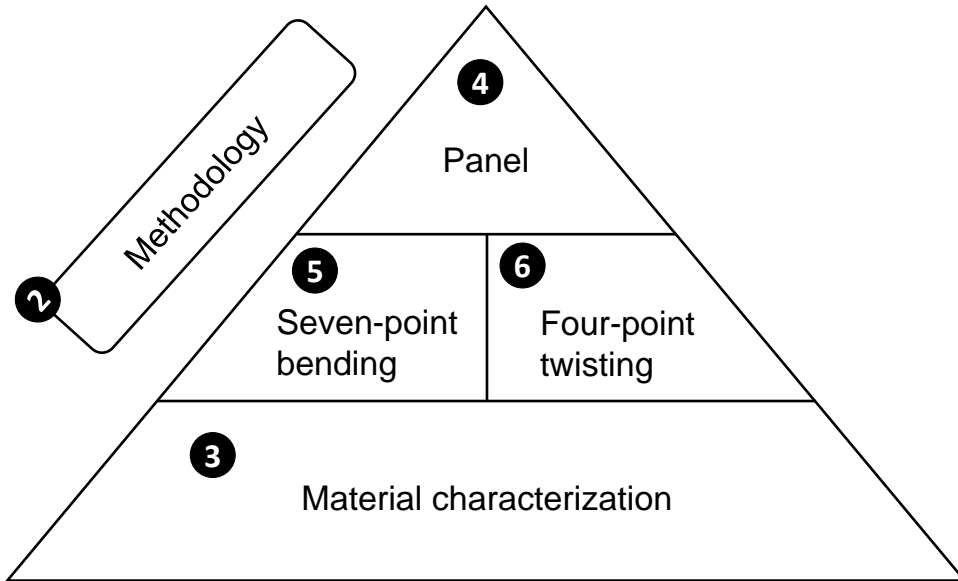


Figure 1.6: Outline of the PhD Thesis, with chapter indications.

Chapter contents

- **Chapter 2:** A methodology for the design, modelling, manufacturing, testing, and data-processing of a single-stringer specimen capable of reproducing postbuckling-like conditions for skin-stringer separation characterization is presented. The specimen and test configuration are specifically designed to reproduce the actual postbuckling conditions.
- **Chapter 3:** The material system used in this thesis is characterized and the failure modes are investigated. The actual design of the skin and flange is used for the coupon tests to consider the possible delamination migration effects that contribute to interface toughness increase. Finally, an adaptation to the state-of-the-art is proposed for implementing the R-curve properties in a finite element model.
- **Chapter 4:** A semi-analytical framework is developed that combines the postbuckling stress/strain field of finite element models with an analytical criterion based on the strain energy release rate [24, 25]. This method can be updated with the result of single-stringer tests, similar to [27], in section 5.6.1 and section 6.6.1.
- **Chapter 5:** The analyses and tests of a single-stringer specimen in a seven-point bending configuration are shown to illustrate the capabilities of reproducing/predicting the skin-stringer separation behaviour of a postbuckled panel.
- **Chapter 6:** The analyses and tests of a single-stringer specimen in a four-point twisting configuration are shown. These are among the first single-stringer tests to characterize mode III separation in postbuckling-like conditions.
- **Chapter 7:** The conclusions and recommendations of this thesis.

2

2

METHODOLOGY

The core of this thesis is the development of a methodology to numerically and experimentally study skin-stringer separation throughout the building block pyramid. A numerical framework is built to design a single-stringer specimen based on the postbuckling deformation of a multi-stringer panel. To aid in this process and improve consistency and repeatability, an in-house mesher tool is developed using Python. All configurations within the presented building-block pyramid can be made, from coupon to multi-stringer panels. The models are built using structural shell elements and interface elements if separation is to be modelled. The interface elements follow a cohesive bilinear traction-separation law. The postbuckling-induced separation shape is elliptical, which allows breaking down the complexity of separation into only two variables, length and width. These enable the testing conditions to be determined. The tests are performed at the Delft aerospace structures and materials laboratory using the in-house developed adaptive multi-point test equipment. Individual load cells at each point are used to measure the force. Specifically, the central load cell can aid in the estimation of initiation. The deformation in the panel is tracked using digital image correlation. The extent of separation is observed through c-scan methods.

2.1 INTRODUCTION OF THE OVERALL APPROACH

THE thesis can be used as a guideline for the development of composite stiffened panels, which are allowed to go into postbuckling. The basis of the methodology is a building block pyramid that is adapted to be used in the framework of designing a composite panel that is allowed to go into postbuckling without the risk of stringer separation. The main adaptation is at the specimen level, where single-stringer specimens are used to bridge the gap between coupons and panels. On all levels of the pyramid, use is made of numerical models and experimental tests.

A numerical framework has been developed with the use of Python to generate input files for all the different models used throughout the thesis and beyond. The input files are written in the Abaqus syntax, such that the Abaqus solver can be used. Separate Abaqus Python scripts are used to collect the desired output.

A guideline for the experiments is made specifically for the single-stringer tests, such that the results can be reproduced accurately. The guideline consists of the manufacturing, testing and results-processing of these specimens. The focus of the methodology is on hat-stiffened panels, but the methodology can be extended to include more stringer designs. The coupon tests are not included in this chapter, although they follow a similar manufacturing procedure, the testing is simply done according to the ASTM standards. No multi-stringer panel has been manufactured or tested.

Chapter goals

- **section 2.2:** To present the building block approach for skin-stringer separation characterization.
- **section 2.3:** To present the numerical framework for the modelling and post-processing of skin-stringer separation across all levels of the building block pyramid.
- **section 2.4:** To illustrate the approach to design a single-stringer specimen capable of reproducing postbuckling deformations of a multi-stringer panel..
- **section 2.5:** To present the experimental framework for the manufacturing and testing of single-stringer specimens in seven-point bending and four-point twisting.
- **section 2.6:** To show the two panel designs and their material properties that will be used as case studies for this thesis.

2.2 BUILDING BLOCK PYRAMID

The building block pyramid, consisting of 3 levels to study the interaction of separation and postbuckling, is shown in figure 2.1.

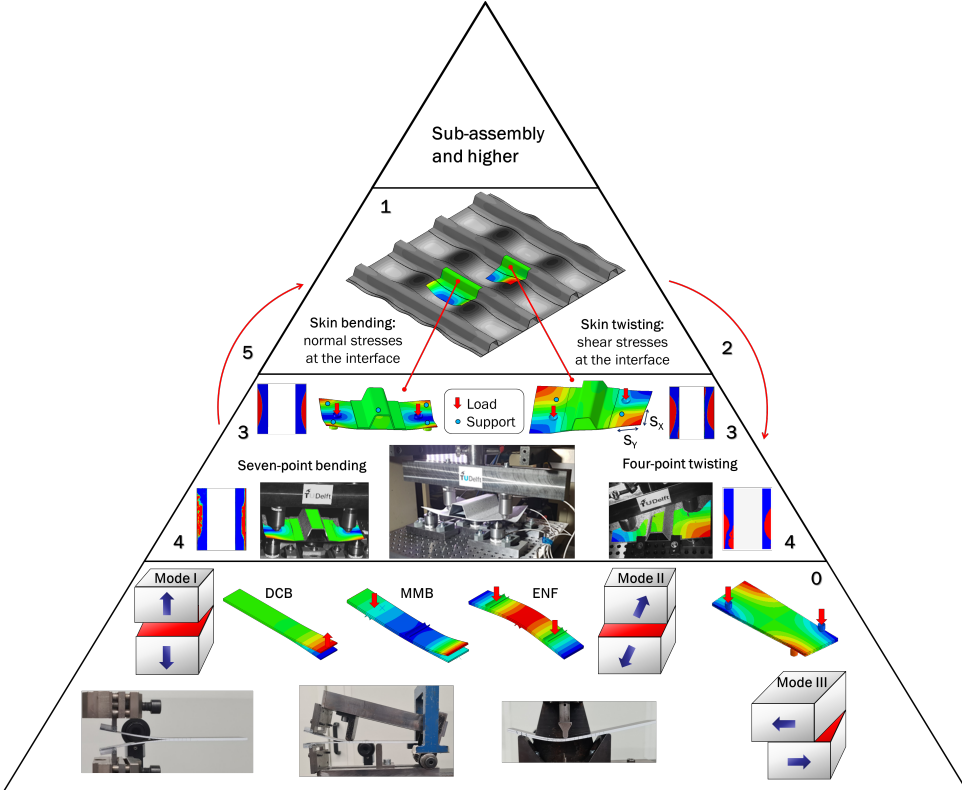


Figure 2.1: Building Block Pyramid for the characterization of (postbuckling induced) skin-stringer separation, from bottom to top: coupon, element or single-stringer, and multi-stringer panels and higher.

The current approach consists of 6 separate steps:

0. Coupon tests are performed to characterize the material properties. The building block pyramid highlights four coupon tests used to determine the interface fracture toughness. Often the unidirectional properties are already known. Hence, the focus should be on testing the properties of the actual (cross-ply) interface. At least the DCB, MMB and ENF tests should be performed in these steps. Specifically for the MMB test three mixed-mode conditions are generally used: 20%, 50% and 80%. The outcome is the critical strain energy release rate values, which can be used for the models in steps 1, 3 and 5.

1. The multi-stringer panel is analyzed and the region that will lead to the initiation of skin-stringer separation is identified. A semi-analytical moment/energy-based criterion is used to identify possible initiation, and cohesive elements are used for validation. The finite element results at the applied displacement around initiation containing the information on this critical postbuckling region is used to design a single-stringer specimen in step 2.
2. The single-stringer specimen is studied by directly loading the skin in the out-of-plane direction to impose the buckling conditions. These buckling conditions can either be bending or twisting of the skin. The former is approximated using a seven-point bending configuration and the latter using a four-point twisting configuration. In the two configurations, the locations of the support and loading points are adapted in order to best approach the postbuckling shape of the specific panel. The Residual Sum of Squares (RSS) is calculated, which is a single value representing the shape difference between the local buckling half-wave in the multi-stringer panel and the deformation of the single-stringer specimen. This value is qualitative in the sense that it needs to be minimized but does not give a physical representation of the actual difference in shape. The calculation of the RSS is repeated for a given set of support and loading point locations. The configuration with the smallest difference is deemed most suited to study the postbuckling conditions on the single-stringer specimen. The final configuration is used as the input for steps 3 and 4.
3. A more detailed numerical model of this single-stringer specimen is developed using cohesive elements. The purpose is twofold: to study initiation and propagation of skin-stringer separation due to an out-of-plane deformation representative of the postbuckling shape observed in a stiffened panel, and to predict the response of the experimental test, step 4, in order to design the testing procedure and to choose the data acquisition accordingly.
4. Experimental tests are used to further investigate the actual physics that affects the skin-stringer separation response. It allows the validation of the numerical model from step 3, which can be updated accordingly. The combined information from steps 3 and 4 can be used for step 5.
5. The information that is obtained from the single-stringer specimen can be used in the multi-stringer panel model in order to make a final prediction of the failure response of the panel. Experimental tests of these large panels are also necessary but should be limited in order to be cost- and time-effective.

Step 0 is presented in chapter 3. Step 1 is presented in chapter 4. Steps 2-5 are presented in chapter 5 for the seven-point bending test and in chapter 6 for the four-point twisting test.

2.3 NUMERICAL FRAMEWORK

A numerical framework has been created for the generation of all the models used in this thesis¹. Python is used as the coding language as it is open-source and therefore the mesher is independent of the Abaqus GUI/CAE. It makes it possible to quickly generate models for a parametric or sensitivity study. It also makes sure there is consistency in the models, between the different levels of the building block pyramid. Lastly, the order and naming of the parts need to be consistent for output processing such that it can be compared to experimental output.

2.3.1 MESHING STRUCTURAL AND INTERFACE ELEMENTS

Even though the numerical models look different from a design point of view, there are a lot of similarities. Hence, the mesher is written based on these similarities to create consistency. For example, the coupon, doubler and single-stringer all have a bottom laminate, referred to as the skin, and a top laminate referred to as the stringer. In the case of the coupon, this is actually another sublaminates, and for the doubler, it is simply a flange-like design. The skin and stringer can be connected in four different ways: a contact definition, cohesive interface elements, a tie-constraint or shared-nodes for continuity. A contact definition is used for the representation of inserts in coupon specimens, cohesive for the modelling of skin-stringer separation, and tie-constraints are used to model the skin and stringer separately, but not allowing any separation between them.

STRUCTURAL ELEMENTS

The skin and stringers are thinner compared to the in-plane dimensions, hence the structures can be approximated as a shell. Although a Continuum Element such as C3D8(R/I) could be used for these models, a more appropriate choice is a shell element. The three options that can be used within Abaqus are briefly discussed:

- **Conventional Shell element (S4R)** is a shell element in its most pure form. The element has no physical thickness but is a simple quadrilateral plate element with a node in each corner with 6 degrees of freedom, which correspond to translation and rotation. Commonly S4R represents the mid-plane of a plate, where the user defines the thickness used for the calculations. In the case of modelling composites, the thickness of each individual ply is given as an input. This element is computationally very efficient, especially for use in buckling problems. However, these elements are not straightforward to use in combination with contact load or with interface elements.
- **Continuum Shell element (SC8R)** is a continuum element. The hexahedron element has a finite thickness with a node in all corners with only the three translational degrees of freedom. The thickness of the element is the local thickness of the plate, whereas in a composite layout, the relative thickness of each of its plies is given as an input for the total thickness. Multiple elements can be stacked, where a continuous stack is able to allow continuous through-the-thickness shearing behaviour. This can be beneficial in some cases, but a user needs to be weary as the size of the

¹<https://github.com/ljkootte>

model increases rapidly. The finite thickness of the elements makes them ideal when modelling the actual contact with a (static) indenter. Furthermore, interfaces are easier to consider as the top surfaces of the skin elements and bottom surfaces of the stringer flange elements can be coincident. When using matching meshes, which is preferred, the nodes of the skin and bottom nodes of the stringer are coincident. This allows for sharing nodes, efficient tie constraints or interface elements to be generated.

- **Continuum Solid Shell element (CSS8)** is relatively new and thus not yet common or widely investigated. Hence, for the purpose of this thesis, this is omitted. It is very suitable for through-the-thickness behaviour but less efficient than the SC8R. Another downside when using the elements to model composite laminates is the fact that they require 3D material properties as opposed to simple planar ply properties.

The SC8R elements are primarily used within this methodology unless mentioned otherwise. The main two reasons are the ability to create the actual zero-thickness interface elements and the ability to accurately model the contact with the indenters.

The numerical tool creates perfect cuboid elements for the skin. In the case of a stringer design with a radius in the transverse direction, the bottom and top surfaces are always parallel to each other. The location of the top nodes of the skin and bottom nodes of the stringer are coincident, where the skin and stringer surfaces meet. Because of the perfectly square meshes, during the post-processing step results along lines of exact locations can easily be extracted.

A mesh sensitivity study is strongly recommended at the start of the methodology. An appropriate size balances the computational efficiency of a model with the accuracy of the results. The numerical framework allows for defining a global mesh size for the structural elements; by changing this value multiple models can be quickly generated for the sensitivity study. The mesh size of these structural elements differs between the configurations. For a coupon about 1 mm is used, 2 mm for the single-stringer and up to 5 mm for the multi-stringer models. The latter is chosen to limit the size of the model as the physical dimensions are larger, whilst still being able to capture the buckling deformation correctly. The slightly smaller element size for the other designs is mainly to cope with the more complex local deformation near the load introduction points.

A bias in the mesh allows keeping the global mesh size along the border of the models. An increase of the mesh density is applied near the location where complex damage mechanisms are expected, modelled by interface elements, to be discussed in section 2.3.1.

The nodes and elements are defined as follows:

*Node

```
<Node ID>, <X>, <Y>, <Z>
2, 0.625, 0.000, 0.000
32144, 25.000, 125.000, 3.072
```

*Element, type=SC8R

```
<Element ID>, <N1>, <N2>, <N3>, <N4>, <N5>, <N6>, <N7>, <N8>
1, 1, 2, 43, 42, 8037, 8038, 8079, 8078
```

A typical mesh of a single-stringer model can be seen in figure 2.2

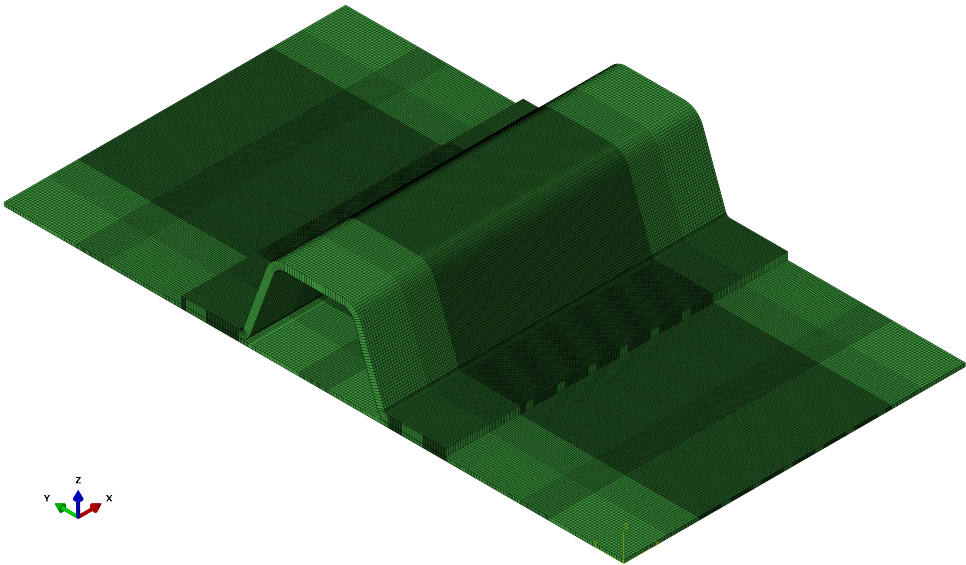


Figure 2.2: A typical mesh for a single-stringer model; The element size is 2 mm along the edges and 0.3 at the longitudinal centre and the skin-stringer overlap, where cohesive elements are placed at the interface.

The cross-sectional mesh of the stringer itself plus the possible variables can be seen in figure 2.3.

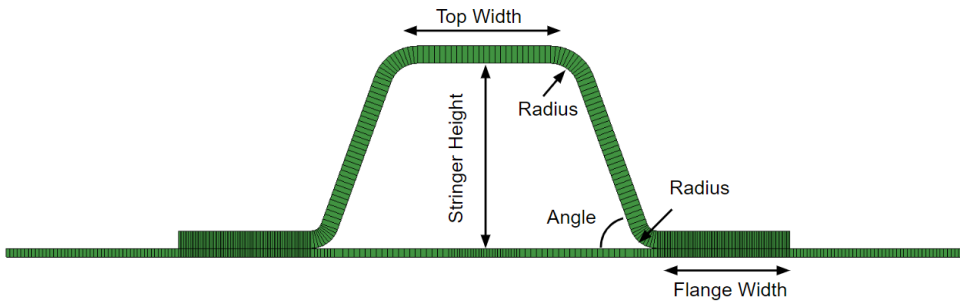


Figure 2.3: The variables in the hat-stringer cross-section.

The order in which the element nodes are defined is important for the behaviour of the element and the assigned section. The primary direction of the element is the vector from N1->N2. The secondary direction is from N1->N4. Lastly, the stacking direction is from N1-N5. An incorrect definition of the primary and secondary direction can be fixed by assigning a coordinate system when assigning a section. The stacking direction requires more care. First of all, when defining the geometry within the Abaqus GUI, the engineer would start with the drawing of a cross-section and then extrude it over the length. The

standard is that the stacking direction will be the same as the extrusion direction, which needs to be manually changed to the top and bottom of the cross-section. Otherwise, the stacking of the composite plies in the section definition will also be in the lengthwise direction. When visualising the stress/strain results, the bottom section output is also shown in the N1-N4-N5-N8 plane, instead of the N1-N2-N3-N4 plane.

The elements section that is used is the composite shell section. If one element through-the-thickness is used, which is the case unless mentioned otherwise, the entire layup is defined in that section. If for example, the skin is divided into layers of elements of equal thickness, the first row of elements is assigned the first half of the laminate, and the second row is assigned the second row of elements. As opposed to S4R, the thickness of the plies has no physical meaning as they are relative to the actual thickness of the elements. For example, if an element of 1 mm has only two plies with $t_{ply} = 0.1$ for P1 and $t_{ply} = 0.3$ for P2, the thickness of P1 is $0.1/(0.1 + 0.3) \times 1.0 = 0.25\text{mm}$ and 0.75mm for P2.

```
*Shell Section, elset=<SectionName>, composite, layup=
<LayupName>, orientation=<CSYS>, stack direction=3
<tply>, <MatName>, <Ori>, <PlyName>
0.128, 3, IM7/977-3, -45, P1
```

The material properties are defined as follows, where for the SI units the density is given in tonnes/mm³ and the stiffness in MPa.

```
*Material, name=<MatName>
*Density
<density>
*Elastic, type=LAMINA
<E1>, <E2>, <v12>, <G12>, <G13>, <G23>
```

SKIN-STRINGER INTERFACE MODELLING

The interface between skin and stringer can be modelled in different ways. The most important for the purpose of this thesis is through cohesive elements. An extensive part of this section will look into how the cohesive elements are connected, which properties are used and the initiation and propagation law they adhere to. Other aspects that are discussed are the interface connections by sharing nodes, surface-to-surface tie and contact.

If there is no separation allowed, the skin is tied to the stringer using a surface-to-surface tie constraint. All the skin elements are grouped in an element set named Skin, and similarly for the stringer elements. A surface with the same name is created, where S2 refers to the top surface of the element set for the skin and S1 to the bottom surface of the stringer element set. In the tie constraint the first input, the stringer, is the slave surface and the skin is the master surface. The logic behind it is that the skin is the surface undergoing the most deformation, either due to skin buckling or applied out-of-plane deformation. The stringer simply deforms as a result of the skin deforming, thus the slave follows the master surface.

```
*Surface, type=Element, name=Skin
Skin, S2
*Surface, type=Element, name=Stringer
```

Stringer, S1

*Tie, name=Skin_Stringer, adjust=yes

Stringer, Skin

Cohesive elements are added to the models in which skin-stringer separation is investigated [95]. Other options that can be considered for this purpose, but are omitted in this thesis, are the Virtual Crack Closure Technique (VCCT)[96, 97] and cohesive contact[98]. Cohesive zone modelling is preferred over VCCT within this work as it allows to model both the initiation as well as the propagation of delamination. Cohesive elements are created by simply using the top nodes of the skin and the bottom nodes of the stringer to create an eight-noded element: COH3D8. Because the mesher is able to create a mesh where the nodes of the stringer and the skin are perfectly coincident, the resulting cohesive elements are actually zero-thickness. This is opposed to creating cohesive elements through Abaqus CAE, where a finite but small thickness needs to be given such that due to rounding errors no negative volume elements can be created. In this case, the skin, interface and stringer elements all share the same planar mesh, making the model as efficient as possible. If the mesh of the skin does not match with the stringer mesh, the user could opt for either tying the cohesive elements to the adjacent skin or stringer or using cohesive contact.

The cohesive elements follow a bilinear traction-separation law, which is shown in figure 2.4. K_0 and K_i are the interface stiffness for pristine and during damage evolution respectively. Initiation is defined by the critical strength τ_c and the opening d_0 . The final opening is d_{end} when the critical strain energy release rate (G_c) is reached. The behaviour of cohesive elements can be broken down into three stages.

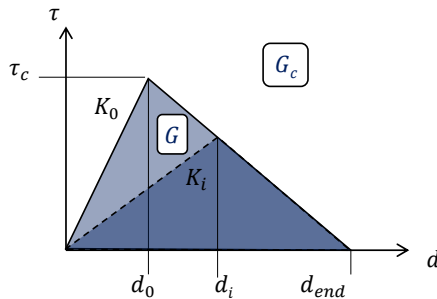


Figure 2.4: Bilinear traction-separation law.

In the first stage, the elements behave as linear-elastic up to initiation. The quadratic stress criterion, presented in equation (2.1), is used to define the initiation of damage in a cohesive element[99]:

$$\left(\frac{\tau_I + |\tau_I|}{2\sigma_c} \right)^2 + \left(\frac{\tau_{II}}{\tau_c} \right)^2 + \left(\frac{\tau_{III}}{\tau_c} \right)^2 = 1 \quad (2.1)$$

where τ_I , τ_{II} , and τ_{III} are the traction at the interface, where τ_I is only considered when positive. σ_c and τ_c indicate the interface strength for the specific normal and shearing modes, respectively.

During the second stage, the mixed-mode propagation of the damage is captured according to the Benzeggagh-Kenane law from equation (2.2). The damage variable (D), normally requested within Abaqus as SDEG, decreases the stiffness of the interface by $K = K_0(1 - D)$.

2

$$G_C = G_{IC} + (G_{IIC} - G_{IC}) \left(\frac{G_{II} + G_{III}}{G_I + G_{II} + G_{III}} \right)^{\eta_{BK}} \quad (2.2)$$

The variables G_I , G_{II} , and G_{III} are the strain energy release rates for the three primary modes. The subscript C indicates the critical strain energy release rate, where $G_{IIC} = G_{IIC}$. The exponential η_{BK} is a material property that defines the interaction between mode I and mode II. This value is obtained from fitting equation (2.2) to the critical strain energy release rate versus mode-mixity, obtained from the coupon tests.

The mode-mixity is defined by the ratio of the shearing modes to the total strain energy release rate as shown in equation (2.3). This output can be requested for the cohesive elements as MMIXDME, for the Abaqus version up to 2019 this is only through the input file.

$$M = \frac{G_{II} + G_{III}}{G_I + G_{II} + G_{III}} \quad (2.3)$$

In the last stage, there is no remaining stiffness. In some cases, the user can opt for element deletion, but in this case, the elements are kept. The remaining purpose of the elements is to not allow interpenetration of the skin and the stringer.

The in-plane mesh size of the cohesive elements is determined by the properties of the adherents, the interface properties and the expected loading conditions. Generally, an interface that is predominantly loaded in mode I require a denser mesh compared to mode II. The dense mesh is required to cope with the nonlinear stress peak behind the crack tip. As a rule of thumb, three to five elements are required in the active cohesive processing zone[100]. The cohesive processing zone length can be approximated using equation (2.4)[101].

$$l_{cz} = \frac{9\pi}{32} E \frac{G_c}{(\sigma_c)^2} \quad (2.4)$$

For actual pure mode I load cases, such as in the analysis of a Double Cantilever Beam with a high interface strength a mesh size as small as 0.1 mm is required. A mesh size of 0.1 mm is used for all coupon models. For the other models, a mesh sensitivity study was performed in order to obtain five active cohesive elements in the cohesive processing zone. This led to a mesh size of 0.3 mm, which is used for all models throughout this thesis. In most models, a mixed-mode condition above 0.3 is observed, hence allowing the coarser mesh.

The cohesive processing zone length can be visualized by opening the output database of the model in the Abaqus viewer. The limits of the plotted damage variable, normally SDEG, should be set to 0.00001 (lower) and 0.99999 (upper). -The Abaqus viewer does not allow values smaller than 10^{-6} .- The elements that are in the second stage, past initiation and before final failure, are highlighted. The elements that are either completely intact or completely failed are outside of these limits and are generally shown in greyscale. Counting the active elements in the direction of crack propagation should result in no less than three

elements. Preferably no more than seven elements are present, otherwise, the model size is inefficiently large.

The material properties for a cohesive interface are given in the input file as follows:

```
*Material, name=<CohName>
*Density
<density>
*Elastic, type=traction
<KI>, <Ksh>, <Ksh>
*DAMAGE INITIATION, CRITERION=QUADS
<sigc>, <tauc>, <tauc>
*damage evolution, type=energy, softening=linear,
mixed mode behavior=BK, POWER=2.07
<GIc>, <GIc>, <GIc>
*COHESIVE SECTION, elset=<CohElsetName>, material=
<CohName>, THICKNESS=specified, response=traction
separation, controls=<ControlsName>
1.0,
*section control, name=<ControlsName>, viscosity=3.e-05
```

2.3.2 LOAD CASES AND TEST CONFIGURATIONS

The load cases are modelled through contact with loading points or support points, which can be spherical or cylindrical, or by applying direct boundary conditions to a set of nodes.

PANEL MODELS

The design of a multi-stringer panel can be seen in figure 2.5. The length and width, plus the position and number of stringers and their position can be changed as required. In this thesis, only a panel with four stringers is used.

The two edges of the panel that are parallel to the stringers are kept unconstrained. The other two edges have clamped boundary conditions. The panel is loaded in end-shortening by applying a displacement boundary condition at the end of the panel along the stringer's axis. The same principle would apply to a potential single-stringer compression specimen model.

SEVEN-POINT BENDING

The 7PB configuration consists of five supports and two loading points. A specimen is placed on top of the supports; in figure 2.6 a single-stringer specimen is illustrated. The main variables that are used in this setup are the length and width of the skin and the position of the supports and loading points. The four corner supports are placed at a distance S_X and S_Y from each of the skin corners. The fifth support is placed at the centre of the skin ($x = L/2$, $y = W/2$). The two loading points are placed at a distance L_X ($x=L/2$) and L_Y from the skin corner. By removing the central loading point a six-point bending (6PB) setup can be created.

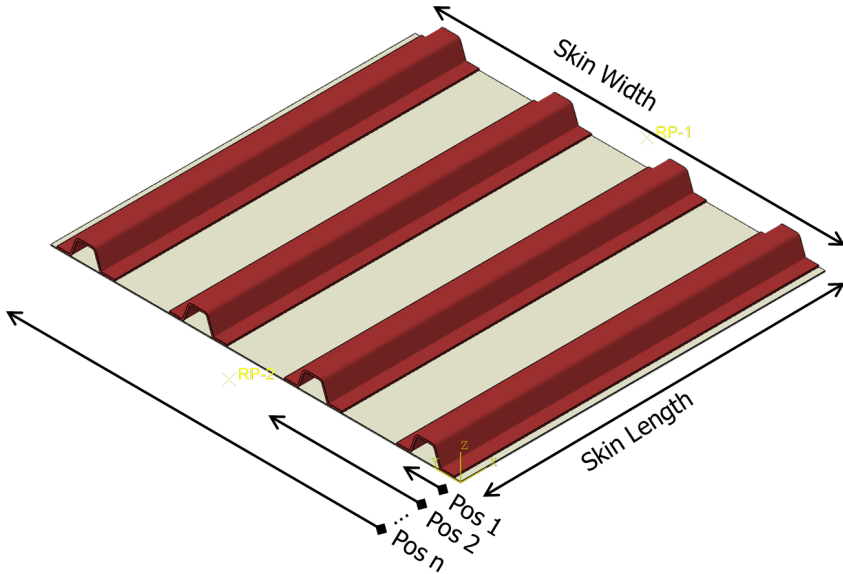


Figure 2.5: Multi-stringer panel design

The configurability of the model allows different combinations of support and loading point positions to be studied. This property is later used in section 2.4, where a configuration is determined that allows the recreation of the deformation observed in a larger multi-stringer panel.

The specimen is loaded through a contact constraint between the skin and hemispherical analytical rigid surfaces (ARSR) representing the loading points of the actual experimental set-up. A finite sliding contact constraint is used to capture the change in contact state during large skin deformation as opposed to a small sliding condition[23]. A transverse friction coefficient of 0.2 between the indenters and the skin makes sure the panel does not fly away during the analysis. The contact areas on the skin are square-shaped and the size is equal to the radius of the indenters.

The contact between a flat surface and a hemispherical and rigid indenter can cause issues for the solver. This is because only an infinitesimal area is making contact at a low deformation. Therefore a smaller mesh size of 0.3 up to 0.5 mm is also present at the contact areas. The loading points move orthogonally to the skin surface, imposing the buckling-like deformation.

Each support and loading point is defined in the same way as can be found below. For supports $\langle ori \rangle$ is 1.0, which translates to upward facing in the positive z-direction. For the loading points $\langle ori \rangle$ is -1 or facing downwards. The ID of the nodes starts at 9900000 and increases by 1 for each additional support/load point.

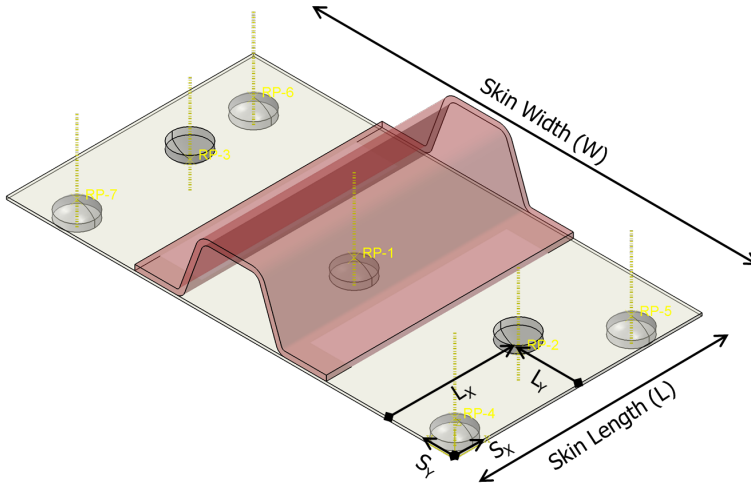


Figure 2.6: Seven-point bending design.

```

*Node
  990000<ID>, <X>, <Y>, <Z>
*Surface, type = REVOLUTION, name = Indenter<ID>
  <X>, <Y>, 0.000, <X>, <Y>, <ori>
START, 0., 0.
CIRCL, 10.0, -5.0, 0., -12.5
LINE, 10.0, -9.0
*Nset, nset=R<ID>
990000<ID>
*Rigid Body, ref node=R<ID>, analytical
surface=Indenter<ID>

```

Each support and loading point is paired with a set of elements of the skin. These skin elements are individually collected first in an elset, which is named $IND<ID>_S<x>$ to refer to the indenter number and the Side which will be under contact. After this set of elements is translated to a surface named $Ind<ID>$. A support contacts the bottom surface of the skin elements, corresponding to surface 1 or S1. Oppositely, the loading points contact the top surface or S2 of the skin elements. The contact pair is identified for each set, whereas the surface interaction property that includes the frictional coefficient only needs to be identified once.

```

*ELSET, ELSET = IND<ID>_S1
%A set of all the elements that will be in contact
*Surface, type=ELEMENT, name=Ind<ID>
IND<ID>_S1,S1
*Contact Pair, interaction=SURFS, type=SURFACE TO

```

SURFACE, no thickness, TRACKING=STATE
 IND<ID>, Indenter<ID>
 *Surface Interaction, name=SURFS
 *Friction
 0.2

2

FOUR-POINT TWISTING

A 4PT configuration has two supports and two loading points in opposite corners of the skin, as illustrated in figure 2.7. The two supports as well as the loading points are positioned S_X and S_Y from the corners. The remainder of the modelling approach is the same as discussed in the previous section regarding the 7PB configuration.

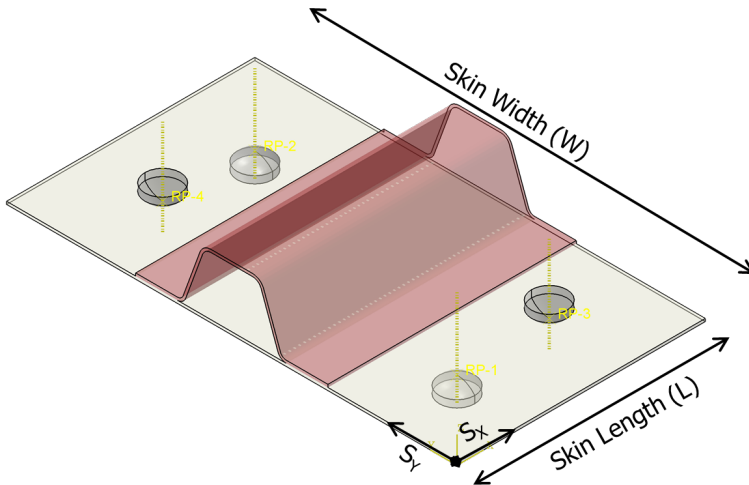


Figure 2.7: Four-point twisting design.

COUPONS

The three standardized coupon tests to characterize interface fracture toughness are highlighted here. The basis of the coupon design is the same and is shown in figure 2.8. An initial insert with a certain length a_0 acts as a precrack.

The double cantilever beam[39], shown in figure 2.9, is the most basic coupon specimen. Upon loading the edge through a hinge constraint, the crack propagates. When looking at crack propagation in a skin-stringer interface, the crack front moves in the direction of the skin width. Therefore within this framework, the width direction in the coupon specimen is equal to the main direction of crack propagation. The length of the coupons can be changed, but the standards prescribe 25 mm, which is also used in this work. With a laboratory that uses imperial units, 1 inch (25.4 mm) could be used.

The end-notched flexure[40] coupon test has the same design parameters as the DCB coupon. The difference is in the loading configuration, where the hinge supports

are replaced by three roller supports, as seen in figure 2.10. The delamination propagates between the rightmost and the central roller upon moving the central roller downwards. The contact definition between the coupon and the roller supports has been described in the seven-point bending configuration section.

The mixed-mode bending[41] test combines the double cantilever beam and the end-notch flexure test. The configuration is illustrated in figure 2.11. The edges with the inserts are hinged, and two roller supports impose a bending deformation. The top roller and top hinge are connected to a reference point at distance c from the top roller. By changing this distance, the mixed-mode conditions can be altered.

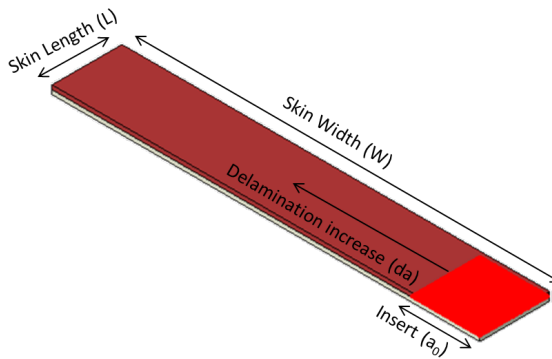


Figure 2.8: General coupon design

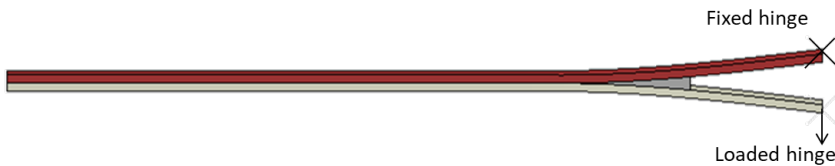


Figure 2.9: Double cantilever beam design

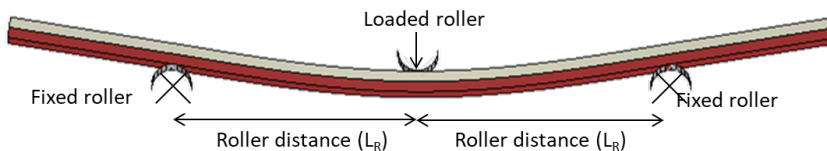


Figure 2.10: End-notched flexure design

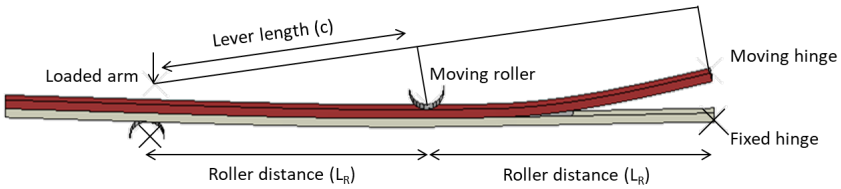


Figure 2.11: Mixed-mode bending design

2.3.3 ANALYSES AND POST-PROCESSING

ANALYSIS

Dynamic implicit analysis with quasi-static properties is used for all models. With a deformation rate of 4 mm/s, both for the in-plane and out-of-plane loaded models, the kinetic energy is kept to a minimum.

The requested history outputs are the displacement (U) and reaction forces (RF) at the supports and loading points as well as all the energies in the system. The history output has a low number of variables but these are output frequently. Within the input file, it looks like:

```
*OUTPUT, HISTORY, FREQ=1
*NODE OUTPUT, NSET=Supports
RF,U
*NODE OUTPUT, NSET=Loads
RF,U
*OUTPUT, HISTORY,variable = PRESELECT
```

The requested field outputs are the displacement (U) of all the nodes in the body. In addition, the stresses (S) and strains (EE) as well as the section curvatures (Sk), moments (Sm) and forces (Sf) are output for all elements. When cohesive elements are used, the damage variables DMICRT and SDEG are requested, which correspond to the initiation and propagation status. MMIXDMI and MMIXDME are the mixed-mode condition for initiation and propagation, respectively. The field output has a high number of variables and is often requested for large models only every 5 or 10 increments. The data is requested in the input as follows:

```
*Output, field, FREQ=10
*Node Output
U
*Element Output, directions=YES
EE, S, Sk, Sm, Sf
*ELEMENT OUTPUT, ELSET=Coh
DMICRT, SDEG, MMIXDMI, MMIXDME
```

The out-of-plane deformation (U3) is the main variable that shows the postbuckling behaviour. Hence, in the specimen design in the next section, this variable is used in comparing the deformation between the panel and the single-stringer specimen.

POST-PROCESSING

Three types of post-processing are done on the models. These are mainly Abaqus Python scripts, advanced Python scripts with data handling tools, and manually through the Abaqus viewer.

First of all, Abaqus scripts, automatically called by Abaqus CAE noGUI=script.py, are used to get the history output for the force-displacement response and write it to a generic txt file. The script can use the force-displacement response to check for an increase in compliance, such that at critical points the data regarding that output frame can be written and/or an image in the correct formatting can be saved.

Global response The global response of the specimen and panels is often shown as a plot of the out-of-plane displacement (U3) and the damage variable (SDEG) of the cohesive elements. This is either in isoview or in top plane view. For the cohesive elements in isoview the skin and stringer are shown as grey and transparent, and for the top plane view the skin and stringer are removed. An example of the out-of-plane and interface damage plots is shown in figure 2.12.

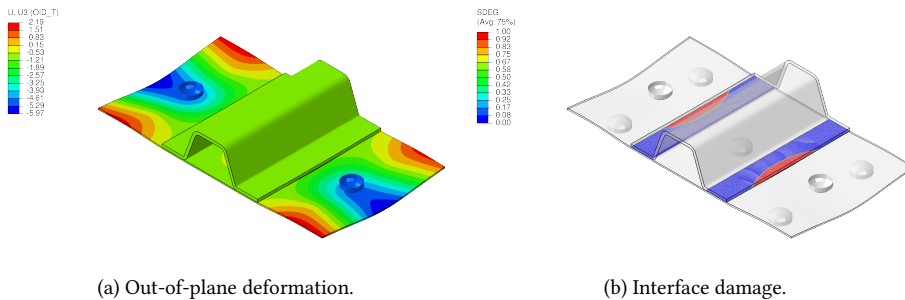


Figure 2.12: Examples of numerical results.

For the out-of-plane deformation plots, red generally indicates a positive out-of-plane displacement, blue negative and light green as low/zero displacements. However, the scale can change if the negative displacement is much larger than the positive. For the interface damage in figure 2.12b, blue means that damage in the cohesive elements has not been initiated. Red indicates that the cohesive element has failed or is very close to failure. The rainbow colour pattern in between depicts the processing zone, where the damage variable is between 0 and 1, but this is often a small region.

Force-displacement response The force-displacement response of a finite element model with cohesive elements is shown in figure 2.13, where the seven-point bending configuration is used as the example. The total curve represents the total applied force. The other LC-curves correspond to the reference points of each of the indenters, where the numbering corresponds to the layout presented in figure 2.14. Due to the perfectly symmetric loading conditions, the curves of LC1 and LC2 overlap, as well as the curves of LC3+LC7 and LC4+LC6.

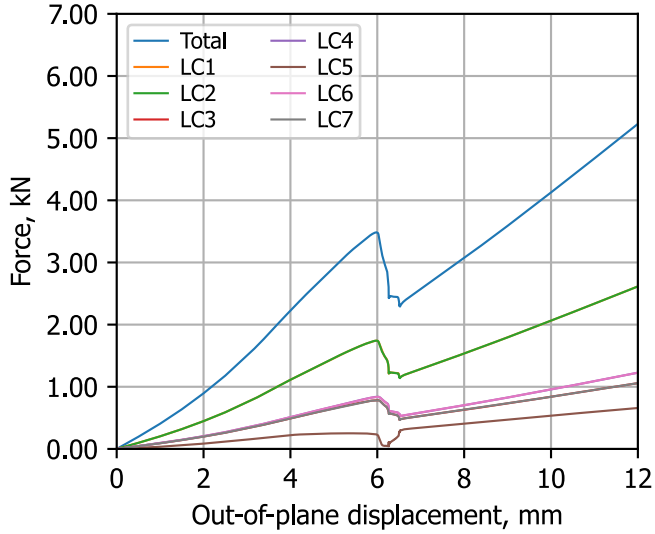


Figure 2.13: Loadpoint distribution and total force.

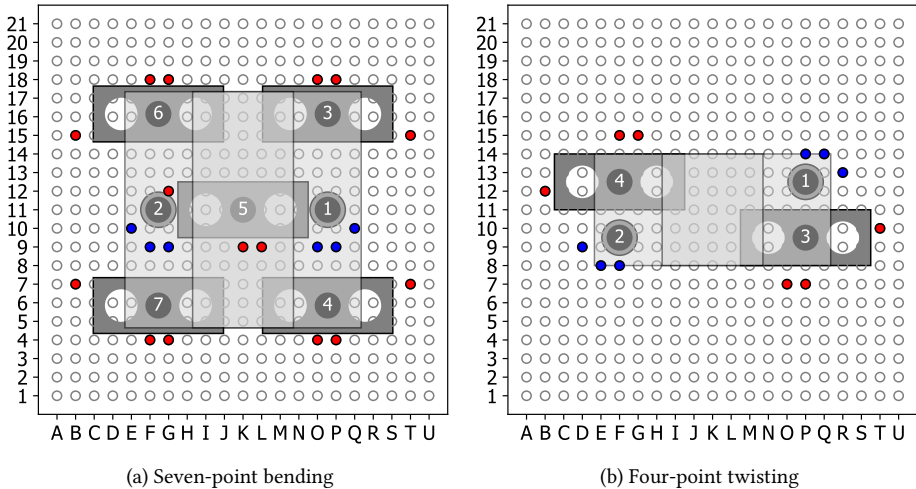


Figure 2.14: Loadcell naming of supports and loading points in the adaptive multi-point test equipment. The schematics depict how to place the dowel pins for aligning the supports (red pins) and loading points (blue pins) in the test equipment.

The models, both 7PB and 4PT, exhibit a geometrical stiffening leading to a decrease in compliance. The stiffening occurs because the loading conditions result in an anticlastic surface deformation, like a saddle shape, where the bending over one axis inhibits bending over the other. On the other hand, skin-stringer separation causes an increase in compliance due to the smaller connecting area. At some point, the increase and decrease compensate each other such that the load seems to be almost linearly increasing. The maximum load can often be identified by a steep drop in load. The remaining stiffness after the drop in load corresponds to the bending of the skin only, as the stringer has been fully separated.

The initiation of skin-stringer separation is more difficult to identify from the force-displacement curve due to the combined nonlinearity of the deformation and the skin-stringer separation. With cohesive elements, initiation can be identified within a model by pinpointing the displacement at which the first cohesive element reaches a damage variable of 1. More specifically, all the integration points of that element should reach 1, meaning that the entire element has degraded.

Another option to identify initiation has been developed for the 7PB configuration. First of all, going through all the output frames to find the first failing element can be time-consuming. Secondly, for the tests, it is impossible to investigate the interface locally and continuously. In the alternative method, the central support (LC5) plays a crucial role. By normalizing the load in the central support by the total applied load, the load distribution can be tracked. The result is shown in figure 2.15. A clear sudden change can be spotted around 3.8 mm, which corresponds to the initiation. When the stringer is partially separated, the corner supports start taking up relatively more load compared to both the non-separated and fully separated conditions. This method can also be applied to the force-displacement results of the experimental investigation.

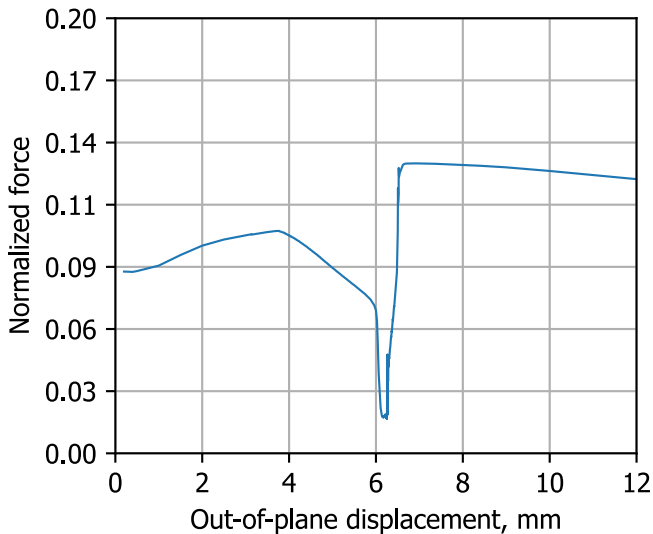


Figure 2.15: Normalized central force.

Separation response The complexity of the growth of a delamination created during skin-stringer separation can be reduced to two variables, by assuming the shape follows a perfect elliptical response. The elliptical approximation is shown in figure 2.16. This makes it possible to quantify the damaged area's size, the propagation speed by comparing it to the applied force/displacement, and the direction of growth by the change in the elliptical shape. Furthermore, it can be used to compare the separation response between different models. Lastly, trends can be observed based on these variables.

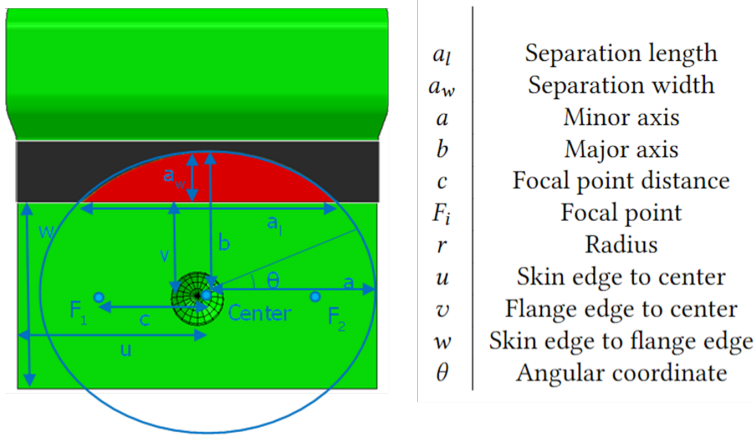


Figure 2.16: Elliptical definition in relation to the single-stringer specimen.

The list of variables used in the ellipse can be found in figure 2.16. The two variables that define the ellipse are the separation length (a_l) and separation width (a_w). Separation width is the most important, as the maximum value that can be obtained is limited by the flange width itself. This is opposed to the separation length which is dependent on the length of the specimen or panel. For example, when comparing the results of the specimen and the panel at a later stage, the design of the stringer is fixed/constant, whereas the length of the panel is 5 times the length of the single-stringer specimen. Furthermore, reaching a critical value of a_w can already lead to final failure in a quasi-static load case; too much of the stringer has been released from the skin and consequently, the load-carrying capabilities are reduced.

In a single-stringer specimen loaded in a 7PB configuration, the separation front seems to be elliptical. An ellipse is defined by location of the origin/center and the minor and major axes or focal point distance. The first assumption is that the center of the ellipse is the same distance from the stringer flange edge as the loading point $v = w - L_Y$. The longitudinal position (u) of the center is close to the position of the loading point, but can shift slightly due to the skew deformation introduced by the layup. The minor axis is defined by the center distance to the edge plus the separation width ($b = v + a_w$). The major axis is determined as a function of the minor axis and the separation length, which is shown in equation (2.5).

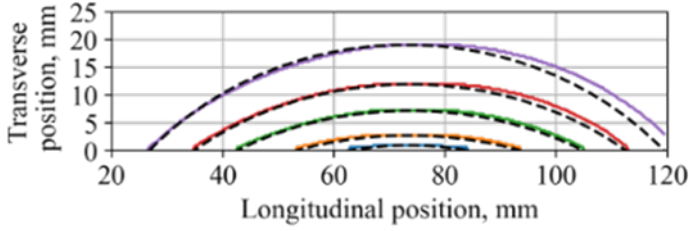


Figure 2.17: Elliptical approximation of actual separation fronts.

$$b = v + a_w \quad a = \frac{0.5a_l}{\cos\left(\sin^{-1}\left(\frac{v}{b}\right)\right)} \quad (2.5)$$

From the elliptical equations, the radius of the ellipse can be determined using the major and minor axes and the elliptical angle (θ), illustrated in equation (2.6). This can be expressed in an x-y framework using equation (2.7). The actual cohesive separation front and the elliptical approximation (dashed lines) at multiple stages throughout its propagation are plotted in figure 2.17. The overlap shows an almost perfect match, which shows that reducing the problem to only the variables a_w and a_l is suitable.

$$r(\theta) = \frac{ab}{\sqrt{(b\cos(\theta))^2 + (a\sin(\theta))^2}} \quad (2.6)$$

$$x = u + r(\theta)\cos(\theta) \quad y = (w - v) + r(\theta)\sin(\theta) \quad (2.7)$$

The force and displacement response can be coupled with the separation response to further investigate the behaviour. The change of the separation width and length for the applied out-of-plane displacement (speed of propagation) is shown in figure 2.18.

The true power of this method is in combining the separation width and length together in figure 2.19. The speed of propagation can change due to different loading cases (in-plane vs out-of-plane) and different material properties. This method makes it possible to identify if the propagation behaviour is consistent regardless of the propagation speed. It is assumed that if the shape is similar, the macromechanical damage models are also similar.

2

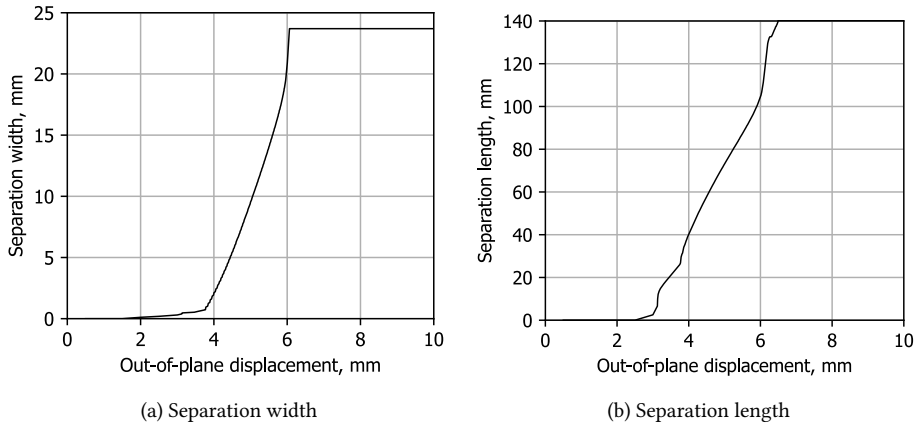


Figure 2.18: Out-of-plane displacement plotted against separation sizes to illustrate speed of propagation.

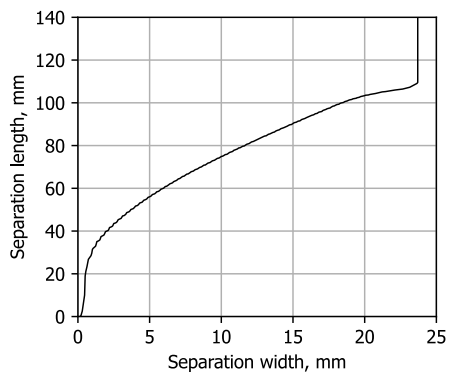


Figure 2.19: Separation width plotted versus separation length.

2.4 A CONFIGURATION TO APPROXIMATE THE POSTBUCKLING SHAPE

The core of the methodology is to design a single-stringer specimen to mimic the postbuckling deformation of a multi-stringer panel. Two types of locations can be approximated, these can be seen in the building block pyramid in figure 2.1. The location of the highest out-of-plane deformation can be matched with a 7PB configuration, and the location of the highest twisting by a 4PT configuration.

For the panel, a field output report that contains the postbuckling shape around the expected point of initiation of skin-stringer separation is created. The field output report contains the node labels and the out-of-plane displacement. The report can be combined with the input file that contains the mesh description. Pandas in Python is used to create a DataFrame containing the node label, coordinates and displacement. This DataFrame is initially used to design the single-stringer specimen. For each single-stringer specimen model, a similar output DataFrame is created, which will be compared to the DataFrame of the panel.

The buckling half-wavelength of the panel drives the length of the single-stringer specimen. The half-wavelength can be easily obtained by dividing the length of the panel by the number of half-waves. Otherwise, the minima and maxima of the displacement are obtained as the locations where the first derivative of the out-of-plane displacement with respect to the longitudinal location is zero. When the second derivative is zero, the inflection points can be determined. The distance between two inflection points is the buckling half-wavelength. Using this method the local length at the critical location can be determined. An example of the out-of-plane displacement at the stringer edge of a panel is given in figure 2.20, where bend and twist correspond to the maxima/minima and the inflection points respectively. Note that the inflection point does not necessarily correspond to a point of zero out-of-plane displacement.

The length (L) of a specimen in 7PB is defined by the distance between the two inflection points adjacent to the critical bending location. Additionally, an overhang (OH) is introduced to make sure the supports are not placed on the edge of the specimen. If the supports were to be placed on the edge, the specimen will simply slide off the supports under high bending loads. An overhang of $OH = 20$ mm, so a total length increase of 40 mm, is introduced. For the 4PT specimen an overhang is not needed ($OH = 0$ mm), the length of the specimen is defined by the distance between the minima and maxima adjacent to the critical twisting location.

The width (W) of the single-stringer specimen, regardless of configuration, is defined by the stringer spacing, shown in figure 2.5, and the additional overhang. If the right flange of a stringer is critical, the single-stringer specimen should have a width of $W = Pos_n - Pos_{n-1} + 2OH$. If the left flange is critical, $W = Pos_{n+1} - Pos_n + 2OH$.

A single mesh is created for the single-stringer specimen, which will be used for all possible support and loading point position combinations, and is written to the main folder. Next, for the set of variables, a subfolder is created with an additional input file that defines the position of the loading points and supports. Lastly, a main input file is created, where the other two input files are imported through an "include" statement containing the properties, boundary conditions and the analysis statement. This approach is slightly

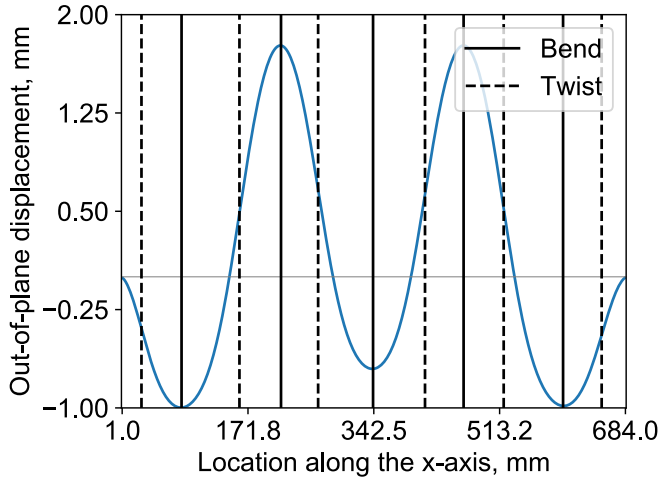


Figure 2.20: Out-of-plane displacement along the length of the stringer flange termination of a postbuckled multi-stringer panel.

different for the 7PB configuration compared to the 4PT configuration.

In the 7PB configuration, the number of variables that are studied is reduced to two: the transverse distance between the edge and the supports (S_Y) and the loading point (L_Y) as can be seen from figure 2.6. Half the single-stringer specimen area is mapped onto the multi-stringer panel, shown by the dashed lines. The out-of-plane displacement at the relative location of the central support is z_1 . In the actual test configuration, the support points are all in the same plane and do not move relative to each other. Hence, when a certain value for S_Y is chosen, different S_X locations are considered. S_X is taken such that $U_3@S_X = z_1$.

For the 4PT configuration, the supports and loading points have the same distance from the edge. As a result, S_X and S_Y are the only remaining variables, illustrated in figure 2.7. Previous work has shown that the loading points introduce a peeling effect on the stringer flange if positioned too close to the stringer. Hence, it is required to have a minimum distance of 20 mm between the loading point and the edge of the stringer flange. The design space in mm is defined by $20 \leq S_X \leq L/2 - 10$ and $20 \leq S_Y \leq (W - W_{stringer})/2 - 20$.

The displacement applied to the specimens in both configurations is the difference between the supports and the loading points ($z_{load} = z_2 - z_1$).

The design space is discretized in steps of 3 mm for both variables for which the RSS is calculated. For each combination, the difference in out-of-plane deformation is calculated with respect to the region of the multi-stringer panel. The difference is determined by calculating the Residual Sum of Squares (RSS), also known as sum of squares of deviation, as stated in equation (2.8).

$$RSS = \sum_{(i=1)}^N (W_i - w_i)^2 \quad (2.8)$$

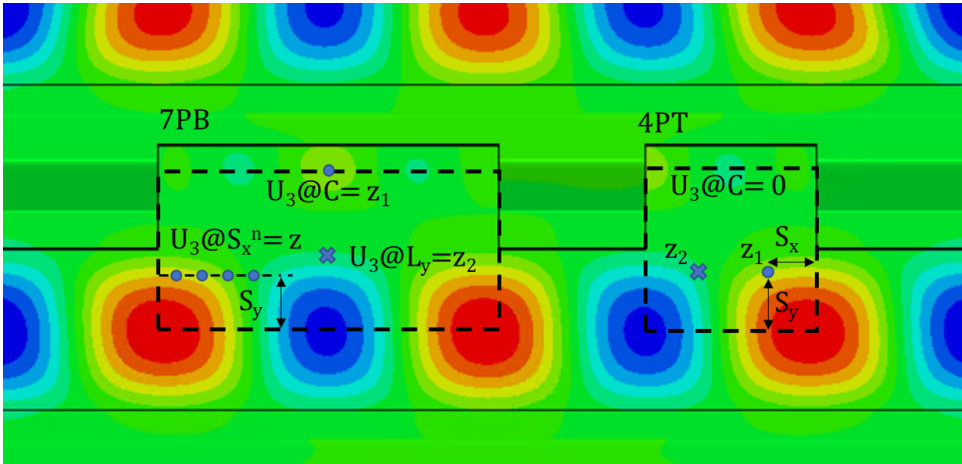


Figure 2.21: Out-of-plane displacements at the relative locations of the supports/loading points in the multi-stringer panel.

The variables W_i and w_i are the out-of-plane displacements at each node for the four-stringer panel and for the single-stringer specimen in their respective regions. The combination of the support and loading point position that results in the smallest difference is deemed to give the optimal configuration for reproducing the postbuckling shape of the panel

2.5 PREPARATIONS AND PROCEDURES FOR TESTING

The testing procedures can be broken down into a few steps. First of all, the manufacturing of the specimens. Next, the assembly includes alignment of the test equipment such that the configuration that can reproduce the critical shape is obtained. Lastly, the test procedure itself includes the loading and unloading procedures plus the measurement tools such as loadcells, digital image correlation (DIC) and C-scanning.

2.5.1 MANUFACTURING

This section discusses the manufacturing of single-stringer specimens. The coupon specimens that are tested for material characterization follow the same manufacturing procedure as described here. The composite specimens are manufactured in-house at the Delft Aerospace Structures and Materials Laboratory. Users of the methodology should adapt their manufacturing procedure according to their material system and available tools. A pre-preg roll of IM7/977-3 of 1.2m wide is used within this thesis. The sequence of the manufacturing steps is shown in figure 2.22.

In figure 2.22a, the material is cut on a vacuum table using an automated Gerber cutter. A nesting approach minimizes waste when cutting the +45, -45, 0 and 90 plies for the skin and stringer.

In figure 2.22b the plies are placed on a flat 5mm thick aluminium plate. The plate has been cleaned appropriately using ethanol and/or acetone. The plate and the stringer

insert receive three layers of a Marbo coat, with a drying time of 30 minutes in between the layers, as a release agent. The edges of the plate are taped with tacky tape such that a debulking foil can be attached. For every three skin plies, the debulking foil is closed and a vacuum is pulled and kept for 9 minutes, three minutes per ply as a rule of thumb. The stringer insert is aligned on the centre of the skin. Using gentle pressure the stringer plies are folded over the insert. The same three plies per debulking is followed.

In figure 2.22c the autoclave assembly goes into the pressurized autoclave oven. The manufacturer-recommended cure cycle should be followed. Note that the skin and stringers are cured in the same step (co-cured) and thus not bonded. The assembly consists of release film on top of the laminate followed by a breather over the whole plate and closed off with a vacuum foil. The specimen is cured at 177 degrees for 6 hours at a pressure of 7 bar.

In figure 2.22d the stringer insert, which is an assembly of three tapered solid aluminium pieces is removed from the single-stringer panel. The stringer insert is 400mm, allowing a maximum single-stringer length of approximately 380 mm.

In figure 2.22e the longer single-stringer panel is cut to the exact size. Generally, two specimens can be obtained from this single-stringer panel. To cut the panel a diamond grinder is used with a precision of 0.005 mm. During every grinding cycle, 0.1 mm of material is removed to obtain smooth and parallel edges.

After the specimens are manufactured the relevant dimensions and the mass have to be measured. The length, width, thickness at multiple locations, flange overlap and height are measured, after which the specimens can be made test ready.

For DIC a white base paint (matte/non-reflective) is applied in three thin layers with at least half an hour of drying time. The thin layers are required such that no droplets are formed over the (inclined) surfaces, which otherwise can result in faulty thickness/strain measurements. Next, using a matte black spray canister speckles are painted on top of the surface. By throttling the nozzle the speckle size can be adjusted, with some experience. The aim is a speckle diameter of approximately 3 pixels. If a specimen is 250 mm in width, with a 5MP square camera (around 2200 pixels per axis) a speckle size of $(250/2200*3) = 0.35$ mm should be used.

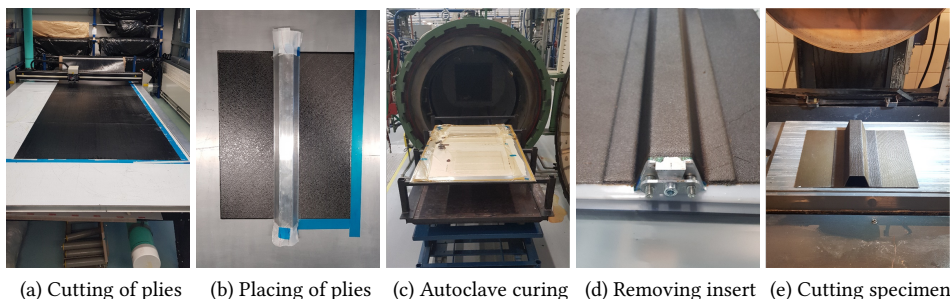


Figure 2.22: Manufacturing procedure.

2.5.2 AN ADAPTIVE MULTI-POINT TEST EQUIPMENT

An adaptive multi-point test equipment has been designed and manufactured within TUDelft. The test equipment, which is shown in figure 2.23, consists of a base-plate with a grid of holes for the placement of the support points. Any number of supports can be placed, but within this project, only two and five supports are considered for the 4PT and 7PB configurations. The loading points are attached at the top bar, which can rotate. Furthermore, the loading points are allowed to slide over the top bar to increase the loading distance. All supports and load points are equipped with 5kN ring load cells and are consistently numbered as shown in figure 2.23.



Figure 2.23: Assembly overview and loadcell numbering of the adaptive multi-point test equipment in a seven-point bending configuration.

The support points (figure 2.24) are aligned with respect to the base-plate centre using dowel pins and spacers. The placement of the dowel pins was shown in figure 2.14. The supports are clamped to the plate using the bridge clamp and screws. The tips of the loading points can be screwed in and out to adjust the height. Different spacers were used with a minimum thickness of 0.5 mm to accurately and repeatably assemble the configuration.

The whole setup is shown in figure 2.25. A 20 kN test machine by Zwick is used. Additionally, DIC, a video camera, and C-scan are used to track the response of the panel.

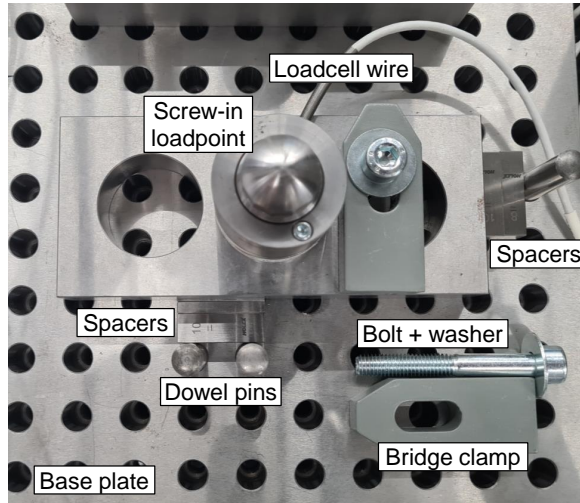


Figure 2.24: Assembly and alignment of the supports with part naming.

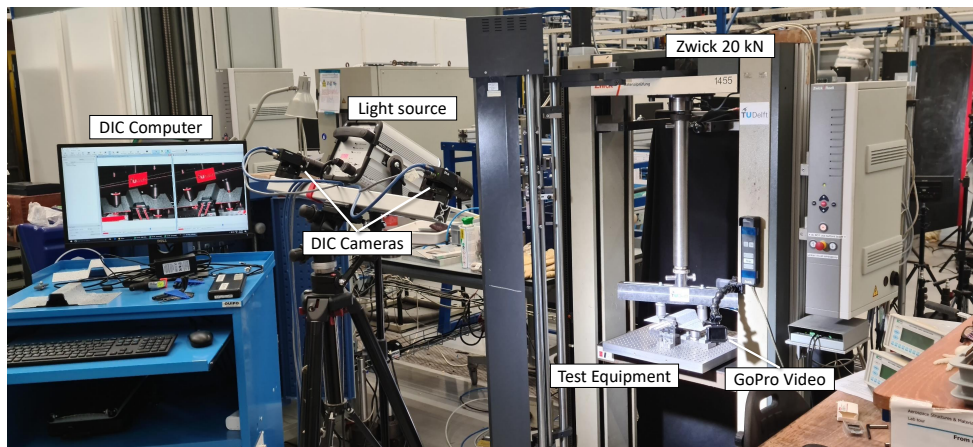


Figure 2.25: Full test set-up, including the Zwick test machine, the adaptive multi-point test equipment and the digital image correlation system (camera's, computer and light).

2.5.3 TEST PROCEDURE

For the single-stringer specimen tests, a fixed procedure is used. However, per configuration, multiple specimens are generally tested.

The first specimen is used as a baseline. This specimen is only aligned and loaded once up to full separation or when a certain set maximum load/displacement is reached. Together with the numerical predictions it is used to define the points at which the other specimens are stopped for data acquisition. The results of the other specimens can be compared to the baseline to identify the effects of reloading and/or realigning.

The remaining specimens are tested with load interruptions, where each cycle is referred to as "run<x>". During the load interruption, the specimen is removed from the fixture such that non-destructive methods can be used to assess skin-stringer separation growth. Generally, the numerical models with base interface properties underpredict the initiation load. Hence, the first stopping point is often (slightly) below the initiation point of the numerical model to show that the specimen is still in pristine condition. The last stopping point should be the same or slightly higher than the load at which the baseline single-stringer test specimen failed. The speed of separation growth tends to increase closer to the failure point. Thus at first, a larger interval can be used and a short interval when faster separation is observed.

The test is deformation-based with a loading speed of 1 mm/min. The loading speed is slower than the speed used in the numerical models (4mm/s), such that the user has time to observe and react.

The start position of the test is set such that an initial force of approximately 20 N is reached. A small preload makes sure that the specimen does not move when the alignment fixture is removed. Every run must start from precisely the same starting position, which means that the initial preload can reduce due to damage formation. If the start position is constantly changed to maintain the same preload, there is already an initial deformation that adds up to the set deformation increment.

The end of each run is set by the user as a limit on the displacement. When the limit is reached, the load should be removed instantly to limit any unstable crack growth. The load is removed at a speed of 50 mm/min until 80% of the maximum observed load in that run is reached. The remaining load on the specimen allows the engineer to investigate the specimen under deformation. In this stage, it is often possible to see the physical opening between the skin and stringer, where a camera can be used to take the images. Afterwards, the load can be removed entirely, and the specimen can be taken out of the test machine.

2.5.4 MEASUREMENT TECHNIQUES

Load cell response The load cell response uses the same format as discussed in the section on post-processing numerical results. This includes the consistency in the load cell naming, which was also shown in figure 2.23.

The specimens that undergo multiple load steps with an ever-increasing applied deformation are additionally post-processed. This is to obtain a single curve that represents the complete load response, which can be compared with the numerical response. The results of one of the specimens are shown in figure 2.26, as an example. If the specimen is well aligned each time after placing it back in the test machine, the new load curve should reach the same load at the displacement at which the previous run was stopped. The deformation

increment, where possible separation changes the compliance, is between the previous maximum deformation and the currently set new deformation limit. All the deformation increments are combined to create a single curve. This approach can also be repeated for the individual load cells to get the change in the load distribution throughout the entire testing of the specimen.

2

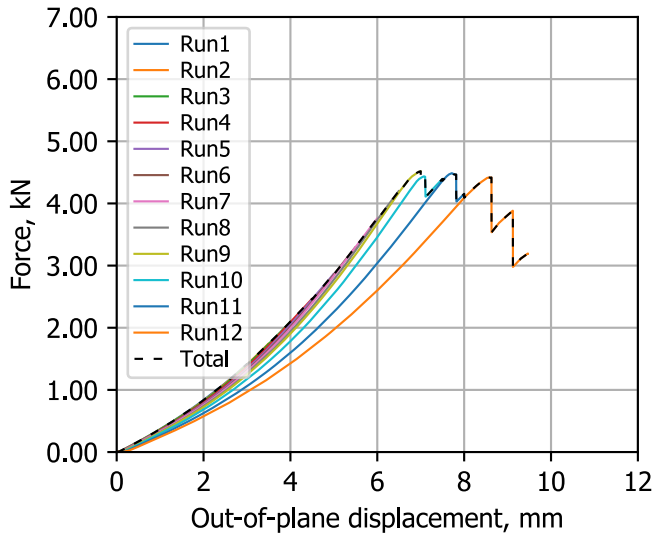


Figure 2.26: Stitching of the separate load runs.

Digital Image Correlation The DIC setup can already be seen in figure 2.25. Vic-Snap is used for image capturing, Vic3D8 for processing and VicPy for post-processing. 5MP cameras were used with the available lenses, with a focal length between 25 mm and 50mm. The stereo angle between the cameras is inversely related to the focal length. As a rule of thumb, 35 degrees is used for low focal lengths. If available, two sets of cameras should be used to capture the entire specimen deformation, as the upper loading beam blocks part of the specimen. However, the deformation of the specimen is (anti-)symmetric, and thus, the capture of one side at least can be sufficient if there is limited availability. The actual procedure for setting up and calibrating is well-described here².

DIC is used to track out-of-plane deformations. At the start of the test, a reference image is taken, and during the test, additional images are captured at a rate of 0.5 Hz. For incremental load cases, a variable capture rate was used. For example, if the specimen was loaded to 6 mm and is now reloaded up to 7 mm, the capture rate to 6 mm is 0.2 Hz, and between 6 and 7 mm, it is 0.5 Hz.

The reference image is typically the first image of the test. The deformation and strains are calculated with respect to the unloaded case. The approach used for the stitching of the

²https://www.youtube.com/watch?v=sgV1gaBe734&list=PLKk1tDmnghecJ_2Lg5Fgb4598bFFxkse

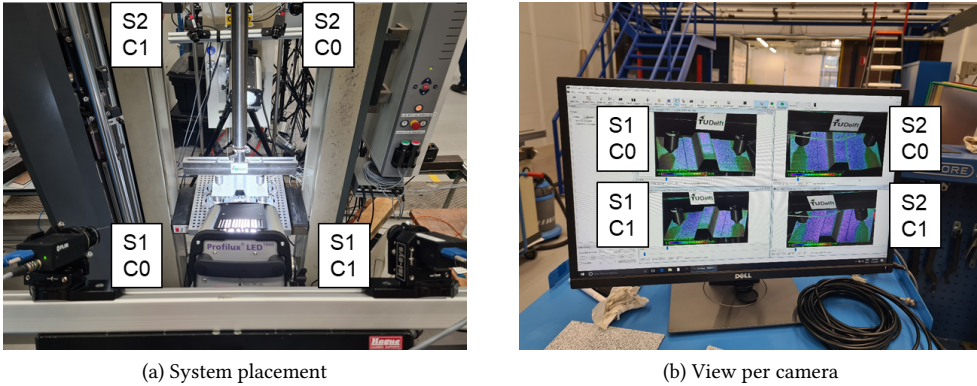


Figure 2.27: Digital image correlation.

separate load curves of each individual run is applied here. Using the previous example, the images up to 6 mm are used from the first run; from the second run, only the images taken between 6 mm and 7 mm are used. This means that deformation and strains during the second run are also calculated concerning the initial reference image of the pristine specimen. If one used the actual reference image (first image at zero displacement) from the corresponding loading run, it would ignore the strains being released in previous runs. This is an essential aspect for having usable DIC data that can be compared to the outcome of the finite element models.

C-scan A tool is required to capture the delamination at the interface during the tests. The specifics are not necessary for the methodology to work, but a minimum of 1 mm resolution is required. For the relatively thin composites, a 5 MHz probe is also strongly suggested. Initially, the Rollerform 5l64-5m was used for the first four 4PT tests, which also permits the capture of the delamination depth. Although this is a nice feature, the design of the tool was not suitable for such small and thin specimens.

A submerged c-scan apparatus was developed in-house that was more convenient to use. The setup is shown in figure 2.28a. Using through-transmission, where the sender and receiver are at opposite sides of the specimen, only the presence but not the depth of delaminations was captured.

An image of the C-scan setup is shown in figure 2.28b. The data was output as a CSV file and post-processed using Python to get the Red-Blue distinction between the separated and intact regions similar to Abaqus. The length and width of the separation fronts were measured manually such that the output could be compared to the numerical models.

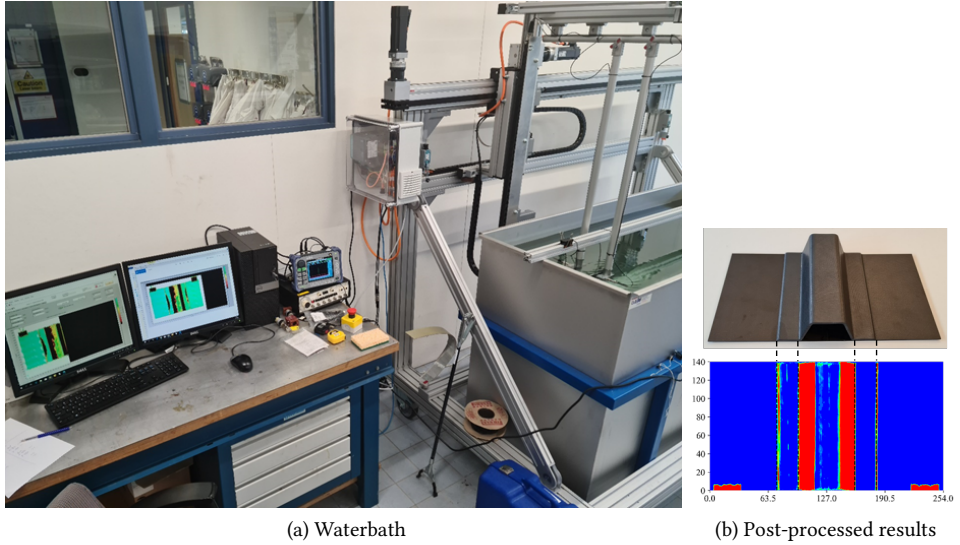


Figure 2.28: Method for C-scanning to investigate the skin-stringer separation after a test run. In b, red indicates loss of signal due to delaminations or slanted edges like the stringer webs.

2.6 CASE STUDY

An overview of the material standard material properties is given in this section. Additionally, the two design cases of a multi-stringer panel that will be investigated in this thesis are presented.

2.6.1 PROPERTIES

The material that is used to manufacture all test specimens is IM7/977-3, where the skin and stringers are co-cured. The base properties are taken from the work of Clay et al. [102]; the lamina properties are presented in table 2.1 and the unidirectional interface properties are presented in table 2.2. Note that in section 3.5, additional interface properties are shown as a result of the coupon tests.

Table 2.1: Lamina properties of IM7/977-3[102].

Longitudinal modulus	E_{11}	164000	MPa
Transverse modulus	E_{22}	8980	MPa
Shear modulus	G_{12}	5010	MPa
Poisson's ratio	ν_{12}	0.32	
Ply thickness	t	0.128	mm

Table 2.2: Unidirectional interface properties of IM7/977-3[102].

Mode I	Fracture toughness	G_{IC}	0.256	Nmm^{-1}
	Interface strength	σ_c	78.9	Nmm^{-2}
	Penalty stiffness	K_I	4.8E5	Nmm^{-3}
Mode II	Fracture toughness	G_{IIC}	0.65	Nmm^{-1}
	Interface strength	τ_c	99.4	Nmm^{-2}
	Penalty stiffness	K_{sh}	—	Nmm^{-3}
Mode I+II	Benzeggagh-kenane parameter	η_{BK}	2.07	

Table 2.3: Cross-sectional design of the stringer used in this thesis.

Flange Width	27 mm
Stringer Height	32.7 mm
Top Width	30.6 mm
Radius	5 mm
Angle	70 deg

2.6.2 DESIGN

The panel configuration used as a baseline in this research is illustrated in figure 2.5. It consists of four co-cured hat-stringers. The panel dimensions are 685 mm in the axial direction, and 770 mm in the width direction. The locations of the centre of the stringers are 66 mm, 277 mm, 493 mm, and 704 mm. This results in a width bay of 102.5 mm between the outer stringers and 107.5 between the inner stringers.

The dimensions of the stringer cross-section are defined in table 2.3, following figure 2.3.

Within this thesis, two four-stringer panel designs are considered. The skin layup is the same and the stringer layup is varied between the two designs. The different stringer designs can give alternative modes of failure. The quasi-isotropic layups are collected in table 2.4.

Table 2.4: Layup used for the thin- and thick-stringer design of a four-stringer panel.

Part design	Layup	thickness
Skin	[-45/45/0/90/-45/45]s	1.54 mm
Thin-stringer design	[45/-45/0/90/45/-45]s	1.54 mm
Thick-stringer design	[45/-45/0/90/45/-45]2s	3.07 mm

3

COUPON TESTS FOR CROSS-PLY INTERFACE CHARACTERIZATION

The coupon tests for material characterisation are at the lowest level of the building block approach. Coupon tests are standardised to obtain specific material properties. This chapter turns away from standard unidirectional composites. Instead, it considers the actual layup of the design of the single-stringer and multi-stringer panels with a cross-ply interface. The critical strain energy release rates are determined using a double cantilever beam, mixed-mode bending, and end-notched flexure tests. A cross-ply interface leads to an increase in fracture toughness, usually less present in unidirectional coupons. A bilinear curve is fitted through the test results to obtain the initial and steady-state fracture toughness and the fracture processing zone. Especially in a double cantilever beam, the fibre bridging causes a toughness increase. A superposed bilinear law models the initiation and the transition zone to steady-state in the cohesive zone. The proposed method of Davila et al.[56] is adapted to decouple the superposed laws. Cohesive elements in the second set only release energy after the first set has completely degraded. The DCB models with this trilinear law correctly reproduce the R-curve response. However, the mixed-mode bending tests are shown not to be capable of characterising R-curve effects under a fixed mixed-mode, and therefore, multiple sets of material properties are proposed.

3.1 INTRODUCTION

MATERIAL characterization[36] is the first level of the building block pyramid in figure 2.1. Generally, the material properties are known from the material supplier/-manufacturer. Otherwise, a material characterization study has to be done, especially for properties that are affected by the application. Specifically for composite laminates, a cross-ply interface can increase the fracture toughness compared to a unidirectional interface[47–65].

This chapter presents the setup for the coupon tests including the data reduction schemes. The method for retrieving a bilinear curve to represent the resistance curve effect is shown. The bilinear curve consists of an initiation point, a linear increase of the fracture toughness and a steady-state toughness. This method is applied to all the tests: DCB[39], ENF[40] and MMB[41, 42]. A mixed-mode relationship can be determined from the initiation and steady-state values through a Benzeggagh-Kenane (B-K)[43] approximation.

For the implementation of the interface properties with regard to R-curve effects different methods exist. For example, a piecewise linear [58, 64, 65], trilinear[56, 60] or trapezoidal[59] representation. The trilinear method proposed by Dávila et al.[56] considers the general bilinear cohesive elements as described in chapter 2. By superposing two elements, both with their own bilinear law, a trilinear law is created that is able to capture the R-curve effects. An adaptation is proposed in this chapter to ensure a more independent response of the two sets of elements.

Chapter goals

- **section 3.2:** To show the coupon design and manufacturing.
- **section 3.3:** To characterise the interface properties for a quasi-isotropic layup and investigate the failure characteristics. DCB, ENF, MMB.
- **section 3.4:** To determine the mixed-mode interaction based on all test results, considering also the R-curve effects. This includes an adaption to the method of superposing bilinear cohesive laws and material parameter fitting through FE.
- **section 3.5:** To present the outcome of the coupon tests in a table containing the bilinear and superposed trilinear cohesive properties to be used for FE.
- **section 3.6:** To discuss the validity of the mixed-mode bending tests.

3.2 COUPON DESIGN AND MANUFACTURING

The design considerations for coupon specimens are important to obtain a correct set of properties. This design parameters section is divided into the laminate definition, the manufacturing process and the dimensions, and lastly the calculations.

The interface used for the designs in this thesis is -45/+45, reported in section 2.6.2. For the coupon tests, the design where the skin and thin stringer have an equal thickness is chosen: [-45/45/0/90/-45/45]_s and [45/-45/0/90/45/-45]_s, respectively. This results in an anti-symmetric layup for the full coupon laminate.

Common laminate properties that are used throughout the material characterization are the Young's modulus (E_{11} and E_{22}). As non-unidirectional laminates are used, the modulus

of the actual laminate has to be calculated, which is done using classical laminate theory. The thickness of the sublaminates (h) and the inverse of the ABD stiffness matrix (abd) are used, following equation (3.1).

$$E_{11} = \frac{1}{ha_{11}} = E_{22} = \frac{1}{ha_{22}} \quad (3.1)$$

Additionally in the coupon tests, the properties γ and χ are introduced. These are calculated according to equation (3.2) and equation (3.3), respectively. γ is used to correct the transverse modulus and χ to correct the crack length[41].

$$\gamma = 1.18 \frac{\sqrt{E_{11}E_{22}}}{G_{13}} \quad (3.2)$$

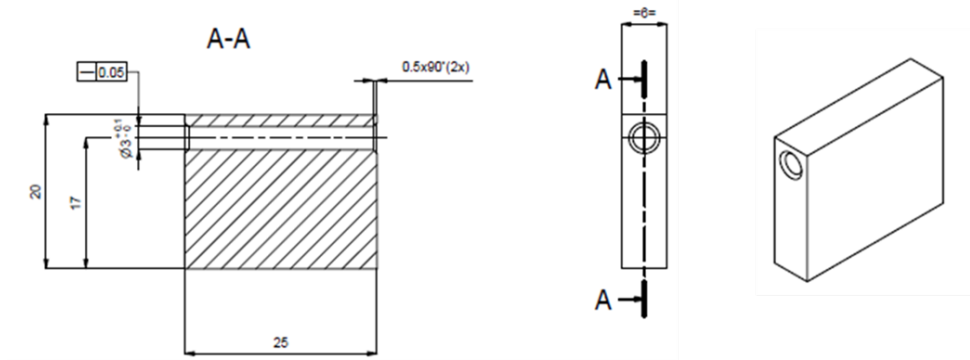
$$\chi = \sqrt{\frac{E_{22}}{11G_{13}} \left[3 - 2 \left(\frac{\gamma}{1+\gamma} \right)^2 \right]} \quad (3.3)$$

The coupon specimens were manufactured under the same conditions and procedure as described in section 2.5.1. Additionally, aluminium loading blocks were aligned via Teflon blocks as shown in figure 3.1 and bonded onto the DCB and MMB coupons using LOCTITE®EA 3430. The loading blocks were tumbled, grid blasted and properly cleaned, similarly the coupons were sanded and cleaned, all to assure maximum adhesion. The load blocks were redesigned in order to ensure proper alignment with the fixture and also to have the axis of loading close to the mid-plane of the laminates. The CAD drawings are illustrated in figure 3.2.



Figure 3.1: Bonding of the blocks onto the coupons specimen using LOCTITE®EA 3430 and Teflon alignment fixtures.

The paint was applied to the sides of the coupons prior to attaching the load blocks for ease of manufacturing. Three thin layers of white paint with proper drying assures a brittle paint without chipping to accurately follow the delamination growth. Additionally, the paint was cut with a sharp knife to mark the distance from the insert, which is shown in figure 3.3.



Surface treatment: Tumble finish (NL: 'trommelen')

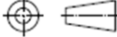
 TU Delft AE DASML	Maateenheid: mm	Drawn: dsrujtenbeek	Third angle projection:
	Tolerances according: ISO2768-mH	Date: 13/07/21	
	File: 0101-08-20_R00 MMB tab.idw	Material: Al8082-T6 (51ST)	Revision: 0
Name: MMB tab			Sheet: 1/1 Format: A3

Figure 3.2: CAD drawing of load blocks for the coupon specimens.

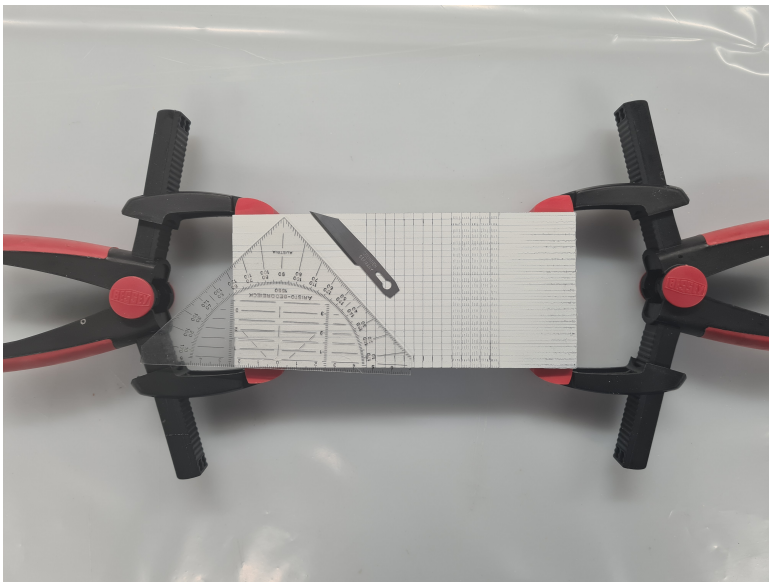


Figure 3.3: Marking of the coupon specimens with the small 1 mm increments up to 25 mm and the large 5 mm increments.

All coupons, for which the parameterised models were shown in section 2.3, have the same layup and dimensions: $h = 1.536$, $W = 125$, $L = 25$ mm. The insert length is kept constant at $a_0 = 25$ mm. PTFE foil of 50 micrometres was used for the insert, deviating from the recommended 13 micrometres, as this was at hand in the laboratory. The ASTM standard[41] on page 5 section 8.2 mentions:

"A nonadhesive insert shall be inserted at the midplane of the laminate during layup to form an initiation site for the delamination. The film thickness shall be no greater than 13 μm [0.0005 in.]. Specimens should not be precracked. By not precracking, an initiation value free of fibre bridging may be obtained."

Deviating from the standard with the thicker insert affects primarily the results for initiation. The thicker insert creates a resin pocket at the initial delamination tip that increases the initial fracture toughness[103, 104]. This could be removed by precracking the specimen, but as mentioned in the standard this influences the fibre bridging behaviour. Especially because precracking is often done using the DCB setup or wedging the specimen. This would create initial pure mode I toughening effects after which the specimen would be tested in a mixed-mode condition, for example. Therefore the specimens are also not precracked.

3.3 COUPON TESTING

This section includes the setup for each coupon, as well as the data reduction scheme, the force-displacement and Critical Strain Energy Release Rate (CSERR) results, and the fracture mechanisms. For the coupon tests, a Zwick 10 kN test machine is used with a 1 kN load cell. A camera observes the delamination front, where the images can be related to the force and displacement data of the machine. The images are manually filtered to have a data point every 1 mm of delamination length, with the exception of crack jumps.

3.3.1 MODE I: DOUBLE CANTILEVER BEAM

The setup that is used for the DCB tests is shown in figure 3.4. The clamps pull the loading block in the direction normal to the plane of the specimen. Delamination starts at 25 mm and extends to the right. The specimens are precracked and reloaded according to the standard[39].

The force-displacement results of the five DCB tests (DCB_1-DCB_5) are plotted in figure 3.5a. The dots correspond to measurements of the delamination length. Generally for DCB tests, after initiation, the load will decrease. For this quasi-isotropic layup, the increase in the fracture toughness during propagation results in a load plateau followed by a decrease. Some load/delamination jumps are observed similar to [47], but overall the propagation is smooth.

To determine the CSERR from the force-displacement results and the delamination length the Modified Beam Theory (MBT) is used. This theory, presented in equation (3.4), is the most conservative approach in the ASTM standard[39]. Within this approach, there is a correction for the effective delamination length, Δ . Δ is approximated by a linear fit of the delamination length and the cube root of the compliance, which is presented in figure 3.5b.



Figure 3.4: Setup for double cantilever beam. The load is applied on the left with the bottom clamp moving downwards.

Δ is taken at the intercept of $C^{\frac{1}{3}} = 0$, which is illustrated in figure 3.5b for DCB_2.

$$G_I = \frac{3P\delta}{2L(a + |\Delta|)} \quad (3.4)$$

The outcome of the data reduction, the mode I CSERR, can be found in figure 3.6. The dots correspond to the instantaneous CSERR at each image. The blue line and area correspond to the mean and standard deviation (1σ) of the sample set. The horizontal dashed-dot line corresponds to the BK estimate of the CSERR based on the properties in table 2.2. The dashed red line is a bilinear approximation of the resistance curve response.

For the bilinear approximation, it is assumed that there is an initial fracture toughness G_0 , a processing zone with a linearly increasing G , and a steady-state where G_{SS} is constant. A bilinear curve fit with equation (3.5) makes it possible to obtain these distinct values. In the equation, the crack increase da is always positive. The slope (k) indicates how fast the CSERR increases when the delamination extends. At some point, $G_0 + kda$ exceeds the steady-state value, at which G will become G_{SS} .

$$G = \min(G_0 + |k|da, G_{SS}) \quad (3.5)$$

The length of the processing zone can be calculated from these three values using equation (3.6). A single fit is done through the complete dataset of all 5 specimens per test configuration. This gives each test set a single value for the initiation and steady-state CSERR as well as the processing zone length.

$$L_{FPZ} = \frac{G_{SS} - G_0}{k} \quad (3.6)$$

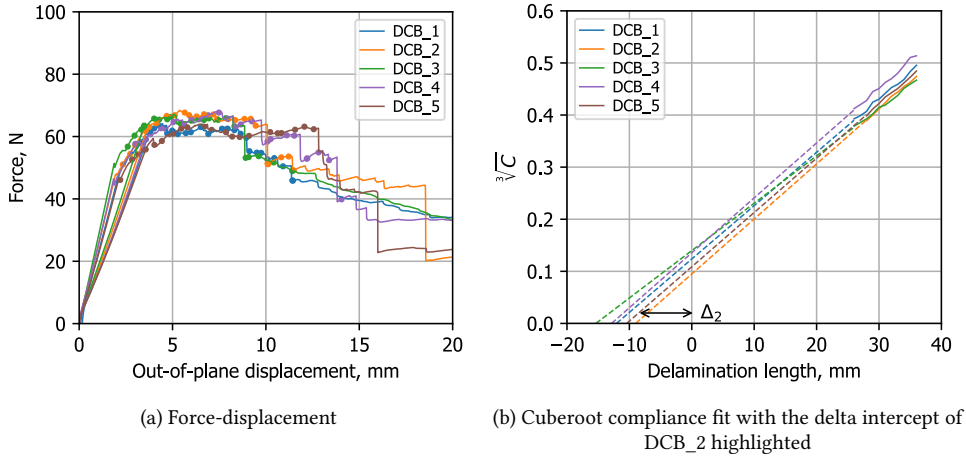


Figure 3.5: Double cantilever beam: force, displacement and compliance results.

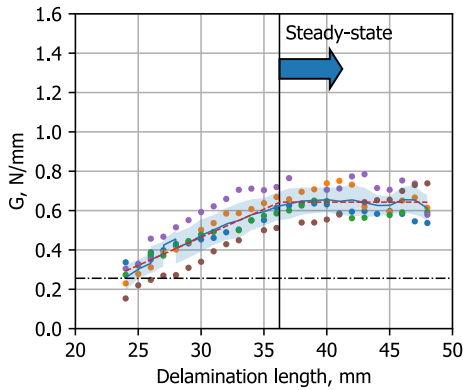


Figure 3.6: The bilinear approximation of the Mode I CSERR from the DCB tests in red. The dots represent the measurements, the blue curve and area show the mean and steady-state of all the results.

A closeup of the coupon specimen is shown for a delamination length of 40 mm in figure 3.7. There is no observed delamination migration, but there is significant fibre bridging in the wake of the crack tip. When a bundle of these larger fibres break a sudden jump in the load was observed in figure 3.5a. This fibre bridging is often observed in mode I loaded multi-directional interfaces [48, 56, 62], which is caused by transverse matrix cracking[52].

3

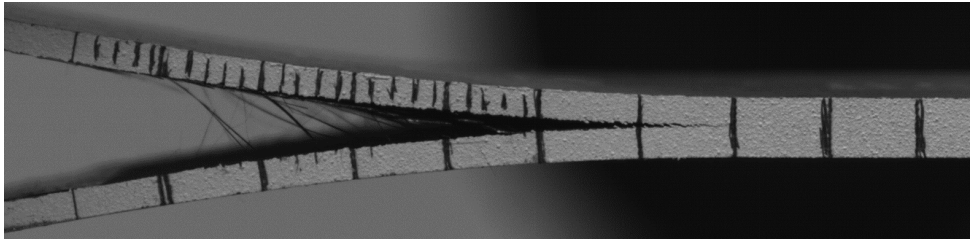


Figure 3.7: Delamination front of DCB 3 with bridging fibers and no delamination migration.

To summarize the outcome, the initiation value is approximately 0.26 N/mm, only 1.5% higher than the unidirectional. The increase in fracture toughness happens over a length of 12.1 mm until it reaches a steady value of 0.64 N/mm, an increase of 150%.

3.3.2 MODE II: END-NOTCHED FLEXURE

The setup for the ENF test is shown in figure 3.8. The central roller pushes down, which leads to the bending of the skin and a pure mode II delamination. The delamination is between the left and central roller. The measurements can be done up to the point when delamination reaches the central roller, after which the results are invalid.

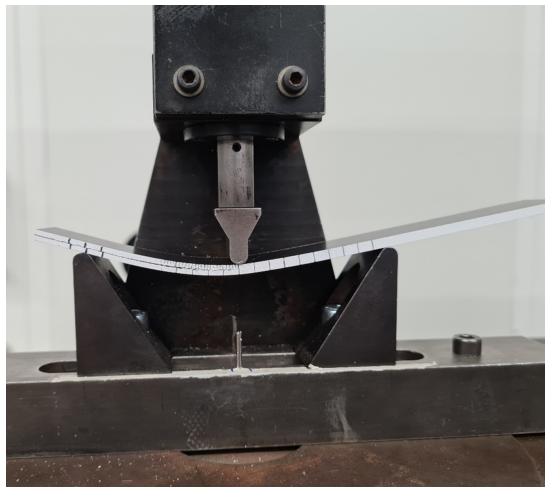


Figure 3.8: Set-up for the end-notched flexure test with the top roller pushing downwards.

Prior to the fracture tests, the flexural stiffness ($E2f$) of each coupon is measured[105]. The compliance calibration is performed by shifting the specimen to change the delamination length without any fracturing. Deviating slightly from the standard, the compliance calibration was performed at delamination lengths of 20, 25 and 30 mm. The standard prescribes 20, 30, and 40 mm. However, all coupons were manufactured together with an insert length of 50 mm. This left ample space for the 40 mm calibration. Still, three measurements are used for the linear fit, albeit with reduced accuracy. The force-displacement response of the first specimen ENF_1 is shown in figure 3.9a for the three delamination lengths. The compliance is measured as the linear fit of the results above 90 N. The compliance as a function of the delamination length cubed is shown in figure 3.9b. Another fit per specimen is used to solve for the variables A and m in the equation: $C = A + ma^3$. " A " can then be used in equation (3.7) to obtain the flexural stiffness.

$$ENF : \quad E2f = \frac{L_R^3}{4ALh^3} \quad (3.7)$$

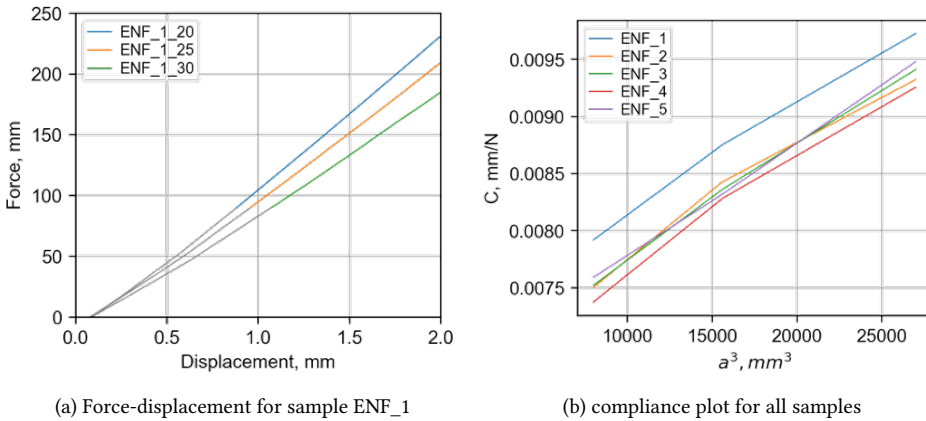


Figure 3.9: Compliance calibration plots for ENF coupons.

The data reduction scheme to calculate mode II CSERR is presented in equation (3.8). The slope m of the compliance calibration, equation (3.7), is used. Generally, only the peak force is used to calculate the CSERR, because delamination often extends directly to a point close to the central roller. For these more compliant specimens due to the quasi-isotropic layup as opposed to unidirectional, delamination initially extended only 10-15 mm.

$$G_{II} = \frac{3mP^2a^2}{2L_R} \quad (3.8)$$

The force-displacement and CSERR results of all five ENF coupon specimens (ENF_1-ENF_5) are shown figure 3.10. A large load drop is observed close to 5 mm of displacement, resulting in a crack increase of 10-12 mm. The CSERR at initiation is almost twice as high as for the unidirectional results, represented by the dashed-dot line. This can be an effect of the thicker insert, which would make the results questionable. Furthermore, it was not possible to perform a bilinear fit as the results seem to be constant at around 1.2 N/mm.

3

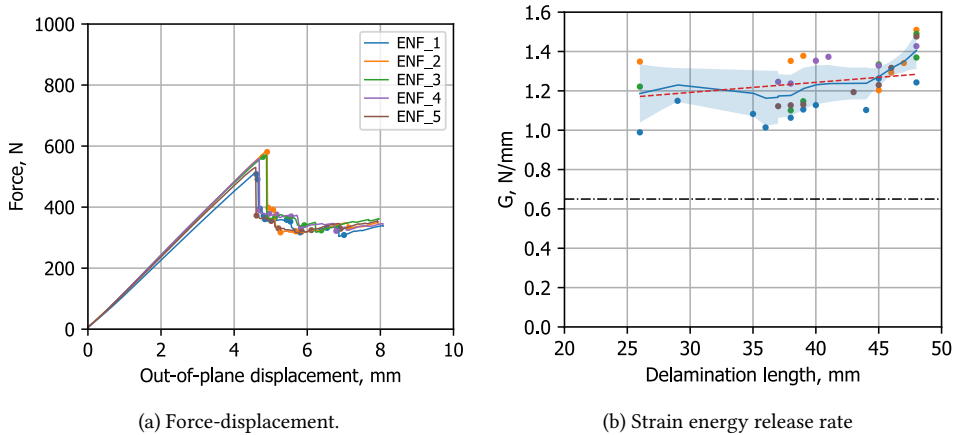


Figure 3.10: End-notched flexure results.

The delamination front after the first load drop, with another 10 mm of available stable delamination growth, is shown in figure 3.11. As opposed to the DCB (figure 3.7) there is more of a sawtooth behaviour at the interface, which can be related to delamination migration. However, the interface with the insert remains the dominant interface.

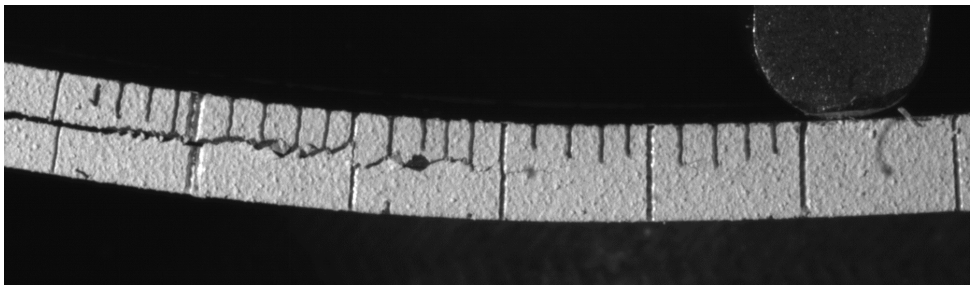


Figure 3.11: Delamination front of ENF 4 with a zigzagging delamination migration. The horizontal/sliding displacement between the two lines (mode II) can be observed on the left.

3.3.3 MODE I+II: MIXED-MODE BENDING

The MMB setup is shown in figure 3.12, where the blue horseshoe pushes down on a roller creating a lever acting on the top beam of the coupon. Delamination growth is between the load blocks on the left and the central roller at the top of the coupon.

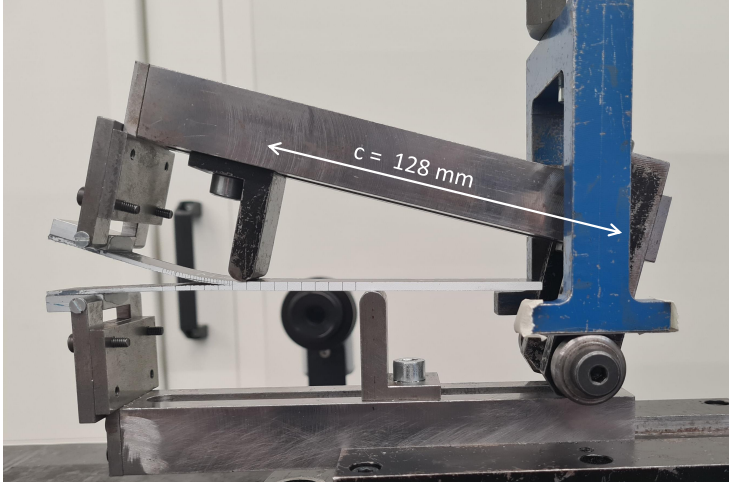


Figure 3.12: Set-up for mixed-mode bending (20%) with the right side pushing downwards to create a lever opening the left side of the coupon.

The length of the lever (c_0) in the mixed-mode bending tests is inversely related to the mixed-mode conditions and calculated with equation (3.9). The parameter α is related to the mixed-mode condition, shown in equation (3.10), and β is a delamination length correction defined in equation (3.11).

$$c_0 = \frac{12\beta^2 + 3\alpha + 8\beta \sqrt{3a}}{36\beta^2 - 3\alpha} L_R \quad (3.9)$$

$$\alpha = 1/MM - 1 \quad (3.10)$$

$$\beta = \frac{a + \chi h}{a + 0.42\chi h} \quad (3.11)$$

The weight of the lever introduces an additional force at its centre of gravity. The lever length is adapted based on the centre of gravity and the ratio of the (estimated) load (P_{est}) and the gravitational force (P_g). This is shown in equation (3.12).

$$c = \left(1 + \frac{P_g}{P_{est}}\right) c_0 - \frac{P_g}{P_{est}} c_g \quad (3.12)$$

The centre of gravity (c_g) is itself dependent on the lever length. The weight and centre of gravity of the lever, measured from the top roller similar to how c is defined, is w_{body} 12.5 N and $c_{body} = 44.3$ mm. The total mass of the lever is $P_g = 17.93$ N, which enables the calculation of the centre of gravity based on the lever length in equation (3.13).

$$c_g = \frac{c_{body}w_{body} + c(P_g - w_{body})}{P_g} \quad (3.13)$$

By inserting equation (3.13) into equation (3.12) and rewriting it, c can be obtained corrected for c_g in equation (3.14).

$$c = \frac{\left(1 + \frac{P_g}{P_{est}}\right) c_0 - \frac{c_{body}w_{body}}{P_{est}}}{1 - \frac{(P_g w_{body})}{P_{est}}} \quad (3.14)$$

The peak force can be calculated, but this does not include the fact that the presence of the gravitational force lowers the peak load of the machine. However, obtaining the exact mixed-mode condition is not necessary. As long as sufficiently spaced mixed-mode conditions are tested, a mixed-mode law can be fitted. It is important that the actual condition is calculated after the tests. The lever lengths are the following: $MMB_{20\%} = 128$ mm, $MMB_{50\%} = 48.5$ mm, and $MMB_{80\%} = 28$ mm.

In the MMB, the CSERR components are calculated separately, considering the gravitational force. The mode I component is calculated using equation (3.15) and mode II using equation (3.16). These values total the CSERR and can be used to calculate the actual mode-mixity using equation (3.17).

$$G_I = \frac{12 [P(3c - L_R) + P_g(3c_g - L_R)]^2}{12L^2h^3L_R^2E_2f} (a + \chi h)^2 \quad (3.15)$$

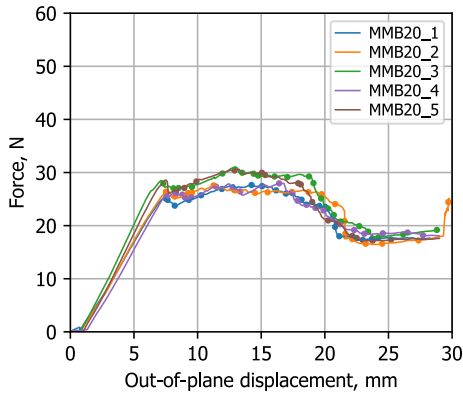
$$G_{II} = \frac{9 [P(c + L_R) + P_g(c_g + L_R)]^2}{12L^2h^3L_R^2E_2f} (a + 0.42\chi h)^2 \quad (3.16)$$

$$MM = \frac{G_{II}}{G_I + G_{II}} = \frac{G_{II}}{G_{tot}} \quad (3.17)$$

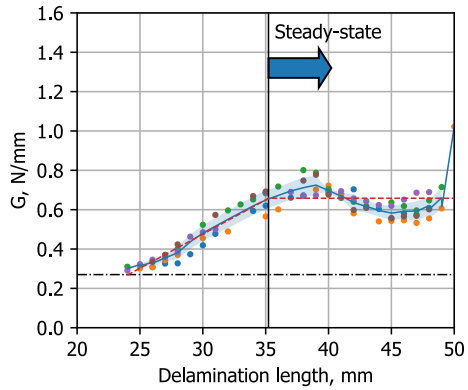
Within this thesis, it was chosen to use the outcome of the ENF compliance tests as an input for the MMB data reduction. The tests were all performed in the same series and the specimens were cut from the same panel. The closest neighbour interpolation was used to find the E_2f value corresponding to an ENF specimen that has the nearest thickness to the MMB specimen.

The MMB results for the mixed-mode conditions of 0.2, 0.5 and 0.8 are plotted in figure 3.13. The approach of equation (3.5) is used for the bilinear curve fit of the CSERR results. For MMB20 the propagation is very stable with minimal load jumps, which results in a low standard deviation, between 0.01 and 0.07 throughout propagation. For a higher mixed-mode condition G_0 and G_{SS} increase and the fracture processing zone length itself shortens.

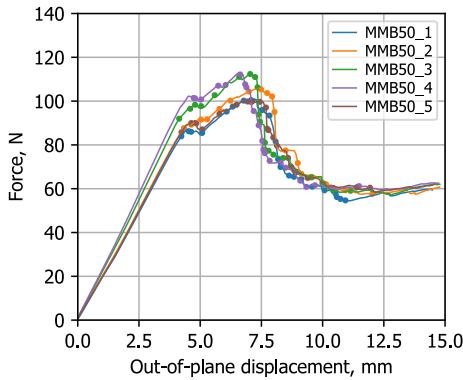
An initial increase is followed by a decrease of the measured G due to delamination migration. The migration is visible in all cases as shown in figure 3.14, which is common in these types of tests[61, 62]. During migration effectively the bottom plies of the upper laminate become part of the lower laminate. This results in a more compliant upper beam as well as a mismatch in the bending properties between the lower and upper beam. If the coupon is designed for this mismatch it can be accounted for, but because of the migration,



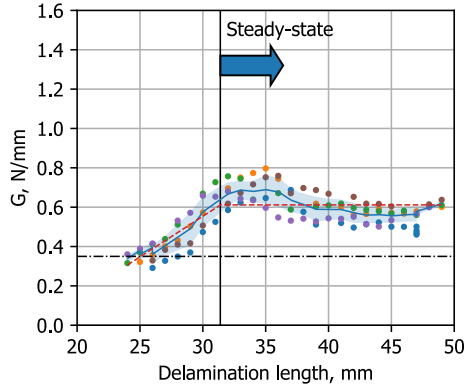
(a) Force-displacement for MMB 20%



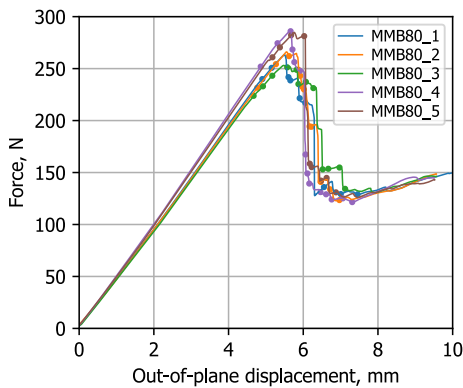
(b) Energy release rate for MMB 20%



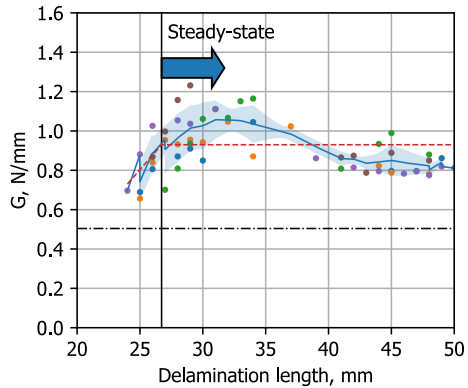
(c) Force-displacement for MMB 50%



(d) Energy release rate for MMB 50%



(e) Force-displacement for MMB 80%

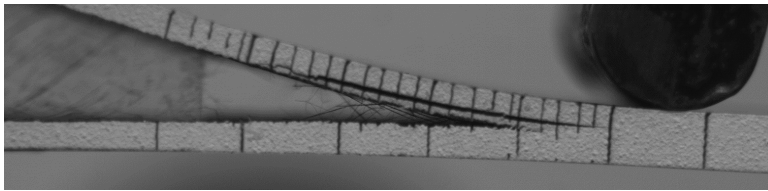


(f) Energy release rate for MMB 80%

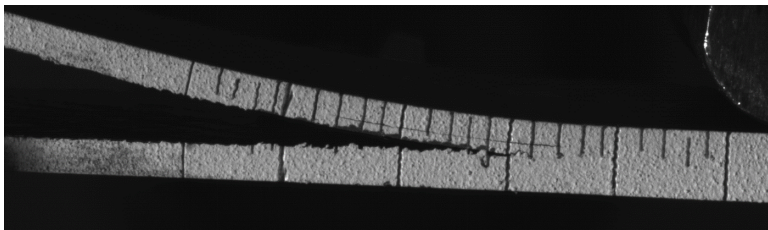
Figure 3.13: Mixed-mode bending results for all mixed-mode conditions.

this is not possible. Despite these migration effects, the middle interface also continued to propagate lagging behind the migrated delamination front. For consistency, it was chosen that the delamination length was always measured with respect to the delamination front of the original interface. The energy that is released in the migrated interface is simply accounted for in the R-curve properties.

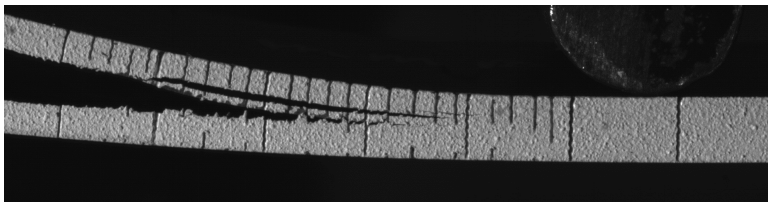
3



(a) MMB20 4



(b) MMB50 5



(c) MMB80 4

Figure 3.14: Delamination fronts of MMB coupons with both fiber bridging. An additional delamination is present in the top sublaminates besides the growing delamination at the original interface.

For the lower mixed-mode conditions the test forces are relatively low with respect to the gravitational force of the lever. Therefore it is important to calculate the actual mixed-mode condition, as this is affected by the ratio of P_g/P_{test} (e.g. for MMB20_3: $17.93/28=64\%$). The actual mixed-mode conditions are 0.2, 0.44, and 0.76 according to equation (3.17).

3.3.4 INVESTIGATION OF THE DELAMINATION SURFACE OF THE COUPON SPECIMENS

To investigate the interface the DCB and MMB specimens were loaded under DCB conditions to separate the upper and lower beams. A loading rate of 50 mm/s was selected as a huge displacement was necessary for full separation. The ENF were separated by shimming the already separated interface and manually opening it, because the ENF coupons do not have any loading blocks.

The lower beams of the separated coupons are shown in figure 3.15. The DCB showed significant fibre bridging, leading to distinct fibres being visible in the +45 direction. Only the DCB specimen did not show delamination migration. All other specimens showed migration. Due to a peeling edge effect and the fact that 45 fibres terminate at the edge, delamination is triggered. Because the specimen itself is 25 mm in width and the ply is angled at 45 degrees, migration occurs over a region of 25 mm. There is no observable difference in the migration patterns between the MMB/ENF specimens. The migration length is the shortest from 45 to 0 as this is fully matrix dominated. This is as opposed to the migration arresting effect of the 90 plies, as the direction of growth is parallel to the fibre.

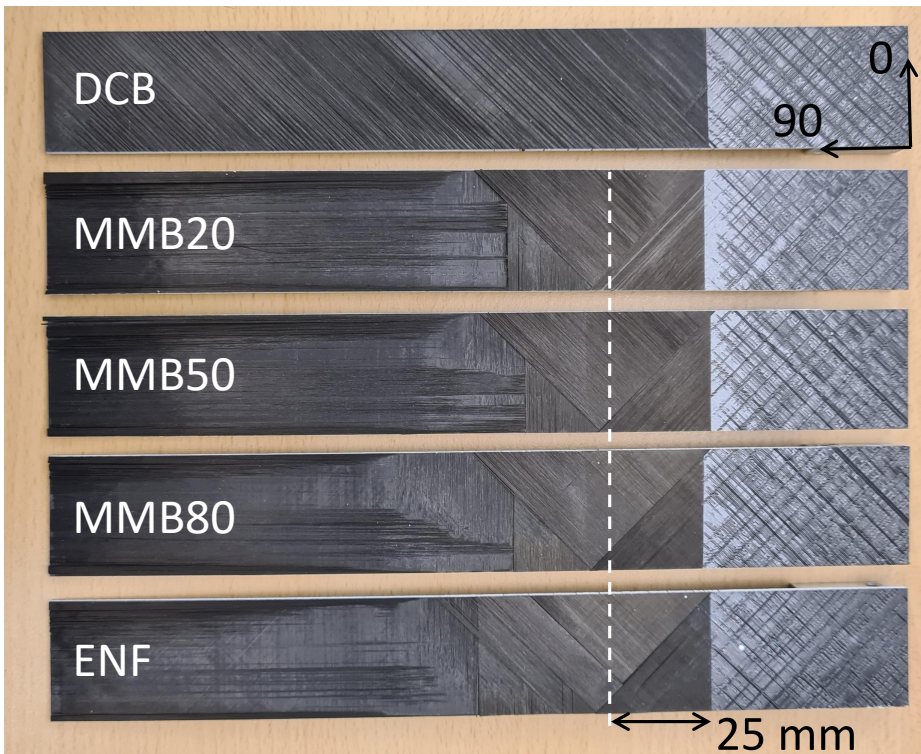


Figure 3.15: Interface of each of the coupon specimens showing the migration patterns, except for DCB. All specimens were tested up to an increase of 25 mm, the rest of the migration is caused by the DCB loading to fully open the interface.

3.3.5 OVERVIEW OF THE COUPON TEST RESULTS AND MIXED-MODE RELATION

The outcome of the mixed-mode conditions is presented in table 3.1. The material parameters will be used as an input for the numerical models that follow a cohesive material model with a Benzeggagh-Kenane mixed-mode law[43], which is explained in section 2.3.1.

Table 3.1: Interface toughness and fracture processing zone length for all mixed-mode conditions.

	DCB	MMB 20%	MMB 50%	MMB 80%	ENF
Mode-mixity	0	0.2	0.44	0.76	1
G_0 , N/mm (1σ)	0.26 (0.06)	0.30 (0.01)	0.34 (0.02)	0.7 (0.10)	1.19 (0.14)
G_{SS} , N/mm (1σ)	0.64 (0.07)	0.66 (0.07)	0.61 (0.07)	0.93 (0.11)	1.29 (0.08)
L_{fpz} , mm	12.1	11	7	3	1
G_{SS}/G_0 , +%	150	120	80	33	8

The general BK law is repeated in equation (3.18), where G_I and G_{II} are taken as the direct results of the DCB and ENF results. The BK exponential η is determined by minimizing the difference between the MMB results and $G(M)$. The actual mixed-mode conditions are used as presented in table 3.1, calculated after the tests were performed, to compensate for any additional influence of the weight of MMB lever.

$$G(M) \approx G_I + (G_{II} - G_I)M^\eta \quad (3.18)$$

A BK fit is obtained separately for both the initiation ($\eta_0 = 2.77$) and Steady-state ($\eta_{SS} = 3.33$) results. The data points and fit are shown in figure 3.16, as well as the fit of the unidirectional tests. As expected, the increase in mode II also leads to an increase in the fracture toughness. Up to a mode-mixity of 50% there is little difference in fracture toughness between the unidirectional and the quasi-isotropic laminates. The relative increase of the fracture toughness is greater for mode I loads, which is accompanied by a larger fracture processing length as presented in table 3.1.

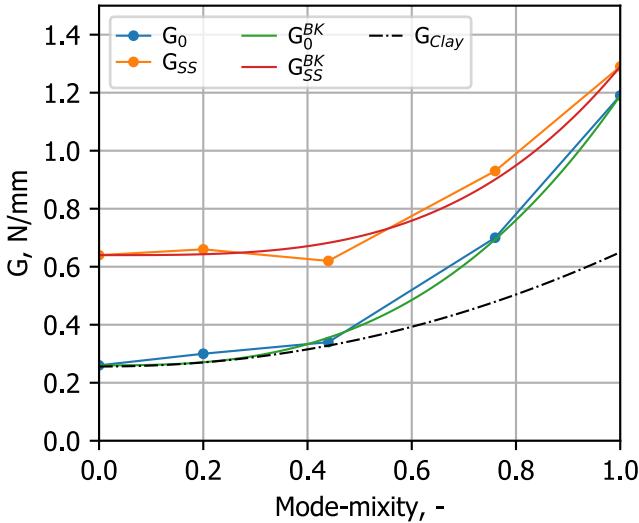


Figure 3.16: Benzeggagh-Kenane fit through the mixed-mode strain energy release rate values for unidirectional (G_{clay}), initiation(G_0) and steady-state(G_{SS}).

3.4 DETERMINATION OF THE TRILINEAR LAW

Within the coupon tests, there was fibre bridging and delamination migration that led to an increase in fracture toughness. To capture these effects in FE would require large models with a complicated mesh. This might be possible for these small coupons, but for larger specimens such as single- and multi-stringer panels, this is too costly. Instead, these R-curve effects are included purely for the increase in fracture toughness for the main interface. By superposing two bilinear cohesive laws a trilinear law is obtained[56] which includes the initiation and steady-state behaviour. Initiation will be covered by the **primary**(Pri) law and toughening by the **secondary**(Sec) law. The approach is easy to implement in the models, only requiring a second material definition, cohesive section assignment, and output request, following section 2.3. Furthermore, Dávila et al. suggests adding the following line to the input file to simply copy the already existing cohesive elements with the same nodal definitions, but with their own unique element IDs.

```
*ELCOPY, element shift=1000000, oldset=COH,
new set=COH_Bridge, shift nodes=0
```

The trilinear law following the concept of Dávila et al.[56]a is illustrated in figure 3.17a. This method has the requirement that the opening at initiation (d_0) of the primary law matches with the initiation in the secondary law. In this thesis, an alternative requirement is proposed. The second cohesive element is activated only when the first one has degraded completely. In other words, the opening at the initiation of the secondary law (d_0^{Sec}) is equal to the opening at the failure of the primary law (d_{end}^{Pri}). This can be visualised in figure 3.17b.

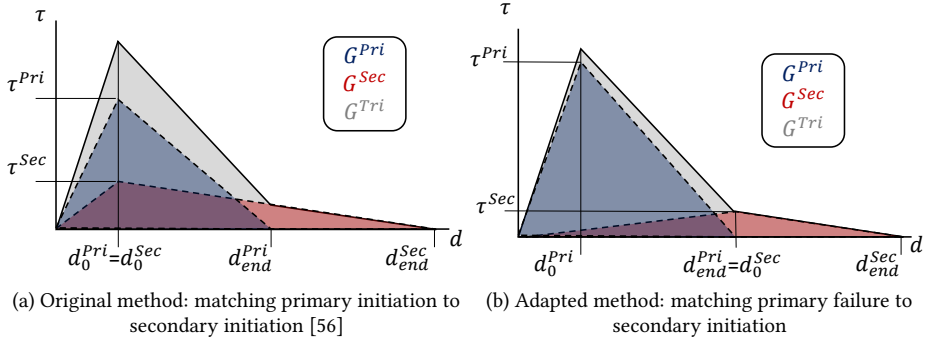


Figure 3.17: Superposing bilinear laws to obtain a trilinear cohesive response.

All together this change is to have the two laws operate more independently of each other. The secondary cohesive element is not releasing any energy before the primary element has completely failed. Additionally, the interface strength of the primary law does not need to be changed with respect to the original bilinear law; The strength of the secondary law at initiation of the primary is much smaller due to the low stiffness.

The determination of the material properties for the secondary law is broken down into four steps:

1. **section 3.4.1:** Determine the critical fracture toughness and the BK fit.
2. **section 3.4.2:** Determine the mode I interface strength using an FE model of a DCB to study the fracture processing zone length.
3. **section 3.4.3:** Determine the mode I penalty stiffness.
4. **section 3.4.4:** Determine the mode II interface strength/stiffness, adding the requirement for the secondary law to also be thermodynamically consistent[106].

3.4.1 THE CRITICAL FRACTURE TOUGHNESS

The fracture toughness of the primary law is defined by the G^0 and η^0 that has been obtained in section 3.3.5:

$$G_i^{Pri} = G_i^0 \quad i = I, II \quad (3.19)$$

$$\eta^{Pri} = \eta^0 \quad (3.20)$$

The toughness in the secondary law is chosen such that when superposed with the primary law it is equal to the steady-state test results:

$$G_i^{SS} = G_i^{Pri} + G_i^{Sec} \quad i = I, II \quad (3.21)$$

or

$$G_i^{Sec} = G_i^{SS} - G_i^{Pri} \quad i = I, II \quad (3.22)$$

For the superposition, two sets of BK-laws are needed to approximate the steady-state results. Therefore equation (3.23) is solved for η^{Sec} with all other variables already known.

$$G^{SS}(M) \approx G_I^{Pri} + (G_{II}^{Pri} - G_I^{Pri}) M^{\eta^{Pri}} + G_I^{Sec} + (G_{II}^{Sec} - G_I^{Sec}) M^{\eta^{Sec}} = G^{Pri} + G^{Sec} \quad (3.23)$$

The final results of the primary(G_{pri}), secondary(G_{sec}) and superposed ($G_{pri}+G_{sec}$) are shown figure 3.18. As the difference between primary and steady-state becomes smaller for higher mode II G_{sec} slopes downwards. As G_{sec} is superposed over G_{pri} , the resulting $G_{pri}+G_{sec}$ is different from the direct optimisation of G_{SS} in figure 3.16.

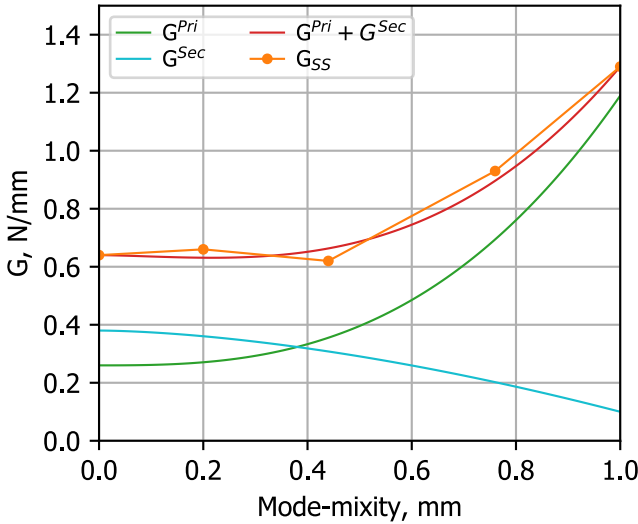


Figure 3.18: Superposed ($G_{Pri}+G_{Sec}$) Benzeggagh-Kenane fit for primary (G_{Pri}) and secondary (G_{Sec}) toughness to approximate the mixed-mode steady-state (G_{SS}) results.

3.4.2 THE SECONDARY MODE I INTERFACE STRENGTH

The strength for the secondary bilinear law needs to be determined. For the primary law the strength is an experimentally determined value by a transverse tensile strength test on a unidirectional coupon, which is a pure matrix-loaded test. The interface strength defines the point of initiation, but indirectly it defines the fracture processing zone length of the cohesive zone model[59, 101, 107]. This attribute is exploited for the secondary law. Through a sensitivity study on the interface strength in a numerical model, the process zone length to go from initiation to steady-state can be fitted to match the experiments.

A model of a DCB coupon was used to study the sensitivity of the mode I interface strength. The model was developed according to the framework described in section 2.3. For illustration, the out-of-plane displacement and interface damage at an applied displacement of 10 mm is shown in figure 3.19 for a DCB coupon with a secondary interface strength of 0.7 MPa.

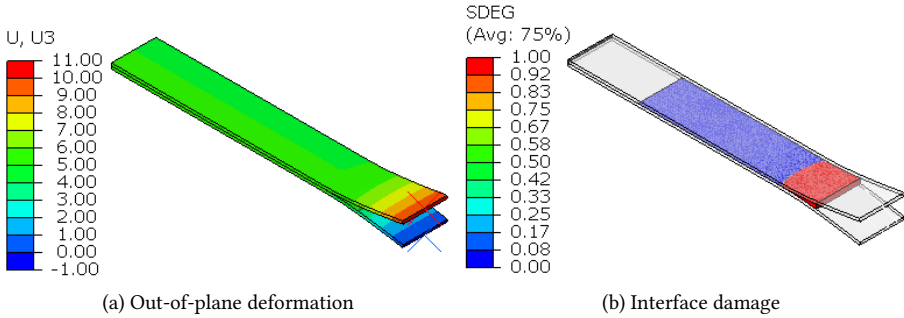


Figure 3.19: Example of the response of a DCB model at 10 mm applied displacement with a secondary interface strength of 0.7 MPa.

An interface strength of 0.35 MPa - 3.0 MPa was investigated. From these models, the force-displacement curves are extracted as well as the delamination length. Using equation (3.4) the R-curve response experienced by the DCB models is retrieved. The results of the different interface strengths for a fixed G_{IC}^0 of 0.26 N/mm and G_{IC}^{SS} of 0.65 N/mm are given in figure 3.20.

The initiation and steady-state are not affected by the interface strength, and both follow nicely the experimental results (in grey). While the transition is affected. In figure 3.20a the peak force is reduced, giving a lower strength, and in figure 3.20b the processing zone length is increased.

The fracture processing zone length can also be visualised within the model itself. The number of active cohesive elements in the secondary cohesive element set should match the processing zone length of 12.1 mm, as presented in table 3.1. The top view of the secondary interface, highlighting the coloured processing zone, is given in figure 3.21 for the four models. Considering both plots of figure 3.20 and the length calculated in figure 3.21, an interface strength of 0.7 MPa is deemed to be the best.

3.4.3 THE SECONDARY MODE I PENALTY STIFFNESS

The penalty stiffness can be calculated from the primary and secondary interface strengths and the CSERR. The goal is to have the point of initiation of the secondary law be at the same displacement as the point of full failure for the primary law. A bilinear law forms a triangle from which the endpoint of the primary law can be calculated based on trigonometry using:

$$G_C = 0.5\sigma_c d_{end} \quad (3.24)$$

Rewriting it makes it possible to obtain the displacement for full failure[108]:

$$d_{end}^{Pri} = \frac{2G_C^{Pri}}{\sigma_c^{Pri}} \quad (3.25)$$

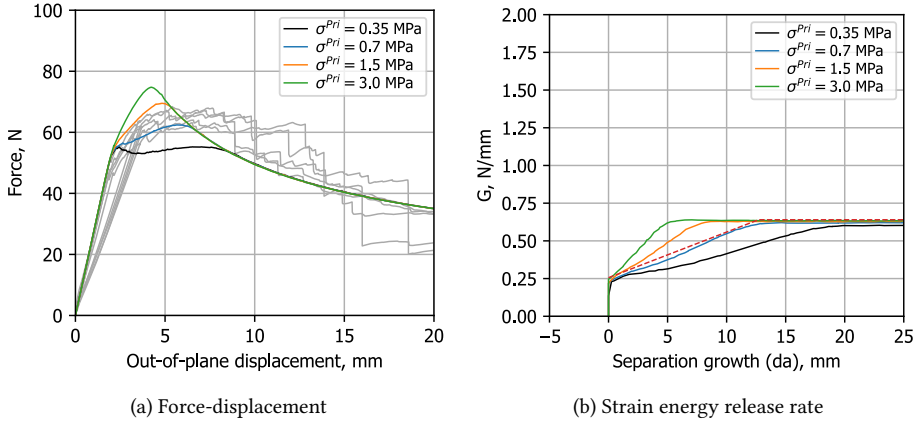


Figure 3.20: Change of the peak force and processing zone length due to the change of the Mode I interface strength in the DCB models.

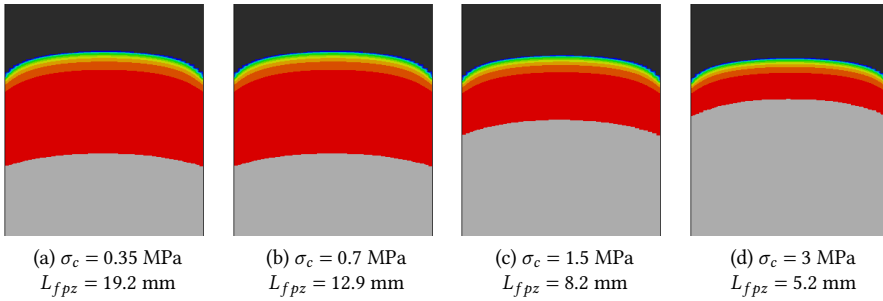


Figure 3.21: Fracture processing zone length in the DCB FE models of the secondary set of cohesive elements for different interface strengths.

The initiation point of the secondary law can be calculated as follows:

$$d_0^{Sec} = \frac{\sigma_c^{Sec}}{K^{Sec}} \tag{3.26}$$

With the requirement that $d_0^{Sec} = d_{end}^{Pri}$ the stiffness can be calculated by:

$$K^{Sec} = \sigma_c^{Sec} \frac{\sigma_c^{Pri}}{2G_C^{Pri}} \tag{3.27}$$

3.4.4 THE SECONDARY MODE II INTERFACE STRENGTH AND STIFFNESS

The fracture processing zone for mode II is unknown and therefore difficult to use to estimate the mode II interface strength and consequently the penalty stiffness. In addition to the matching of the primary end and the secondary initiation, the requirement of

thermodynamical consistency is added[109, 110]. This requirement was already present for a normal bilinear law for the primary cohesive elements but has so far not been included for the secondary law. This consistency means that during a change in mixed-mode conditions, no energy is being retrieved. This is especially important in the secondary law as it deals with large processing zones and thence change in mixed-mode conditions. This requirement is discussed in section 5.3 and the equation is repeated in equation (3.28)

$$K_{sh} = K_I \frac{G_{IC}}{G_{IIC}} \left(\frac{\tau_c}{\sigma_c} \right)^2 \quad (3.28)$$

First write equation (3.27) in terms of the secondary shear stiffness:

$$K_{Sh}^{Sec} = \tau_c^{Sec} \frac{\tau_c^{Pri}}{2G_{IIC}^{Pri}} \quad (3.29)$$

which can now be related to equation (3.28), from which the following is obtained:

$$K_I^{Sec} \frac{G_{IC}^{Sec}}{G_{IIC}^{Sec}} \left(\frac{\tau_c^{Sec}}{\sigma_c^{Sec}} \right)^2 = \tau_c^{Sec} \frac{\tau_c^{Pri}}{2G_{IIC}^{Pri}} \quad (3.30)$$

The terms can be reordered to solve for τ_c^{Sec}

$$\tau_c^{Sec} = \frac{(\sigma_c^{Sec})^2}{K_I^{Sec}} \frac{\tau_c^{Pri}}{2G_{IIC}^{Pri}} \frac{G_{IIC}^{Sec}}{G_{IC}^{Sec}} \quad (3.31)$$

By substituting again equation (3.27) for K_I^{Sec} the final solution is obtained:

$$\tau_c^{Sec} = \tau_c^{Pri} \frac{\sigma_c^{Sec}}{\sigma_c^{Pri}} \frac{G_{IIC}^{Sec}}{G_{IIC}^{Pri}} \frac{G_{IC}^{Pri}}{G_{IC}^{Sec}} \quad (3.32)$$

By rewriting it can be seen that ratios for the strength and toughness of the primary law need to be equal to the secondary law:

$$\frac{G_{IIC}^{Pri}}{G_{IC}^{Pri}} \frac{\sigma_c^{Pri}}{\tau_c^{Pri}} = \frac{G_{IIC}^{Sec}}{G_{IC}^{Sec}} \frac{\sigma_c^{Sec}}{\tau_c^{Sec}} \quad (3.33)$$

Equation (3.29) can now be solved for the secondary shear stiffness as well.

3.5 FINAL PROPERTIES

Two sets of properties, initiation and steady-state have been derived in this chapter in addition to the results already available from Clay et al.[102]. The properties from the unidirectional interface will be used for the base models of the multi-stringer and single-stringer specimens in future chapters, which will provide a lower-limit prediction of separation. For the numerical-experimental comparison, the steady-state is used as an upper bound.

Three sets of superposed properties are proposed. The first uses the properties of the unidirectional tests from literature and the steady-state from this characterization. The second set uses the initiation and steady-state from this characterization study. The

difference for mode I is only small, but the split between the initiation and propagation values for mode II is greater. Lastly, a trilinear law with no increase in mode II is assumed to study the mixed-mode behaviour in the single-stringer models.

Table 3.2: List of the final cohesive interface properties to be used throughout this thesis.

Name	Symbol	G_I	σ_c	K_I	G_{II}	τ_c	K_{sh}	η_{BK}
Base UD (Clay [102])	G_{clay}	0.256	78.9	4.76E5	0.65	99.4	-	2.07
Initiation (0)	G_0	0.26	99.4	4.76E5	1.19	99.4	4.11E5	2.77
Steady-state (SS)	G_{SS}	0.64	78.9	4.76E5	1.29	99.4	-	3.33
Trilaw $G_{clay} - G_{SS}$	G_{clay}	0.256	78.9	4.76E5	0.65	99.4	8.98E3	2.07
	G_{SS}	0.384	0.7	108	0.64	0.6	44	5.67
Trilaw $G_0 - G_{SS}$	G_0	0.26	78.9	4.76E5	1.19	99.4	1.65E5	2.77
	G_{SS}	0.38	0.7	106	0.1	0.05	2.11	1.64
Trilaw $G_{clay} - G_{II0}$	G_{clay}	0.256	78.9	4.76E5	0.65	99.4	8.98E3	2.07
	G_{II0}	0.38	0.7	106	0.1	33.0	5.55E3	1.65

3.6 DISCUSSION

This discussion includes mainly the implementation of the properties in the MMB models and the corresponding discussion on the validity of the properties, the data reduction method and the test itself.

3.6.1 MIXED-MODE IMPLEMENTATION OF THE TRILINEAR LAW.

The interface properties are implemented in the mixed-mode bending models, developed through section 2.3. An example of the response in FE is given in figure 3.22.

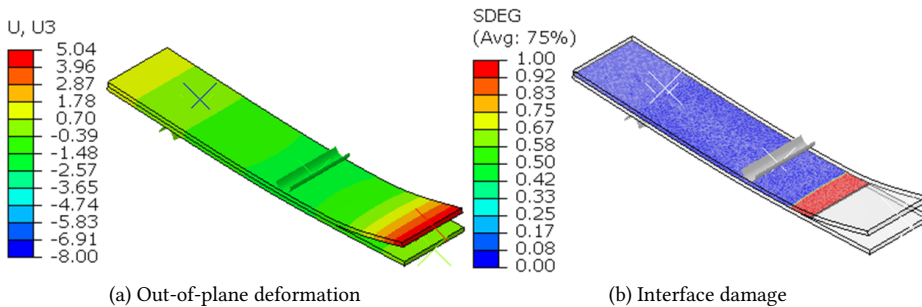


Figure 3.22: Example of the response of an MMB model at 8 mm applied displacement.

The mixed-mode conditions of the tests are considered for the calculation of the lever length in the numerical model: 20%, 44% and 76%. The force-displacement responses are

not compared to the tests as in the numerical model the mass of the lever is not considered. The force-displacement response and strain energy release rates are shown in figure 3.23.

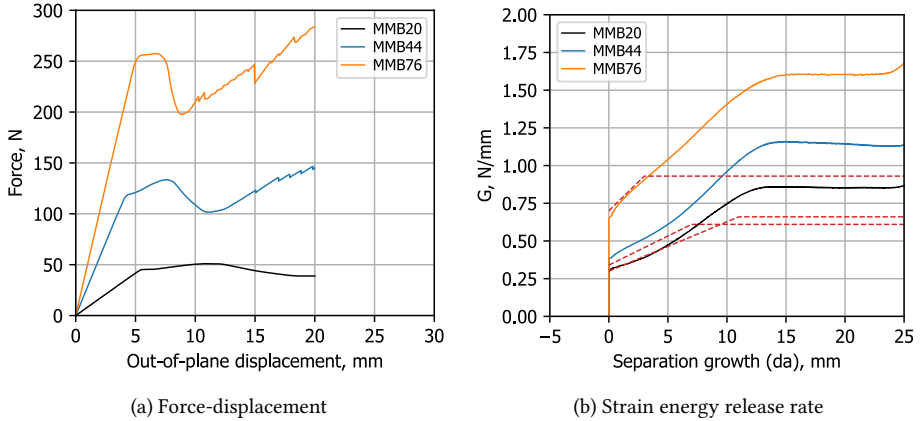


Figure 3.23: Numerical results of MMB for different mixed-mode conditions with R-curve properties.

The initiation and slope of the CSERR are captured by the models as can be seen in figure 3.23b. However, all three models fail to reproduce the steady-state part of the R-curve that was observed during the tests. In order to understand the shortcomings of the MMB models with a superposed trilinear law, a closer look is taken at changing the secondary mode II interface strength and secondly at different interface toughnesses. The 44% mixed-mode bending tests were selected as the load case to verify the correct implementation of the properties.

3.6.2 MODE II SECONDARY INTERFACE STRENGTH EFFECT ON MIXED-MODE TRILINEAR LAW.

The effect of the secondary interface strength on the force-displacement and strain energy release rate responses are shown in figure 3.24. The basic model with interface strength of 0.05 MPa, as a result of equation (3.32), severely overpredicts its own input. The low interface strength results in a long processing zone, which has an effect on the instantaneous mixed-mode conditions [107, 111, 112].

The outcome is that in order to reproduce the same R-curve-like effects as the test the secondary interface strength needs to be increased to 180 MPa. This actually leads to the displacement at the initiation of the cohesive element being higher than the displacement at full failure. It is simply assumed that all its energy will be released upon reaching the maximum strength. In order to implement this higher strength, the earlier imposed requirement of thermodynamical consistency is ignored. The requirement of having the initiation of the secondary mode match the final failure of the primary mode is still retained.

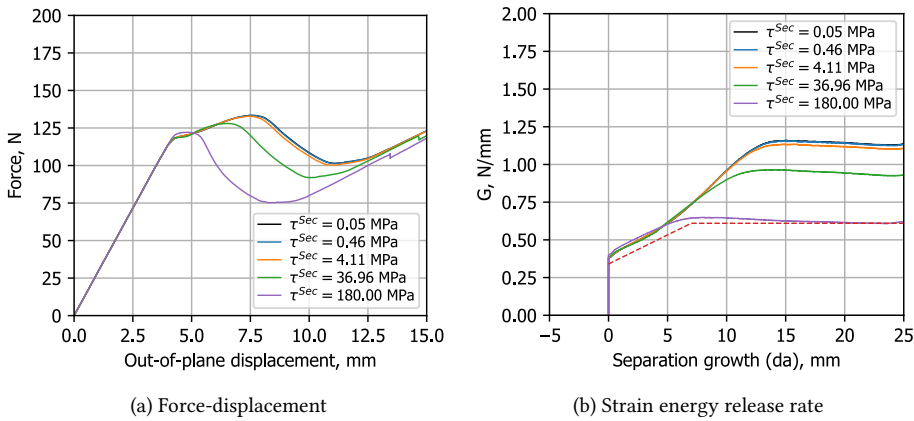


Figure 3.24: Shortening of the fracture processing zone due to increase of the secondary Mode II strength in an 44% MMB FE model.

3.6.3 MODE II INTERFACE TOUGHNESS EFFECT ON MIXED-MODE TRI-LINEAR LAW.

The interface properties proposed in table 3.2 are implemented in the MMB 44\$ model. The results of these models are shown in figure 3.25. All three bilinear law models reproduce the interface toughness measurements. The fact that GSS is overshooting the steady-state is a result of the optimized fit to obtain the BK law. Although the measured steady-state was around 0.61 N/mm, the implemented steady-state BK is closer to 0.7, as could be seen in figure 3.16. All trilinear models completely overshoot the steady-state. Most interestingly, setting mode II to have no increase in fracture toughness also has no effect on the outcome.

3.6.4 DISCUSSION ON THE VALIDITY OF THE CONSTANT MIXED-MODE ASSUMPTION

The changing mode-mixity can be seen from the output of a primary and secondary cohesive element at the same location. The total mixed-mode CSERR at the centroid of both elements plotted against its damage variable SDEG is presented in figure 3.26. Generally, the primary element starts around pure mode II, and the total mixed-mode condition slowly falls during damage evolution until it reaches the desired 0.44. Note that the instantaneous mode-mixity is likely to be lower than 0.44 to compensate for the initial energy released under mode II. The secondary cohesive element initiate and fails under pure mode I. This is why there was no effect in the outcome of the MMB50 models when it is assumed there is no increase in mode II fracture toughness (G_{II0}) in figure 3.25.

The changing mixed-mode conditions can be visualised from the deformation of laminates adjacent to the interface. The side view of a mixed-mode bending coupon, showing the cohesive interface in red, is presented in figure 3.27. The nodes at either side of the interface have a vertical and horizontal displacement with respect to the other side. The

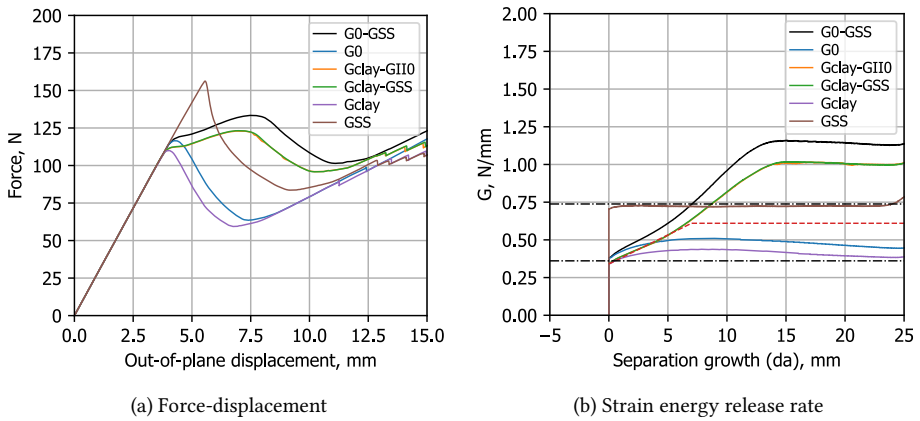


Figure 3.25: Illustration of all properties of table 3.1 in the 44% MMB FE model. There is no change when removing the mode II R-curve effect (GII0)

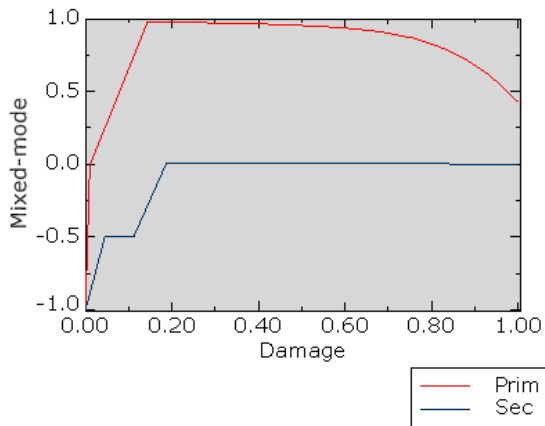


Figure 3.26: Change of mode-mixity during damage evolution in a cohesive element.

higher the ratio of the vertical opening to the horizontal, the more mode I is present. Larger processing zones lead to a higher mode I opening due to the mismatch in the curvatures of the two arms [111].

In summary, the increase of fracture toughness due to the failure mechanisms in the wake of the crack is assumed to happen in the fixed 44% mixed-mode state. However, the energy is being released locally under (pure) mode I. The MMB data reduction method does not account for this. Hence it is not suitable for the characterisation of R-curve effects.

The effect of not knowing the toughening properties under a fixed mixed-mode condition is minimal if the structure itself does not experience it. Hence, for the continuation of this work, it is assumed that all energy in the MMB has been released under the three

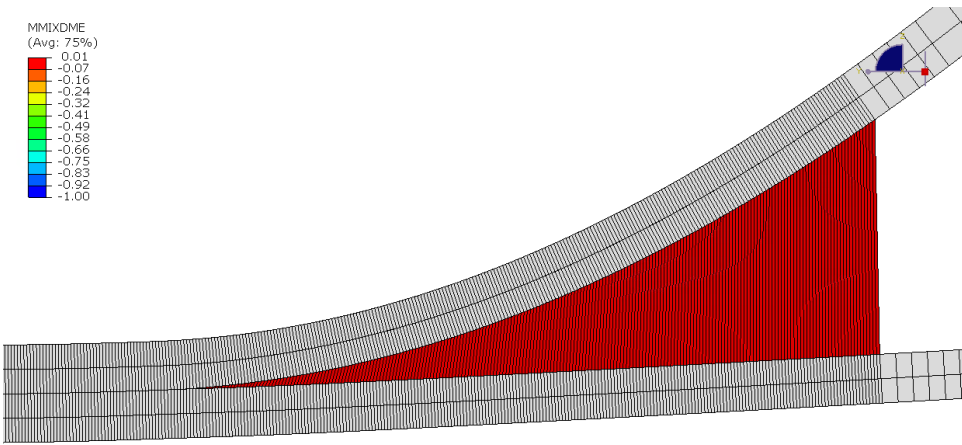


Figure 3.27: Interface deformation of a MMB 50% with a scale factor of 3. The ratio of vertical to horizontal displacement is larger on the right and smaller closer to the crack front on the left.

fixed mixed-mode conditions. What might still have an effect that is ignored is that the toughening mechanisms for mode I are different if the history of the crack opening is under a certain mixed-mode. For example, in figure 3.21, fibres are bridging between a +45// -45 interface, whereas in figure 3.14, there are fewer fibres bridging, but there is delamination migration.

3.7 CONCLUSION

Coupon tests are used to characterise the interface fracture toughness for a cross-ply interface. The layout of the bottom sublaminates is the same as the skin for all other specimens considered within this thesis, and the top sublaminates are their anti-symmetric counterparts. DCB, MMB (20%, 50% and 80%) and ENF tests were performed to get the full range of interface properties. This made it possible to calculate the dependency of the interface toughness on the mode-mixity following the Benzeggagh-Kenane relationship.

Cross-ply interface toughening effects occurring at the interface cause the CSERR to increase when the delamination length increases. This R-curve effect is also identified by fitting a bilinear optimisation curve through the data set of each coupon test. With these results, initiation and steady-state interface toughness as well as the fracture processing zone length were obtained. For higher mode-mixity, the initiation values increased, and the fracture processing zone length and the increase of fracture toughness both decreased. Both the fibre bridging decreased and the delamination migration increased for increasing mixed-mode.

The R-curve effect was implemented within the finite element models through an approach where two bilinear cohesive laws are superposed to obtain a trilinear law behaviour. The work of Dávila was used as the basis and adapted. With the updated approach, the initiation of the second law occurs exactly when the first element has fully failed. This decouples the two cohesive elements; the two superposed elements will not release energy simultaneously. Furthermore, the requirement of thermodynamic consistency between

normal and shearing modes is also applied to the second law. This allows calculating the mode II interface strength without knowing the fracture processing zone length.

The interface properties were applied to a DCB and MMB 44% model, and the same experimental data reduction scheme was applied to the numerical models. This showed that the R-curve effect is well captured for the DCB model. The opposite is true for the MMB 44% model, but the results are used regardless as it has been shown that reducing the increase of fracture toughness of mode II had no effect on the outcome of the models.

This chapter presented a table of all the considered sets of cohesive interface properties, two bilinear law and three superposed trilinear law sets of properties. The effect of the interface properties on postbuckling separation will be the topic of the other chapters.

4

A SEMI-ANALYTICAL APPROACH TO IDENTIFY INITIATION OF BENDING SEPARATION

4

The typical bending of the skin in postbuckling can locally be addressed as a two-dimensional problem. Due to this two-dimensionality, a simple criterion that predicts the initiation location can be designed. The approach is semi-analytical, working in conjunction with a finite element model of a stiffened panel. Unlike models employing cohesive elements to capture initiation, the computational time is short whilst attaining acceptable accuracy. Verification is done through a representative 2D skin-flange bending model, where analytical failure is compared to failure using cohesive elements. The assumption of a small precrack is similar to a state of cohesive elements with low interface strengths. The analytical framework is also applied to a finite element model of postbuckled four-stringer composite panels. The model is validated through cohesive elements in the four-stringer panel with an error within 10%. This procedure can potentially reduce the overall development cost and allows the investigation of the design parameters that influence the skin-stringer separation.

4.1 INTRODUCTION

This chapter presents a semi-analytical approach to investigate the initiation of skin-stringer separation. Commonly these types of criteria are either fully numerical or analytical. Within a purely analytical framework, there are limits to the complexity of the structure, such as boundary conditions and imperfections. Whereas in FE, the primary method to capture initiation, cohesive zone modelling, is time-consuming for large structures.

This failure criterion works in conjunction with a finite element model to predict the initiation. This offers significant computational advantages as well as versatility and usability. This approach uses the moment output from a finite element analysis to identify the locations of maximum bending and maximum twisting. Subsequently, a failure index is calculated to estimate the applied displacement where the stringer will start to separate from the skin due to the postbuckling deformations.

A simple model can be made of a composite structure using FE, where different geometries or stacking sequences can be considered. Furthermore, FE allows the consideration of initial geometrical imperfections by adding a scaled buckling eigenvalue mode or actual panel measurements. Different buckling cases could be investigated for the same geometry and the possible change in buckling patterns at high postbuckling ratios

After the derivation, implementation and verification of the semi-analytical criterion, it is applied to the four-stringer panel designs discussed in section 2.6. This makes it possible to efficiently determine the critical postbuckling shape, which corresponds to step 1 in the building block pyramid in figure 2.1. This chapter is split into separate sections:

Chapter goals

- **section 4.2:** To derive a semi-analytical equation for the determination of the initiation of skin-stringer separation.
- **section 4.3:** To illustrate the finite element implementation and verify the criterion by comparing semi-analytical to cohesive initiation.
- **section 4.4:** To determine the initiation in two four-stringer panel designs using the criterion and verify the outcome of the panel once more to a cohesive model.

4.2 THE SEMI-ANALYTICAL APPROACH

The derivation of the initiation criterion for bending is based on the fracture mechanics-based approach initially developed by Williams [25, 113] to estimate the propagation of an initial crack in laminated composites.

A coupon specimen with an initial pre-crack in a double cantilever beam is used, as shown in 4.1a. The nomenclature designates the top laminate as the flange (f) and the bottom laminate as the skin (s), and where these two are connected, the skin-flange overlap as (sf). A moment (M) is applied to the skin, the flange, and the skin-flange overlap and subsequently, the parts undergo a rotation (ϕ).

Although the skin-flange overlap is intact, the skin and flange part of the intact overlap are considered separately. This can be done as in the finite element model, the skin and flange are modelled as separate elements. This makes it possible to consider the slope of

the overlap to be bilinear instead of linear, deviating from William's work [25]. The two connected parts consist of the skin laminate (sf1) and the stringer laminate (sf2).

After a small crack extension, the previous crack front is split into the unconnected skin and flange laminates, as can be seen in 4.1b. For a small crack extension, it is assumed that the moments in sections s and f do not change. Hence, the initial moments of the skin and flange now also act on the two unconnected sections at the initial crack front.

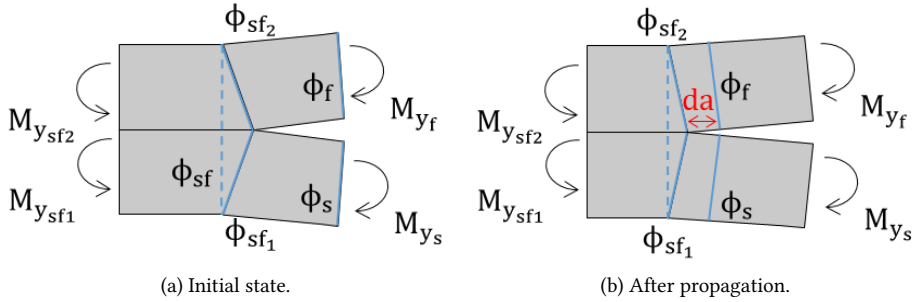


Figure 4.1: Skin-flange cross-section with individual bending moments and section rotation.

Due to the small crack extension da , the strain energy (U) and the external energy (V) change and the difference between the two states give the strain energy release rate (G):

$$G = \left(\frac{dV}{da} - \frac{dU}{da} \right) \quad (4.1)$$

The crack extends by a length of da if the strain energy release rate approaches the critical strain energy release rate (G_c) value. The curvature (κ) in the direction of crack extension is equal to the variation in the slope over the distance dy , therefore:

$$\frac{d\phi}{dy} = \kappa_y = M_y d_{22} = \frac{d\phi}{da} \quad (4.2)$$

where d_{22} is the bending compliance of a composite laminate. The variation in the external energy can be defined as the change in the curvature and applied moment due to the crack extension. The external energy applied to the crack front prior to a crack extension is given by:

$$\frac{dV}{da} = \left(M_{y_s} \frac{d\phi_s}{da} + M_{y_f} \frac{d\phi_f}{da} \right) - \left(M_{y_{sf1}} \frac{d\phi_{sf1}}{da} + M_{y_{sf2}} \frac{d\phi_{sf2}}{da} \right) \quad (4.3)$$

Substituting equation (4.2) and considering that sf1 and s have the same bending compliance and sf2 and f also have the same bending compliance, the following expression is obtained:

$$dV/da = \left(M_{y_s}^2 - M_{y_{sf1}}^2 \right) d_{22_s} + \left(M_{y_f}^2 - M_{y_{sf2}}^2 \right) d_{22_f} \quad (4.4)$$

The strain energy of a plate subjected to bending moments is given by:

$$U = \frac{1}{2} M_y^2 d_{22} \quad (4.5)$$

Considering the sections at the crack front of figure 4.1a, the following equation is obtained:

$$U = \frac{1}{2} \left(M_{y_{sf1}}^2 d_{22_s} + M_{y_{sf2}}^2 d_{22_f} \right) \quad (4.6)$$

After a crack extension, as represented in figure 4.1b, the strain energy is given by:

$$U = \frac{1}{2} \left(M_{y_s}^2 d_{22_s} + M_{y_s}^2 d_{22_f} \right) \quad (4.7)$$

Therefore the variation of the strain energy due to the crack extension da is:

$$\frac{dU}{da} = \frac{1}{2} \left(M_{y_{sf1}}^2 d_{22_s} + M_{y_{sf2}}^2 d_{22_f} \right) - \frac{1}{2} \left(M_{y_s}^2 d_{22_s} + M_{y_s}^2 d_{22_f} \right) \quad (4.8)$$

$$\frac{dU}{da} = \frac{1}{2} \left(M_{y_s}^2 - M_{y_{sf1}}^2 \right) d_{22_s} + \frac{1}{2} \left(M_{y_f}^2 - M_{y_{sf2}}^2 \right) d_{22_f} \quad (4.9)$$

The variation in the strain energy (equation (4.9)) is half of the variation in the external energy (equation (4.4)), hence the strain energy release rate of equation (4.1) can be written as:

$$G = \frac{1}{2} \left(M_{y_s}^2 - M_{y_{sf1}}^2 \right) d_{22_s} + \left(M_{y_f}^2 - M_{y_{sf2}}^2 \right) d_{22_f} \quad (4.10)$$

Until this point, the derivation followed William's work [25], except for splitting the skin-flange overlap in the two sections. In the case of initiation of skin-stringer separation in a stiffened panel, a free edge needs to be considered. The updated skin-flange cross-section is illustrated in figure 4.2.

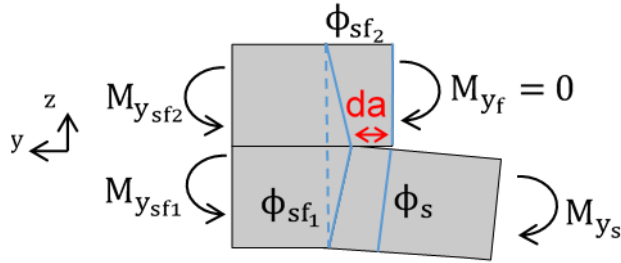


Figure 4.2: Skin-flange cross-section with flange termination.

Before a crack extension, the moment in the top section of the skin-flange laminate, $sf2$, is only attributed to the transfer of the loads from the skin through the skin-stringer interface. This is because there is a free edge and thus M_{y_f} is zero. After a crack extension, the moment $M_{y_{sf2}}$ becomes zero as well. Therefore, in this case equation (4.10) becomes:

$$G = \frac{1}{2} \left(M_{y_s}^2 d_{22_s} \right) - \left(M_{y_{sf2}}^2 d_{22_f} + M_{y_{sf1}}^2 d_{22_s} \right) \quad (4.11)$$

The failure index (FI) for skin-stringer separation initiation can be calculated by comparing the strain energy release rate to the critical strain energy release rate. Although any stiffness mismatch between skin and flange laminates will couple opening and shear crack tractions, it is assumed that, in the loading case of figure 4.2, the critical strain energy release rate is dominated by mode I. Consequently, the failure index is expressed in terms of the mode I critical energy G_{Ic} as:

$$FI = \frac{1}{2G_{Ic}} \left(M_{y_s}^2 d_{22_s} - \left(M_{y_{sf2}}^2 d_{22_f} + M_{y_{sf1}}^2 d_{22_s} \right) \right) \quad (4.12)$$

The failure index is set to zero if the bending moment is negative in the skin-only section.

4.3 IMPLEMENTATION AND VERIFICATION OF THE SEMI-ANALYTICAL CRITERION

A representative skin-flange model is developed to show the implementation of the criterion within FE. Furthermore, the model is used for the mesh sensitivity study and verification through a cohesive comparison.

4.3.1 REPRESENTATIVE VERIFICATION MODEL

For the illustration of the implementation process and for the verification of the criterion a simple skin-flange bending model is developed. The model is representative of the skin-flange section of a multi-stringer panel, specifically the red highlighted section in figure 4.3.

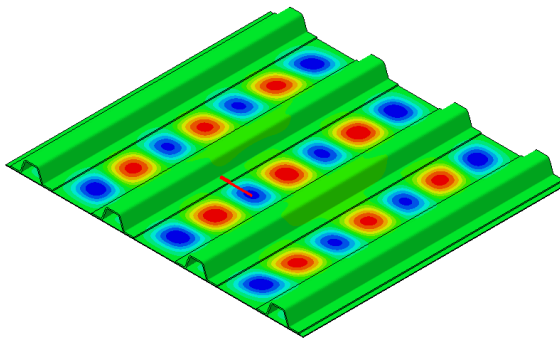


Figure 4.3: Section of a stiffened panel for which the criterion implementation/verification model is representative.

The verification model is shown in figure 4.4 including dimensions. A load orthogonal to the skin is applied to create a bending moment locally at the skin-flange interface similar to the conditions in a postbuckled panel. A distance of 100 mm was chosen between

the applied displacement (dz) and the flange termination to limit the vertical shear load. All nodes are constrained to only deform in the yz -plane. This effectively creates the 2-dimensional loading and deformation conditions on which this criterion is based, whilst being consistent with the use of SC8R elements. The left side of the model is fully clamped.

The dimension in the x -direction is always 1 mm with only a single element in that direction. Also in the z -direction, only a single element is used per sublaminates, but its thickness depends on the layup. The mesh size in the y -direction is variable. A mesh size of 1 mm and a stringer twice the thickness of the skin is used as the reference model, which can be found in figure 4.4.

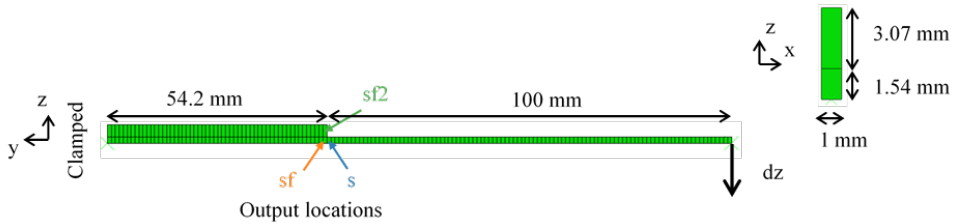


Figure 4.4: Numerical skin-flange bending model for criterion verification.

The applied displacement (dz) versus the force is given in figure 4.5 and the corresponding out-of-plane displacement ($U3$) plot at 20 mm displacement in figure 4.6. The results are mainly presented to give an indication of the type of loading and to be able to recreate and validate the results.

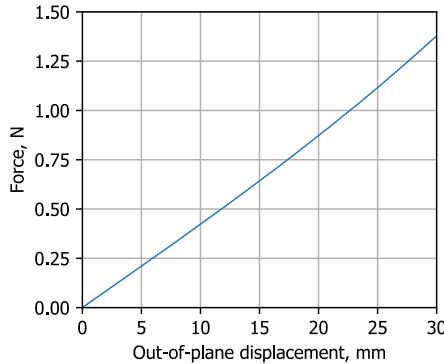


Figure 4.5: Force-displacement response of the baseline skin-flange model.

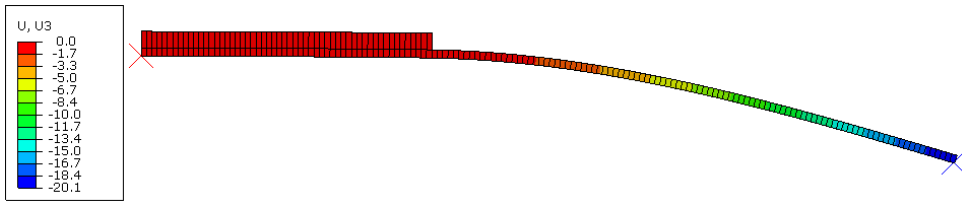


Figure 4.6: Deformation of the baseline skin-flange model.

4.3.2 FINITE ELEMENT IMPLEMENTATION

Within the FE model, three sets of elements are defined, for the skin (s), the skin part of the skin-flange (sf1) and the flange part (sf2). The three output locations are highlighted in figure 4.4. For the verification model, this is a single element per set, but for the single/multi-stringer panels it includes all the elements along the length/x-axis at this cross-sectional location. The sets are defined as follows in the input file:

```
*ELSET, ELSET = FI_S
      nID1, nIDx
*ELSET, ELSET = FI_SF1
      nID2, nIDx
*ELSET, ELSET = FI_SF2
      nID3, nIDx
```

The section curvatures or moments and forces can be requested, next to the standard strains/stresses:

```
*Element Output, directions=YES
EE, S, Sk, Sm, Sf
```

At the end of the analysis a python for Abaqus script is called that writes a comma-separated values (csv) file for all output frames and for each of the sets through a for loop. Using the abaqus function LeafFromElementSets, only the elements within that set are written to the csv file using writeFieldReport.

```
session.fieldReportOptions.setValues(
reportFormat=COMMA_SEPARATED_VALUES)

for loc in ['S', 'SF1', 'SF2']:
    leaf = dgo.LeafFromElementSets(elementSets=(Part+
        '.FI_'+loc, ))

    myViewport.odbDisplay.displayGroup.replace(leaf=leaf)
    session.writeFieldReport(fileName='{}_{}_SK_{}_{}.csv'
        .format(Path, ViewportName, loc, Frame), append=OFF,
        sortItem='Element Label', odb=odb, step=i, frame=j,
        outputPosition=INTEGRATION_POINT, variable=
        (('SK', INTEGRATION_POINT), ), stepFrame=SPECIFY)
```

The csv file includes the following columns:

- ODB Name
- Step
- Frame
- Part Instance Name
- Element Label
- IntPt
- X
- Y
- Z
- Section Name
- Material Name
- Section Point
- SK-SK2
- SK-SK1
- SK-SK3

Through standard Python this can be imported as a Pandas (pd) dataframe.

```
Df_SK = pd.read_csv(filename.csv', usecols =
[' Element Label', 'X', 'Y', 'Z', 'Section Name',
'Material Name', 'SK-SK1',
' SK-SK2', ' SK-SK3']
).sort_values(['X'])
```

The added benefit of the csv file is that next to the standard field output (element label and element output) it also includes the xyz coordinates of the element centroid as well as the section and material name. The coordinates can be used to sort all the elements in the x-direction. The section and material name can be coupled to the initial input file. Reading the input file the material properties can be connected to the composite layup continuum shell section to calculate the bending stiffness (ABD Matrix). In the end for each element group, (s, sf1 and sf2) the x-location the bending stiffness and the section curvature/moment is known.

Defining a lambda function in Python to calculate the component $M_y^2 d_{22} = k_y^2 D_{22}$ allows to easily calculate the Failure Index using equation (4.12):

```
valsq = lambda loc, out, j: Df_SK[loc][out].values**2
*ABD[loc][j,j]
```

```
CSERR = 0.5*abs(-valsq('S', 'SK2', 4)+valsq('SF1', 'SK2', 4)+
valsq('SF2', 'SK2', 4))
```

```
CSERR[Df_SK['S']['SK2']<0]=0
```

```
FI_B = CSERR/Gc['I']
```

4.3.3 MESH SENSITIVITY OF THE SEMI-ANALYTICAL CRITERION

The sensitivity of the semi-analytical criterion to the mesh size is studied on the model depicted in figure 4.4. The element size of the skin and skin-flange overlap are first varied simultaneously, between 0.1 and 2.0 mm. Next, the skin element size is varied while keeping the overlap at 0.3 mm. Hereafter the skin size is fixed at 0.3 mm and the overlap is changed. Additionally, the skin and overlap are fixed at 2.0 mm and only the first element of the overlap, at which the output $sf1/sf2$ is requested, is decreased.

Examples of the different meshing strategies are shown in figure 4.8. These models show the bending moment (SM2) to see how that is affected locally by the choice of the mesh size. The magnitude of the bending moment in the skin is unaffected by the mesh size, comparing figure 4.8a to figure 4.8b. Hence in figure 4.7 the criterion seems to be independent of the skin mesh size. Oppositely, a smaller mesh size for the stringer flange, as shown in figure 4.8c, does lead to a higher local bending moment in Sf2. These are attributed to the singularities present at a stringer flange edge[114]. This sensitivity is also seen in figure 4.7, when looking at the curve "flange, skin = 0.3 mm". The refinement is however only required in the first (rightmost) element of the skin-flange overlap, illustrated in figure 4.8d.

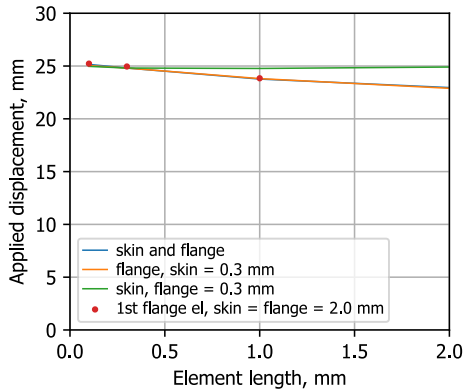
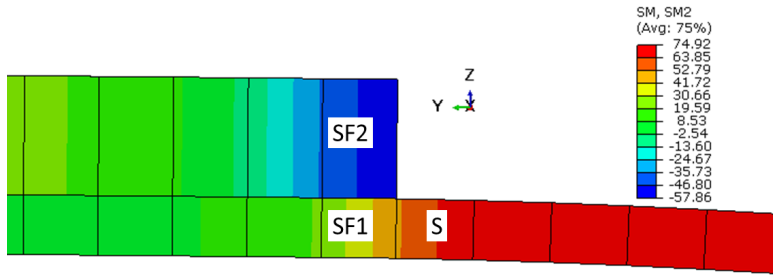
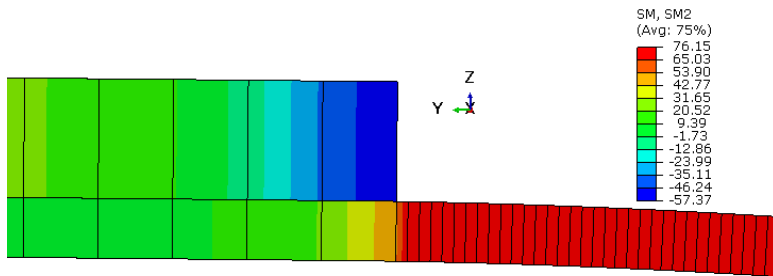


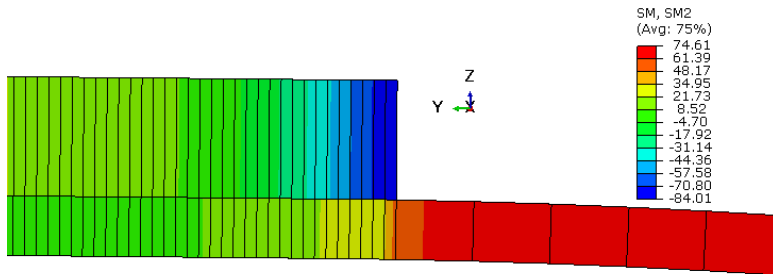
Figure 4.7: Mesh sensitivity of the semi-analytical criterion. Changing only the flange mesh size, only the skin mesh size, and changing both simultaneously.



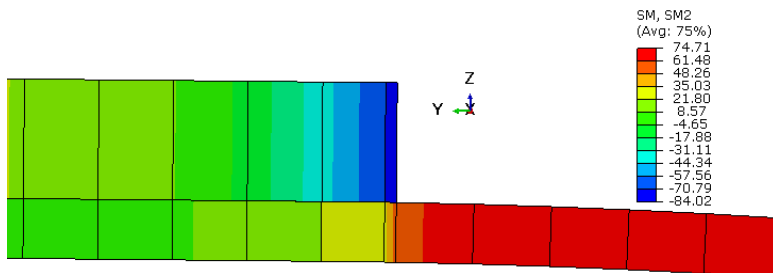
(a) skin = flange = 2.0 mm



(b) skin = 0.3 mm, flange = 2.0 mm



(c) skin = 2.0 mm, flange = 0.3 mm



(d) skin = flange = 2.0 mm, flange edge (SF1/SF2) = 0.3 mm

Figure 4.8: Mesh view of verification models, showing bending moment at a displacement of 18 mm.

4.3.4 VERIFICATION OF THE CRITERION AGAINST COHESIVE INITIATION

The semi-analytical criterion can be verified using a similar model employing cohesive elements. The cohesive elements are zero-thickness with an element length of 0.3 mm along the y-axis and implemented following the method of section 2.3. The bilinear *G*_{clay} properties of table 3.2 are used for the cohesive material. However the mode I interface strength is varied: 10, 25, 50, 78.9, and 100 MPa and with that the shear penalty stiffness changes according to equation (3.28). The out-of-plane displacement and interface damage of the cohesive model with a strength of 78.9 MPa is shown in figure 4.9.

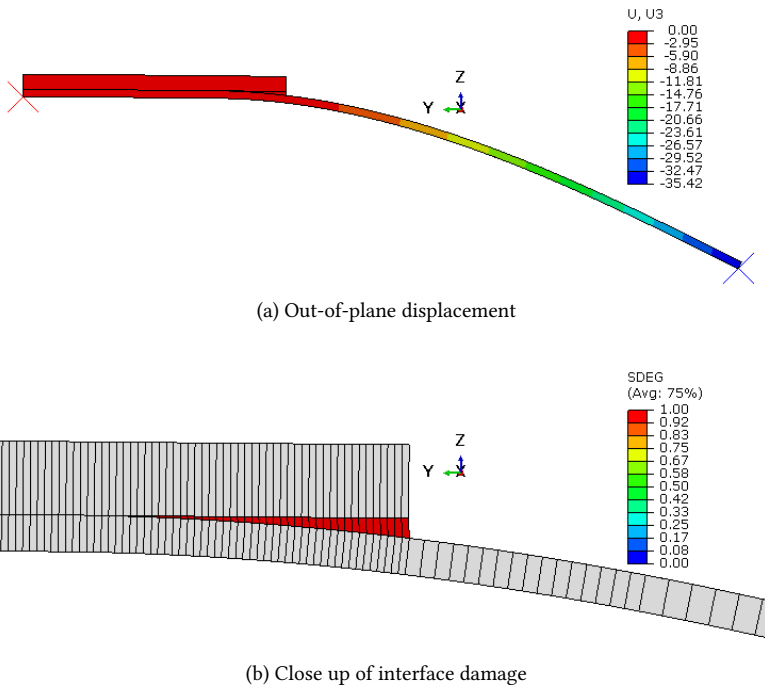


Figure 4.9: FE field output results of the cohesive model with an interface strength of 78.9 MPa.

The force-displacement response of the models with cohesive elements and the model with the criterion implemented is shown in figure 4.10. The initiation within the cohesive enriched models, defined by the location of the peak force, decreases with interface strength. At a low strength (<50 MPa), initiation stabilizes around the analytically found initiation point. The exact percentage difference is collected in table 4.1. This shows that if the strength is already exceeded, due to matrix cracking or other pre-damages, the criterion is able to predict the onset of that assumed pre-damage. If not, the criterion gives a conservative prediction of initiation[115].

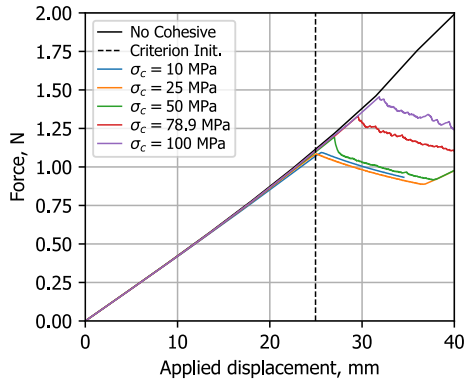


Figure 4.10: Force-displacement curves of the semi-analytical model and cohesive models with different interface strengths to illustrate initiation.

Table 4.1: Displacement at initiation for the semi-analytical model (Crit.) and cohesive models with different interface strengths.

Model	Crit.	10 MPa	25 MPa	50 MPa	78.9 MPa	100 MPa
d, mm	24.95	25.61(+3%)	25.07(+0%)	27.00(+8%)	29.56(+18%)	31.87(+28%)

4.4 INITIATION OF SEPARATION IN A FOUR-STRINGER PANEL

The semi-analytical criterion derived in section 4.2 can be used to determine the initiation in a multi-stringer panel design. In this section, the applied compressive displacement at which skin-stringer separation might occur in the four-stringer panel is determined using the criterion. The critical locations in the corresponding postbuckling shape can be obtained as well. The four-stringer panel models are also studied using cohesive elements to verify the outcome of the criterion.

The material properties and the laminate designs have been discussed in section 2.6.1 and section 2.6.2, respectively. As explained in section 2.6.2, two designs are considered: a panel with stringers that are the same thickness as the skin (thickness flange/skin=1) and a panel where the stringers are twice the thickness of the skin (thickness flange/skin=2). They will be simply referred to as the thin-stringer and thick-stringer panel, respectively. The thick-stringer panel and the thin-stringer panel will be discussed in section 4.4.1 and section 4.4.2, respectively. The specifics regarding the mesh and analysis can be found in section 2.3 and there are no initial imperfections applied to these models.

The four-stringer panel model without cohesive elements is presented in figure 4.11. The total amount of elements is $5e5$ and the amount of nodes is $2.5e5$. Three sets of elements are defined, the last skin element (s) and the first elements of the skin-flange overlap (sf1 and sf2). All elements at this cross-sectional location along the full length of the panel are included in the sets.

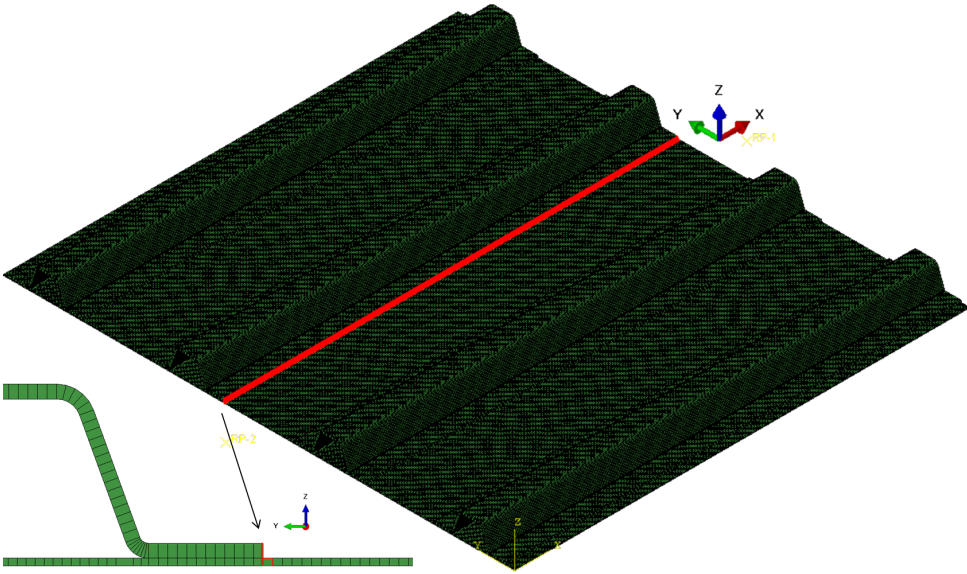


Figure 4.11: Four-stringer panel with a mesh size of 2 mm and local edge refinement of 0.3, with the three sections (s, sf1 and sf2) highlighted for the output used in the criterion.

A four-stringer panel model with a section that includes cohesive elements is created. The central part that is finely meshed is tied to its surroundings and includes cohesive elements at the interface. The model can be seen in figure 4.12 and contains 1.5E6 nodes and 1.3e6 elements.

First, the load-displacement curve and postbuckling shape of the simple model will be shown. Next, the failure indices from the criterion along the flange termination plus the corresponding bending moment M_y and twisting moment M_{xy} distribution will be compared. Next, the results are compared to the cohesive model.

4.4.1 THICK STRINGER PANEL: BENDING FAILURE

The force-displacement response and out-of-plane buckling deformation patterns at an applied compression displacement of approximately 2.6 mm are shown in figure 4.13. The panel postbuckling shape has seven half-waves with out-of-plane deformations below 4 mm.

The failure index is calculated in different sections along the edge of the flange and for an increasing applied compression displacement. The failure index distribution at intervals of 0.5 mm displacement is shown in figure 4.14. It is possible to determine the location and the value of the applied compression displacement in which the failure index is greater than one. The locations of the peaks correspond to the locations of maximum bending. The failure index in the panel with thick stringers exceeded 1 at a displacement of 2.6 mm.

4

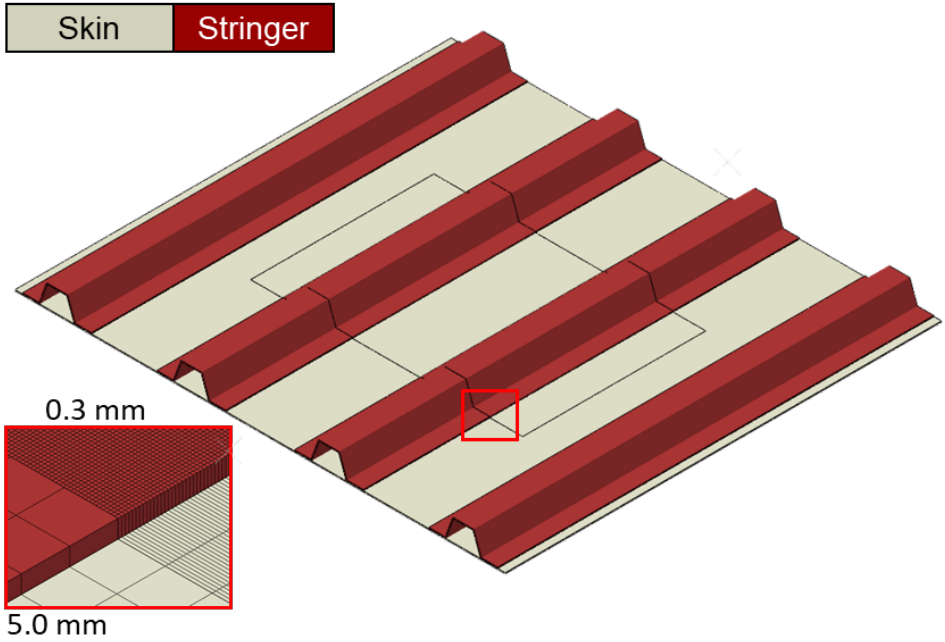


Figure 4.12: Four-stringer panel model with a refined center, encompassing the two middle stringer, at which cohesive elements are placed. This model can capture skin-stringer separation: initiation and propagation.

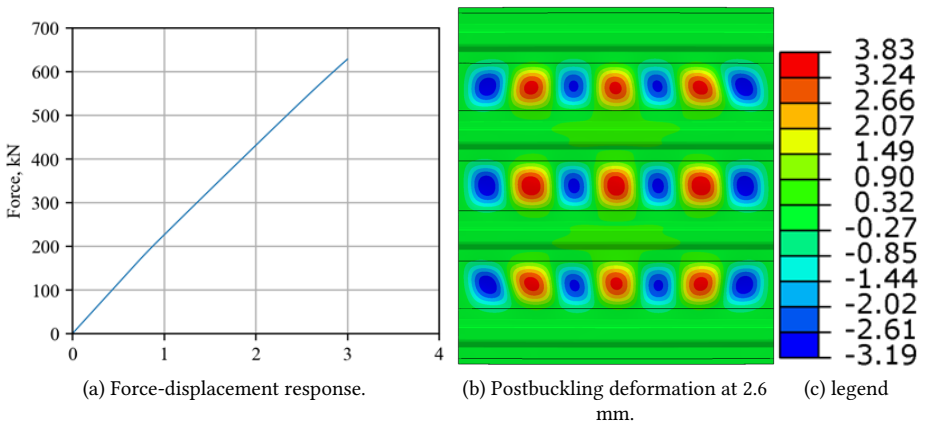


Figure 4.13: The postbuckling response of the four-stringer panel with thick stringers without cohesive elements. The blue half-waves indicate that the skin bends away from the stringer.

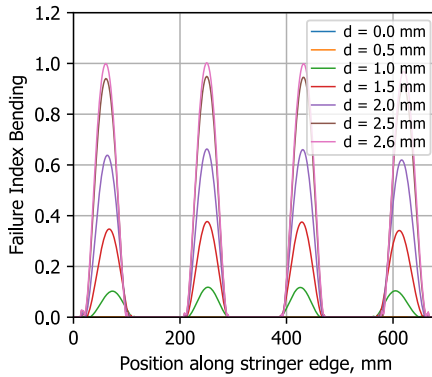


Figure 4.14: Failure index due to bending in the four-stringer panel with thick stringers. The index is calculated along the full length of the panel and displayed here for every 0.5 mm applied displacement increment until it exceeds 1 at 2.6 mm.

The bending moment and the twisting moment along the stringer edge at applied displacements 2.6 mm are shown in figure 4.15. The moments are taken from the three elements along the flange edge. The blue line labelled *s* represents the moments in the skin outboard of the flange edge, the line *sf1* represents the moments in the skin where the skin and flange overlap and the line *sf2* represents the moments in the flange. The bending moment is significantly higher than the twisting moment. The bending moment is maximum at the points where the maximum out-of-plane deformation is observed. The twisting moments are approximately zero at the locations of maximum bending, showing that ignoring the twisting moment in the analytical model for bending is valid.

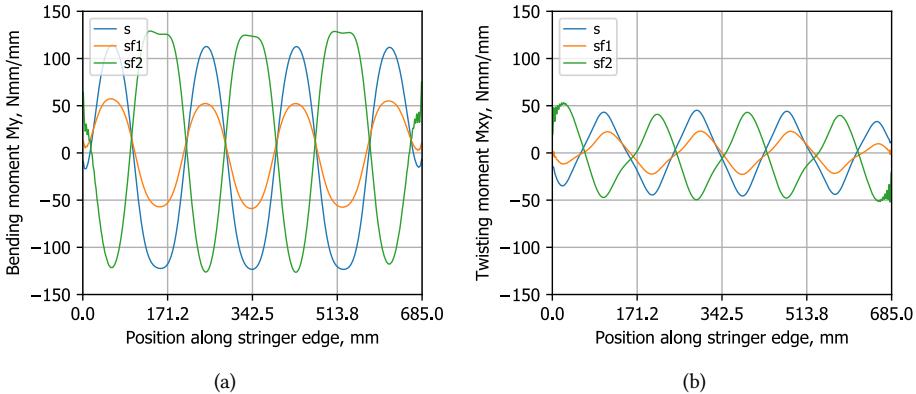


Figure 4.15: Bending and twisting moments at the critical displacement of 2.6 mm.

The results of the cohesive model are collected in figure 4.16. Cohesive failure accompanied by a load drop is observed at an applied displacement of 2.37 mm a. The displacement is 9% lower for initiation compared to the analytical criterion.

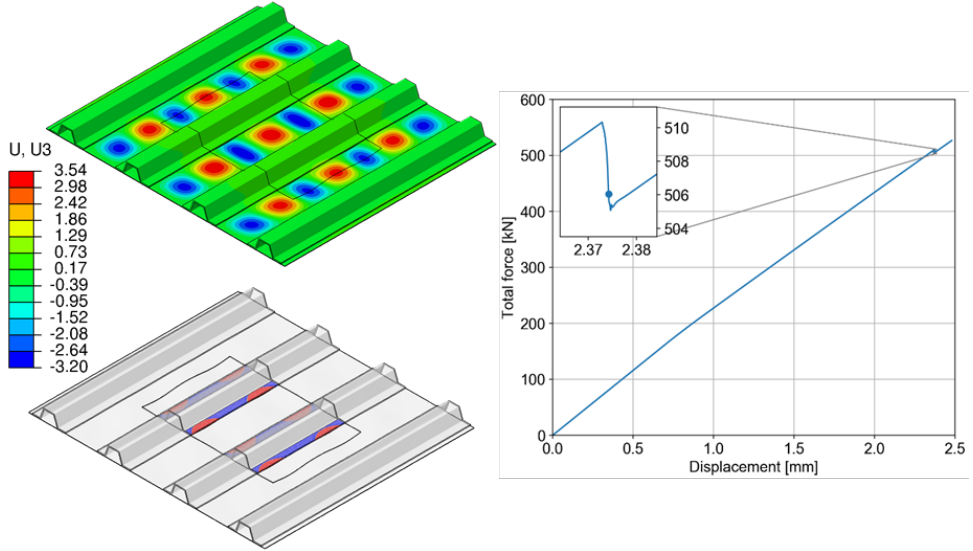


Figure 4.16: The postbuckling and separation results of the thick stringer panel model with cohesive elements for the verification of the displacement and critical locations.

The cohesive model confirms that separation is predominantly present at the location of maximum out-of-plane deformation (3rd and 5th half-wave). The output frame of the simple model containing the postbuckling deformation at 2.4-2.6 mm should be used to design the single-stringer specimen in a seven-point bending configuration in chapter 5.

4.4.2 THIN STRINGER PANEL: TWISTING FAILURE

The force-displacement response and buckling pattern of the thin-stringer panel are shown in figure 4.17. The thin flange of the stringer tends to bend with the skin. Generally, an (effectively) wider bay for the same length can lead to fewer buckling waves, in this case, the panel presents five buckling half-waves. The out-of-plane deformation of the skin is significantly higher relative to the panel with thick stringers. This is a combination of the fewer half-waves and the more compliant stringer flange.

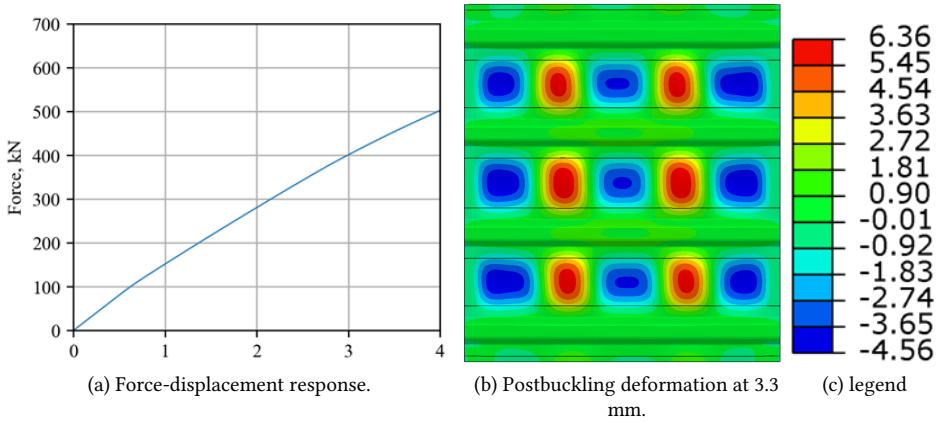


Figure 4.17: The postbuckling response of the four-stringer panel with thin stringers without cohesive elements.

The failure index plot of this panel is presented in figure 4.18. Even at 4 mm applied displacement, the index calculated for bending initiation does not exceed 0.15. This indicates that the thin stringer panel is not prone to fail in bending.

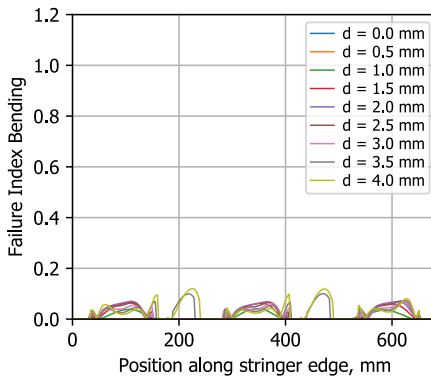


Figure 4.18: Failure index due to bending in the four-stringer panel with thin stringers.

The bending and twisting moments are shown in figure 4.19. The distribution is flipped compared to the thick stringer panel in figure 4.15, where the twisting moment is >3x higher compared to the bending moment. Therefore it is very likely that this panel will exhibit separation due to twisting before bending separation occurs.

The failure mode is verified by the model with cohesive elements, shown in figure 4.20. Indeed separation occurs at the locations of maximum twisting around an applied displacement of 3.3 mm. The output frame of the simple model containing the postbuckling deformation at 3.3 mm should be used as a reference to design the single-stringer specimen to be tested in a four-point twisting configuration in chapter 6.

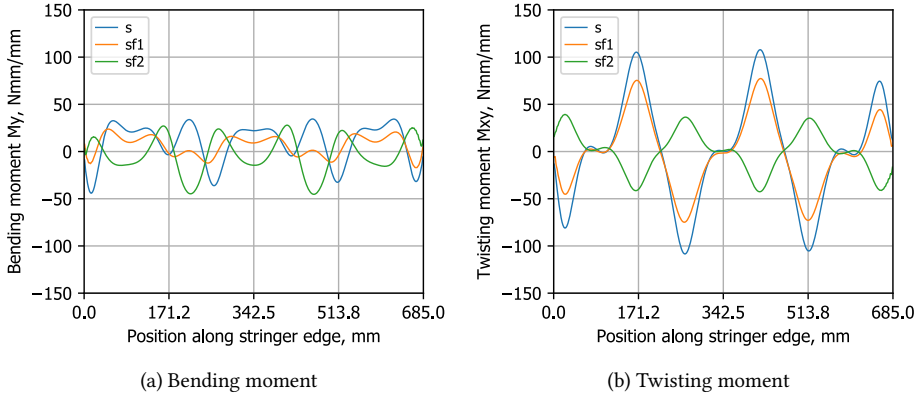


Figure 4.19: Moments at the critical displacement of 3.3 mm. The magnitude of the twisting moment, at the inflection points, is higher than the maximum bending moment.

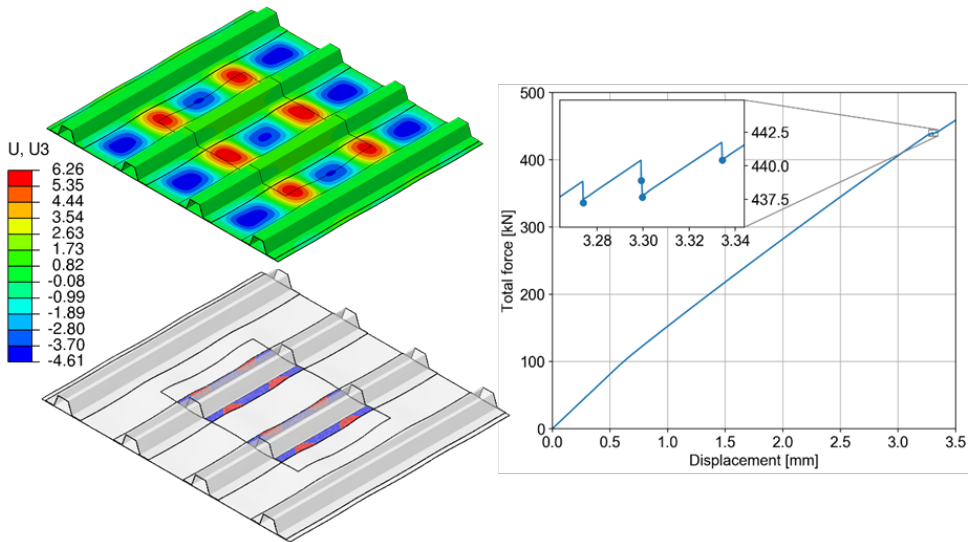


Figure 4.20: The postbuckling and separation results of the thin stringer panel model with cohesive elements, showing separation at the inflection points.

4.5 CONCLUSIONS

An analytical approach was developed to predict the initiation of skin-stringer separation, considering the moments along the skin-flange cross-section. The criterion uses the principle that when the stringer separates from the skin, the separated stringer part will be unloaded. In contrast, the separated skin part will become equal to the skin part that is adjacent to the edge.

The criterion is semi-analytical and works in conjunction with finite element. Three sets of elements are created within the models, each one contains all the elements at the cross-sectional location of the skin, the skin and the flange of the skin-flange overlap at the flange edge. A Python script requests the output in CSV, which is combined with the input file containing the material properties and material section definitions. For every output frame of the finite element model, the failure index can be calculated along the complete flange edge of the model.

The criterion was first implemented in a flange bending model that behaves in 2D but does have continuum shell elements. The criterion is mesh-dependent for the stringer flange but independent of the skin mesh size. Only the last element of the flange needs to be refined to approximately 0.3 mm.

Comparing the results of the criterion to a skin-flange bending model with cohesive elements showed a correlation of 0-3% for low interface strengths. The low interface strengths simulate a pre-damage-like condition in the cohesive model, which is assumed in the criterion.

Using the proposed criterion in the four-stringer panel, it is possible to estimate at which applied compression displacement and predict at which location skin-stringer separation occurs. The criterion indicated initiation at 2.6 mm at the maximum out-of-plane displacement locations for the four-stringer panel with thick stringers. Similarly, a cohesive model of the same panel showed separation at these locations, but already at 2.4 mm. The four-stringer panel with thin stringers did not exceed the failure index of the criterion. The panel with cohesive elements also agreed that separation due to bending does not occur. Separation was observed instead due to twisting in between the half-waves at 3.4 mm.

The next step in the methodology is using the results obtained from the criterion, at which applied compression displacement and at which location skin-stringer separation occurs, to select the appropriate test configuration. Specifically for separation due to a high twisting moment, a four-point twisting configuration would be considered. However, in the case of initiation due to a high bending moment using a seven-point bending test is most appropriate.

5

A SEVEN-POINT BENDING CONFIGURATION TO CAPTURE SKIN-STRINGER SEPARATION

5

Skin-stringer separation can occur in two regions of a four-stringer panel: the region of maximum deflection and the region of maximum twisting. A seven-point bending configuration, in which five supports and two load points induce buckling waves to the specimen, can mimic the deformation in the region of maximum deflection. An optimization procedure to find the placement of the supports and load points minimizes the error between the representative single-stringer specimen's out-of-plane deformation and the panel's corresponding region. The separation behaviour was studied using a combination of numerical models and experimental tests. The peak of the normalized force in the central load cell was a good indicator for initiation. The separation shape was similar between the tests and the models and independent of the interface properties. Removing the R-curve effect for mode II had a negligible influence on the separation response. During the tests, separation became unstable above a separation length of 15 mm, 60% of the flange width. A 107 Nmm/mm local bending moment triggered separation in the single-stringer specimen. Applying this value as an allowable to identify initiation in the four-stringer panel resulted in a correlation of 0.4%. Furthermore, the seven-point design recreates the local moment distribution observed in the panel. The designed single-stringer specimen well represented the shape of separation in the four-stringer. Even in the panel, separation was perfectly elliptical, but the focal points moved close to each other during propagation. The seven-point bending test proved to be a good test for skin-stringer separation in postbuckling conditions with a significant reduction in required load (<1%) and more manageable tracking of separation growth.

5.1 INTRODUCTION

This chapter presents a numerical and experimental investigation of the seven-point bending test for the characterization of skin-stringer separation failure in postbuckled composite multi-stringer panels. In chapter 4, the critical postbuckling shape of the four-stringer panel has been determined. Specifically, in the panel with thick stringers, separation in mode I is dominant. The design of a single-stringer specimen based on the postbuckling deformation of a four-stringer panel is shown as well as the resulting skin-stringer separation response.

This chapter serves the following purposes:

Chapter goals

- **section 5.2:** Determine the design of the single-stringer specimen to mimic the critical postbuckling conditions.
- **section 5.3:** Observe the initiation and propagation behavior of an out-of-plane loaded panel with different interface properties.
- **section 5.4:** Characterize the interface failure mechanisms in a postbuckling-like induced skin-stringer separation.
- **section 5.5:** Compare the finite element models to the experimental tests to illustrate the effectiveness of the models and to judge the material properties that are used.
- **section 5.6.1:** Update the initiation allowable and compare the forces and moments along the edge of the single-stringer specimen to the four-stringer panel.
- **section 5.6.2:** Verify the ability of the single-stringer specimen to reproduce the skin-stringer separation behaviour by comparing it to the four-stringer panel.

5

5.2 DETERMINING THE SINGLE-STRINGER SPECIMEN CONFIGURATION

The out-of-plane deformation of the skin in the four-stringer panel of chapter 4 at the buckling half-wave spanning from 380 mm to 480 mm is being matched by a single-stringer specimen in a seven-point bending configuration. The out-of-plane deformation of the panel at an applied compressive displacement of 2.2 mm is plotted in figure 5.2a. The conclusion from chapter 4 was that initiation would occur at 2.4-2.6 mm and that displacement should be taken as a reference, but due to the order of the performed work 2.2 mm was initially deemed to be critical. There is no postbuckling shape change, but only a change in magnitude so its effect would be minimal.

A single-stringer specimen in a seven-point bending configuration is designed according to the method described in section 2.4. The design parameters of the model were shown in figure 2.6. The length of the specimen is approximately the length of a buckling half-wave and the width is related to the stringer spacing of the multi-stringer panel. In this case, the dimensions are $L=140$ mm and $W=254$ mm, respectively.

A total of 121 models with different positions of the supports and loading points have been analyzed numerically and the shape error has been calculated. Two variables were changed, the transverse distance between the edge and the supports (S_Y) and the loading point (L_Y). The calculation of S_X based on S_Y has been described in section 2.4. For each

variable 11 different locations were chosen; starting at 20 mm with an increment of 4 mm up to 60 mm from the bottom edge of the skin.

Four distinct results of a seven-point bending configuration with different positional variables are shown in figure 5.2b-e with the same deformation scale as the panel. The shape error for each of the 121 combinations is calculated following the method presented in section 2.4. The surface plot of the shape errors is shown in figure 5.1, where a low error valley is present along the $S_Y = L_Y$ line. The optimum configuration is found at $S_Y = 36$ mm and $L_Y = 36$ mm and $S_X = 24$ mm, which corresponds to the design illustrated in figure 5.2b and figure 5.3.

The four designs of figure 5.2b-e illustrate the effect that the placement of the supports and loading points have on the induced deformation. In figure 5.2c, having the same distance for the supports and loading points to the edge, but too close to the stringer flange, results into a large wake below the loading points. In figure 5.2d, with only the loading point close to the flange, a local dimple is created which is not allowed to go into a half-wave due to the restricting supports in the corner. Oppositely in figure 5.2e, with only the supports too close to the flange the loading point causes only the bending of the skin itself over 1 direction, which looks similar to a 3-point bending-induced deformation.

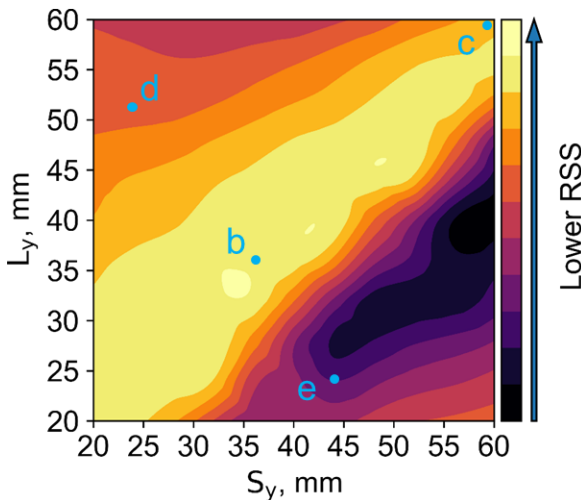
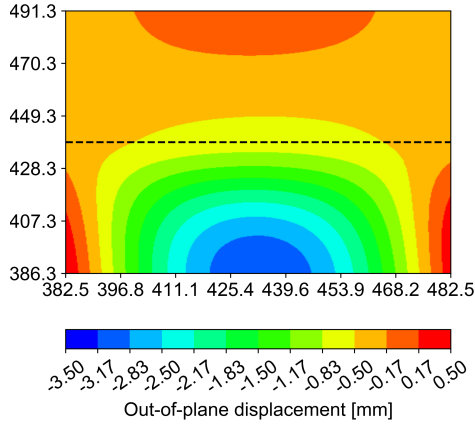
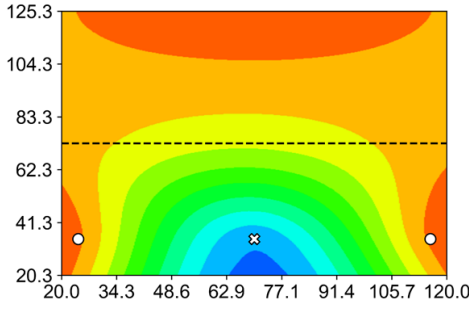


Figure 5.1: The shape error for all 121 configurations (different combinations of S_Y and L_Y), with the four designs of figure 5.2 indicated as b-e. A lower RSS corresponds to a better approximation of the actual postbuckling shape of the panel.

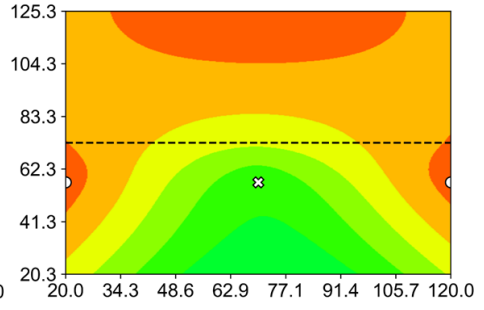


(a) Panel

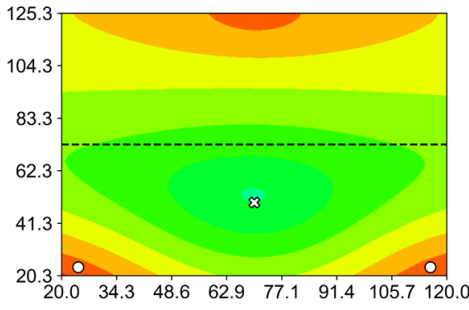
5



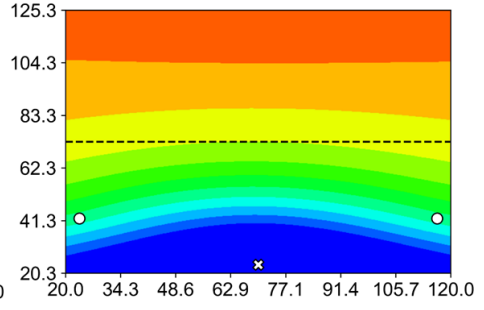
(b) $S_Y = 36 \text{ mm}$, $L_Y = 36 \text{ mm}$



(c) $S_Y = 60 \text{ mm}$, $L_Y = 60 \text{ mm}$



(d) $S_Y = 24 \text{ mm}$, $L_Y = 52 \text{ mm}$



(e) $S_Y = 44 \text{ mm}$, $L_Y = 24 \text{ mm}$

Figure 5.2: a: The critical region of the four-stringer panel to be compared to the single-stringer specimens; b-e: Single-stringer specimens in a seven-point bending configuration with different positional variables, displayed by the circles and crosses for the supports and loading points, respectively. All subfigures use the scale of a.

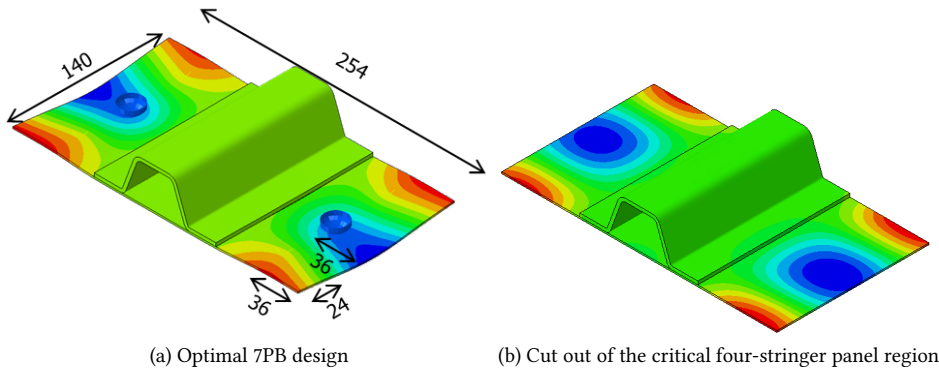


Figure 5.3: Optimal design (figure 5.2b) for a single-stringer specimen in a seven-point bending configuration and the corresponding four-stringer panel region (figure 5.2a). The area considered in the comparison excludes the 20 mm along the border.

5.3 PREDICTING SEPARATION THROUGH COHESIVE ZONE MODELLING

5

To analyze separation in the single-stringer specimen, an FE model was created using the method discussed in section 2.3. Within the model different interface properties were used, corresponding to the results of material characterization presented in table 3.1. The first set of cohesive elements, following the unidirectional properties of Clay et al.[102] (Gclay), is used as the baseline and lower bound prediction of the tests. This allows the identification of the earliest possible initiation point. The steady-state (GSS) is used as an upper bound, to capture the maximum possible load, which can be vital for selecting the appropriate test rig and load cells. The remaining models follow a trilinear cohesive behaviour (Gclay-GSS, Gclay-GII0, and G0-GSS), which considers the toughening effects due to fibre bridging and possible delamination migration.

The force-displacement response, including the individual loading point and support point, of the baseline is shown figure 5.4. Due to the perfect and symmetric loading conditions, the curves of LC1 and LC2 overlap as well as the curves of LC3+LC7 and LC4+LC6. The layup creates a bias, because of the selected -45 outermost ply, leading to a slight difference in LC6 and LC7. The central support takes up a lower load compared to the corner supports.

The total force response of the five models and the normalized force of the centre support point are presented in figure 5.5, a and b respectively. The increase in the compliance in the force-displacement curve is due to the initiation of separation, which also corresponds to the peak of the normalized central force. The point of initiation is mainly higher for G0-GSS and GSS as the mode II critical strain energy release rate is higher. The trilinear models that include Gclay initiate at the same point as the bilinear Gclay model and reach the same displacement for the maximum load as the bilinear GSS model.

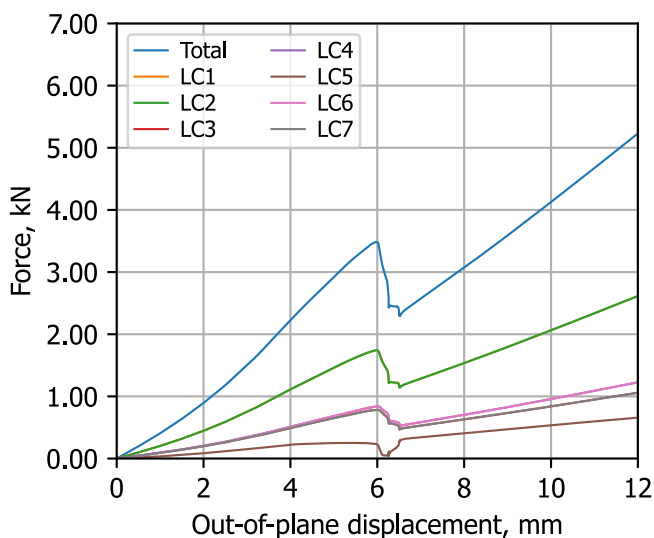


Figure 5.4: The force distribution in the supports and loading points plus the total force in the baseline Gclay seven-point bending model with cohesive elements.

5

The displacement and load at the point of initiation values, based on the first cohesive element failure as well as from identifying the max of the normalized force are reported in table 5.1. The table also includes the force and displacement at which the maximum load has been reached. The peak of the normalized central force is a good indicator of the initiation as it matches with cohesive initiation.

Table 5.1: Initiation and max load of the seven-point bending models.

	Norm init. mm	Coh init. mm	Force init. kN	Disp at max load mm	Max load kN
Gclay	3.77	3.84	2.11	5.99	3.49
Gclay-GSS	3.85	3.86	2.13	7.21	4.74
Gclay-GII0	3.91	3.91	2.17	7.20	4.73
G0-GSS	4.32	4.32	2.51	8.00	5.69
GSS	4.50	4.50	2.67	7.33	4.90

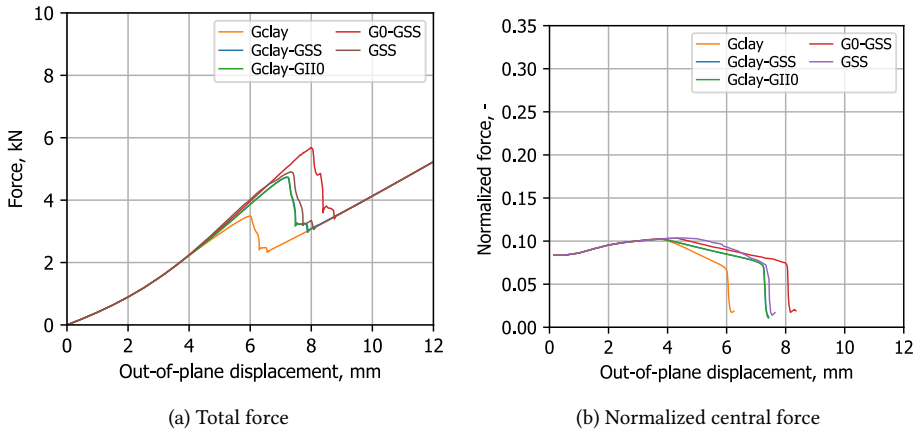


Figure 5.5: Force-displacement response of the numerical models for different interface properties.

For Gclay-GSS, the out-of-plane deformation plots as well as the interface damage at different stages of separation growth are illustrated in figure 5.6. The postbuckling-like deformation is somewhat constant, but when the stringer has fully separated the shape is more similar to a tunnel as also observed in stiffened panels[5, 7]. The fracture processing zone length of the primary set of cohesive elements, which models the initiation of separation, is short at 1 mm. Oppositely, for the secondary set, which represents the toughening R-curve behaviour, the length is >20 mm, which is almost equal to the full flange width.

5

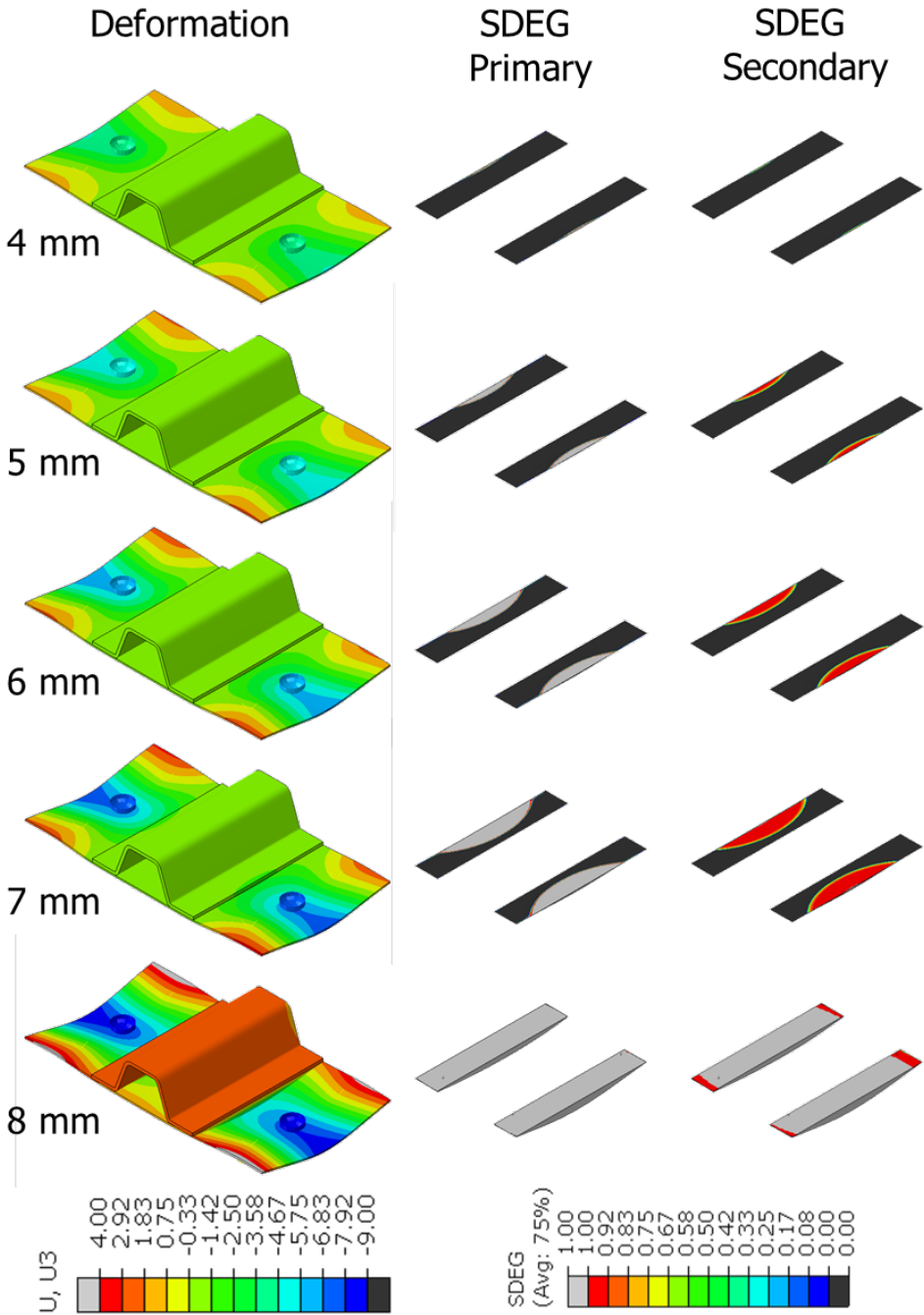


Figure 5.6: Deformation and interface separation for different loading amplitudes between initiation and failure for the seven-point bending model with Gclay-GSS properties. For the SDEG variable: grey is separated, black is intact and coloured is currently active in the cohesive processing zone. Primary corresponds to the cohesive elements modelling initiation and secondary to the elements that capture the R-curve effects.

The global mixed-mode conditions for both initiation and propagation and each cohesive set are shown in figure 5.7. Initiation in the primary set is purely due to shearing. Evolution in the primary set is approximately at a mode-mixity of 20-50%, where the closer to the inner edge the more mode I is present. This is because the arm that applies the moment is a combination of the initial distance to the edge plus the separation width, so an increase in this arm increases the mode I component. The secondary set of cohesive elements undergoes pure mode I failure, which was also observed in the mixed-mode bending tests from section 3.6. This is why there is no difference between the Gclay-GSS and Gclay-GII0 models in figure 5.5, which means that the assumption from section 3.6 about ignoring the mode II R-curve effect is valid.

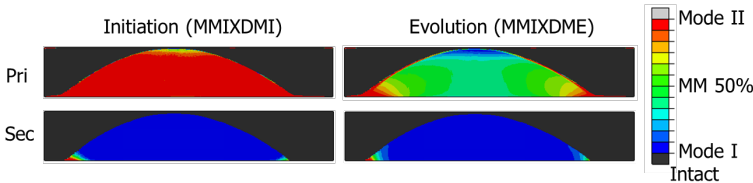


Figure 5.7: Mixed-mode conditions at initiation and full evolution for the pri(mary) Gclay and sec(ondary) GSS set of cohesive elements in the Gclay-GSS models.

The speed of propagation of skin-stringer separation, both in length and width direction, is shown in figure 5.8. The rate of growth of the separation width increases with the applied displacement. Oppositely, for the separation length, an initial large increase is observed after which the rate slows down until a final quick jump in length and width, corresponding to total separation.

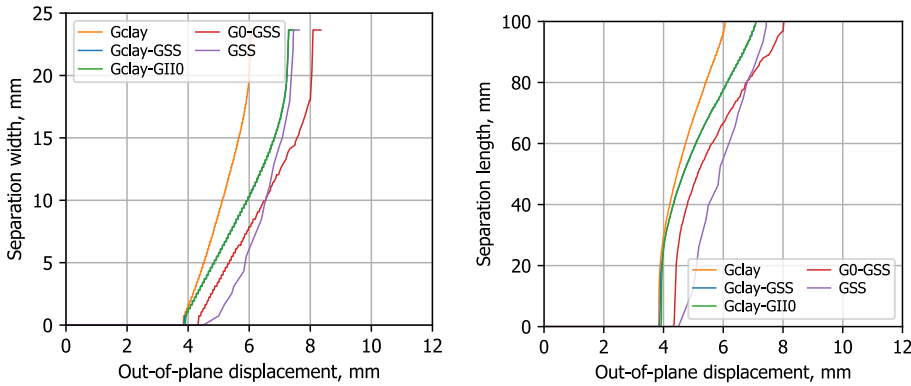


Figure 5.8: Separation sizes for all seven-point bending models.

The speed of the propagation differs between the models, but the shape of the separation front is similar. The separation fronts, including the elliptical approximation, are shown at intervals of 5 mm in figure 5.9. The corresponding plot of the separation width versus length, figure 5.10, highlights that the separation fronts are still similar between the models with the different interface properties.

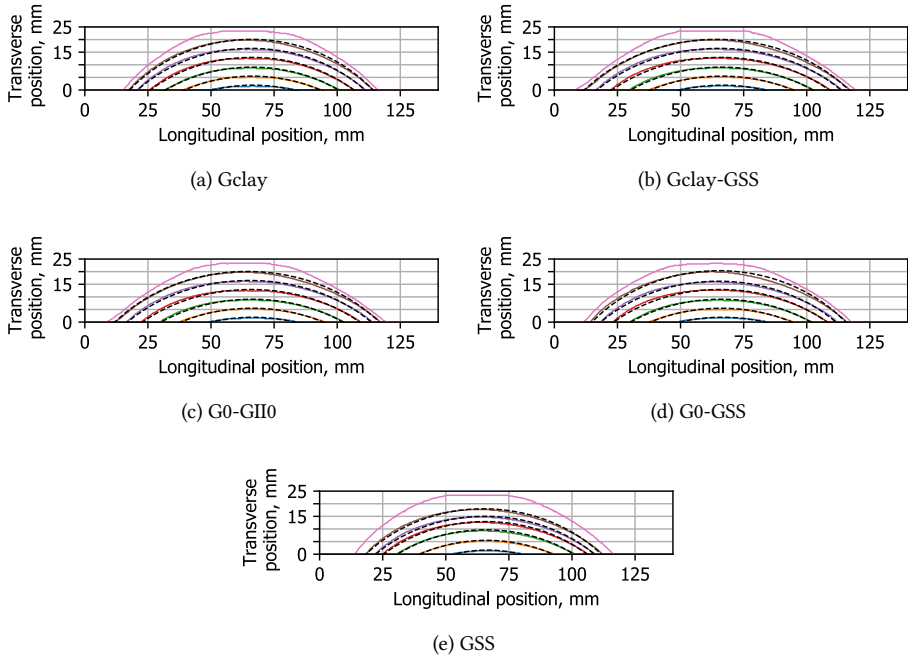


Figure 5.9: Separation fronts and elliptical approximations (dashed) at different stages of separation growth; a subfigure for each seven-point bending FE model.

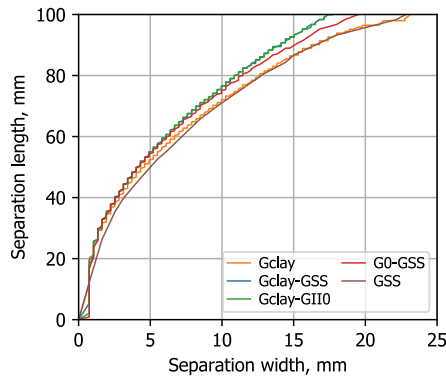


Figure 5.10: Effect of the interface properties on the elliptical separation shape defined by its length and width.

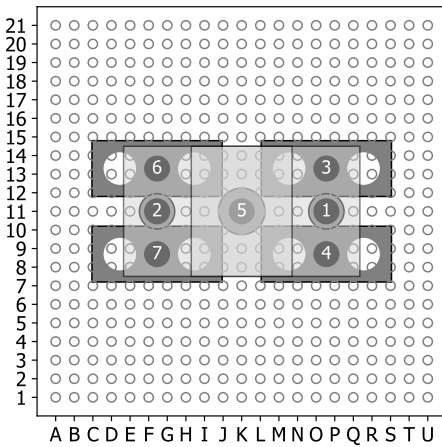
5.4 TESTING OF SKIN-STRINGER SEPARATION

For the tests in a seven-point bending configuration, four composite single-stringer specimens were manufactured (7PB7 to 7PB10), shown in figure 5.11. The alignment schematic and the setup for the seven-point bending configuration are illustrated in figure 5.12.

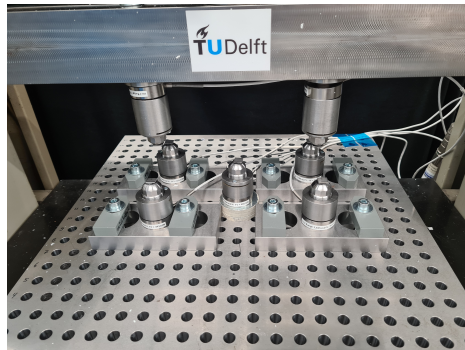


Figure 5.11: Four in-house manufactured single-stringer specimens for testing in seven-point bending.

5



(a) Schematic for alignment



(b) Physical setup

Figure 5.12: Layout of the seven-point bending configuration.

The lowest prediction of initiation in the FE models was at 3.5 mm and the highest displacement until the separation width reaches the maximum value was just below 8 mm. Hence, the three specimens were stopped at 3.0 mm and tested up to 8.0 mm with an increase of 0.5 mm per run, plus an additional run to remove the stringer. This resulted in a total of 12 individual load runs per specimen.

In figure 5.13a, the force-displacement response is plotted for each individual run of specimen 7PB8 including a stitched curve representing the total response of the specimen. After the separation is initiated the compliance of each individual run increases. The maximum load of 4.5 kN was reached at 7.0 mm displacement. The loadcell distribution in figure 5.13b shows that the left side becomes unstable first, which can be caused by manufacturing imperfections. The force-displacement curves and the normalized central force of the four specimens are shown in figure 5.14 with the summarized results in table 5.2.

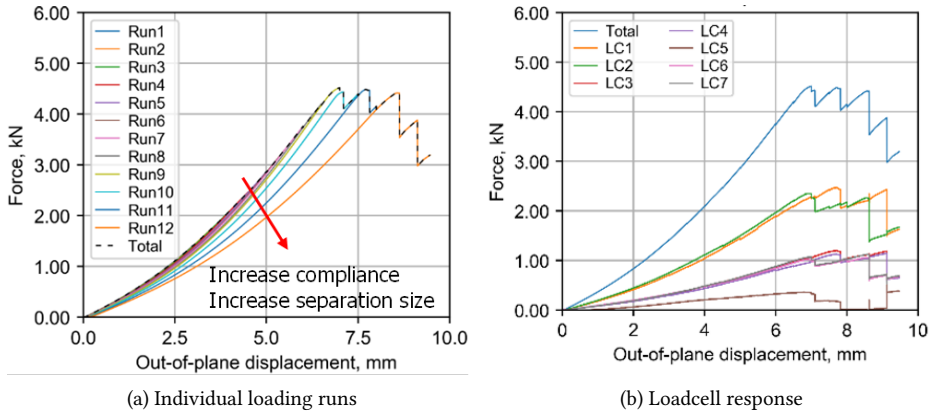


Figure 5.13: Force response of the 7PB8 specimen.

Table 5.2: Initiation and maximum load of the seven-point bending tests.

	Norm init. mm	Force init. kN	disp at max load mm	max load kN
7PB7	3.18	1.65	7.05	4.42
7PB8	3.57	1.79	7.00	4.52
7PB9	3.29	1.59	7.09	4.73
7PB10	3.54	1.77	7.17	4.67

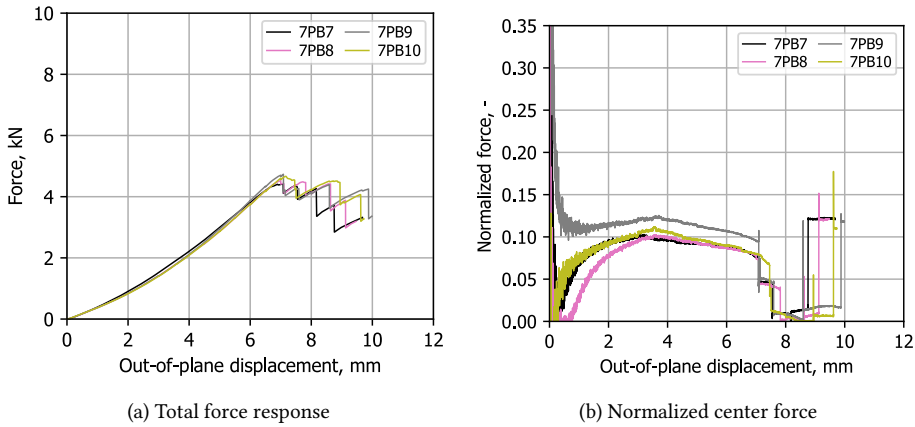


Figure 5.14: Force responses of all seven-point bending specimens.

The out-of-plane deformation and the C-scan after run 6 (at 4.5 mm) and run 11 (at 7.0 mm), are shown in figure 5.15. The trend of the out-of-plane displacement indicates that the specimen deforms similarly to the numerical models. The skin-stringer separation response, the red half moons, still follow an elliptical response as indicated by the overlapping dashed white lines. Specimens 7PB8 and 7PB10 initially show symmetric separation, but when the critical separation width was reached one side failed before the other. 7PB9 showed one-sided separation only, whereas the out-of-plane deformation plots still show a symmetric postbuckling-like shape.

The elliptical approximation of the separation front of the individual specimens is shown in figure 5.16. The red dots on the skin indicate the centre of the ellipses close to the loading points and the other dots represent the focal points close to the supports points. The colour of the dashed line corresponds to the end of each run, which was represented in figure 5.13. Two things can be observed from these graphs. Firstly, the separation size increases more quickly when closer to the maximum load; The C-scans were all spaced equally from each other with 0.5 mm applied out-of-plane displacement. Secondly, the ellipse becomes more circular as the focal points move closer to the centre at high separation.

The ellipse deviates from the separation front for the experimental test when a large part of the flange has separated, as illustrated in figure 5.17, which was not the case for the numerical models. This was attributed to separation migration into the top ply of the skin, as illustrated in figure 5.18. From the centre of the separation front, a -45° line can be drawn, where everything to the right experiences migration, caused by the separation front growing in a direction perpendicular to the fibres. Overall the elliptical shapes are similar to other single-stringer tests with bending failure, such as in the SSC tests[34, 69, 70, 116] and the other 7PB tests[79, 80, 82], where also delamination migration to the first and second skin ply was observed[80, 82].

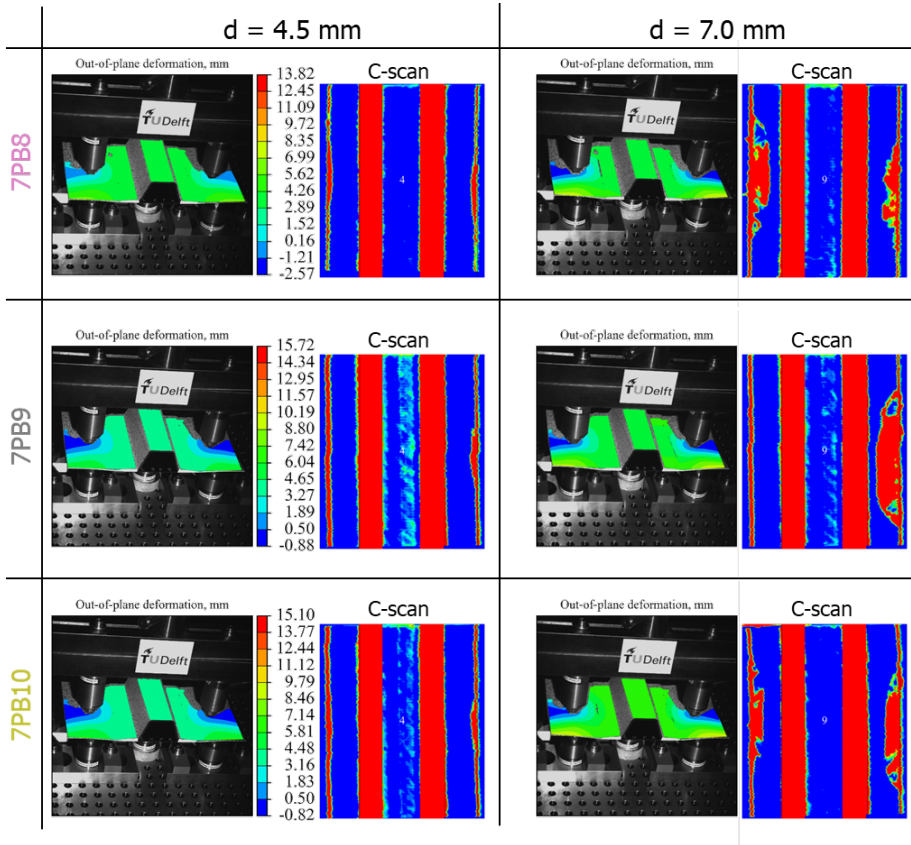


Figure 5.15: Out-of-plane deformation (DIC) and interface separation (C-scan) results of the seven-point bending tests at 4.5 and 7 mm of applied displacement.

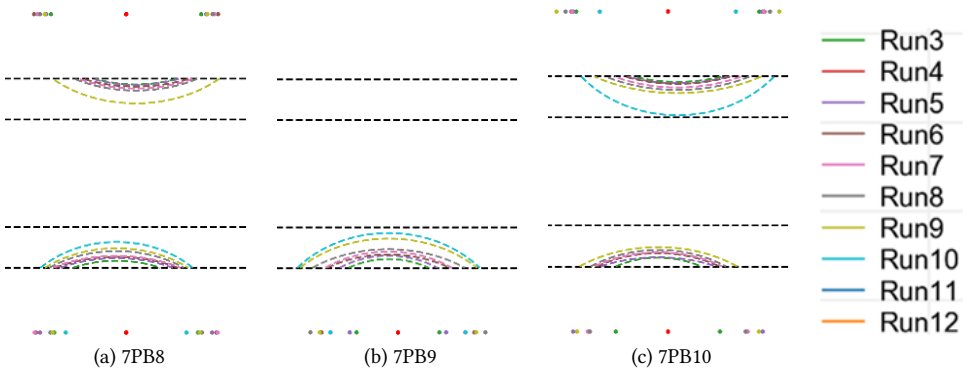


Figure 5.16: Elliptical approximation of the C-scans, where each coloured dashed line corresponds to the end of a loading run.

Matrix cracking and migration of separation cause R-curve effects that result in increased apparent fracture toughness, slowing separation along the propagation direction. The left side is therefore allowed to propagate at a faster rate since the front propagates parallel to the fibre direction. The combination of considering ply orientation and directionality of growth in cohesive zone modelling should further be investigated[117, 118].

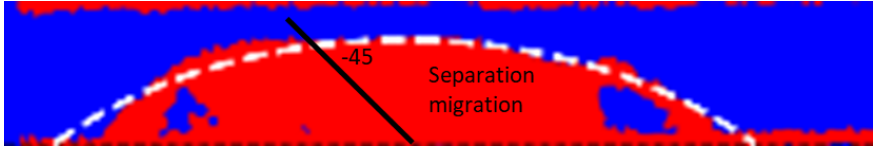


Figure 5.17: Interface separation, highlighting the separation migration location.



Figure 5.18: Side view of physical separation showing migration from the interface into the top skin ply.



Figure 5.19: Top view of the interface from skin side post-mortem, showing that the top ply is partially peeled off.

5.5 NUMERICAL-EXPERIMENTAL COMPARISON

Three aspects can be compared between the numerical model and the experimental results: 1) the initiation point, 2) the maximum load, and 3) the separation behaviour.

The total force-displacement response is shown in figure 5.20. There is good correspondence in terms of the stiffness between the models and tests. The trilinear Gclay-GSS is the closest match to the tests in terms of maximum force. The tests experience multiple sharp load drops after the maximum is reached, whereas in the numerical model it is just one continuous drop.

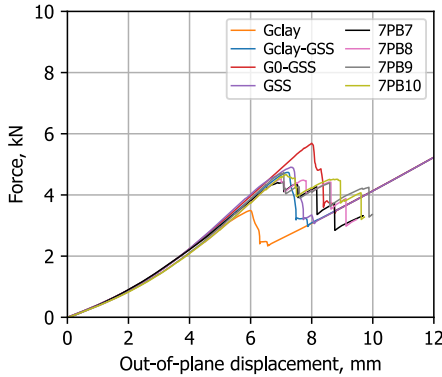


Figure 5.20: Force-displacement comparison between numerical models and seven-point bending tests.

The speed of separation propagation is compared in figure 5.21. The GSS model is not able to capture the initiation, whereas propagation is too fast in the Gclay model. The separation width is best captured by G0-GSS, whereas the separation length corresponds better to Gclay-GSS.

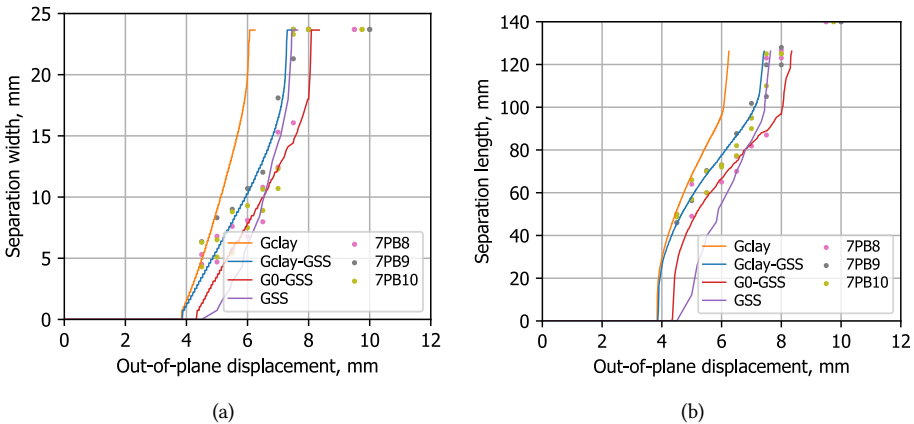


Figure 5.21: Comparing separation sizes between numerical models and tests.

When comparing the actual shape (figure 5.22a) it can be seen that the numerical models and tests show good similarity. Some deviations arise when the propagation is asymmetric, for example in specimen 7PB9 where separation only occurred on one side. However, the influence of the matrix cracking and delamination migration has only a limited effect on the actual propagation shape.

Another factor that can be compared is the load cell forces for the loading points at each side versus the separation width, as shown in figure 5.22b. Once more, the load at initiation is similar and starts to increase for a growing separation size. In all cases, the loadcell forces plateau around a separation width of 15 mm. This indicates that separation growth becomes unstable when the separation spans 60% of the total stringer width.

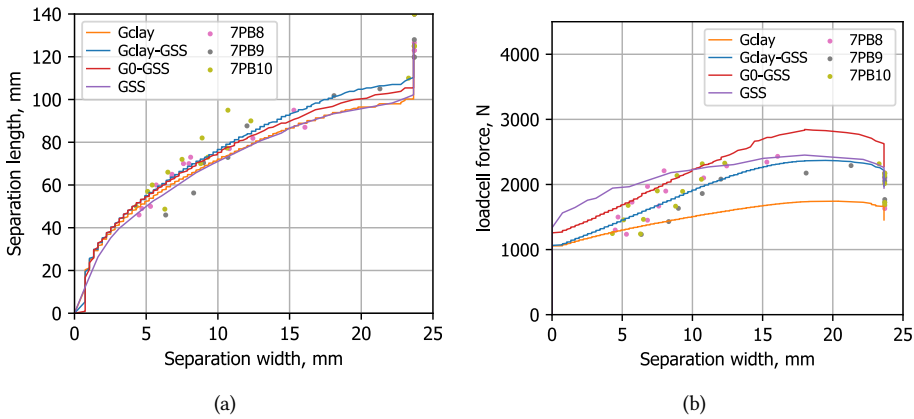


Figure 5.22: Comparing separation shape and loadcell load between numerical models and tests.

The force and displacement results of initiation and full separation of the tests are compared to the model with Gclay-GSS in table 5.3. Within 3% the maximum load is captured as well as a high correlation between the growth of separation in figure 5.21.

Table 5.3: Load comparison between numerical analysis and tests.

	Initiation		Maximum load	
	Disp, mm	Force, kN	Disp, mm	Force, kN
Gclay-GSS	3.86 (+7%)	2.13 (+17%)	7.21 (+2%)	4.74 (+2%)
Exp 7PB8	3.57	1.79	7.00	4.52
Exp 7PB9	3.70	1.90	7.09	4.73
Exp 7PB10	3.55	1.78	7.17	4.67
Exp Avg	3.61	1.82	7.08	4.64

For completeness, the similarity of the postbuckling-like deformation is highlighted in figure 5.23a/b as well as the corresponding separation in figure 5.23c/d for the Gclay-GSS model and 7PB8 specimen at 6 mm out-of-plane displacement.

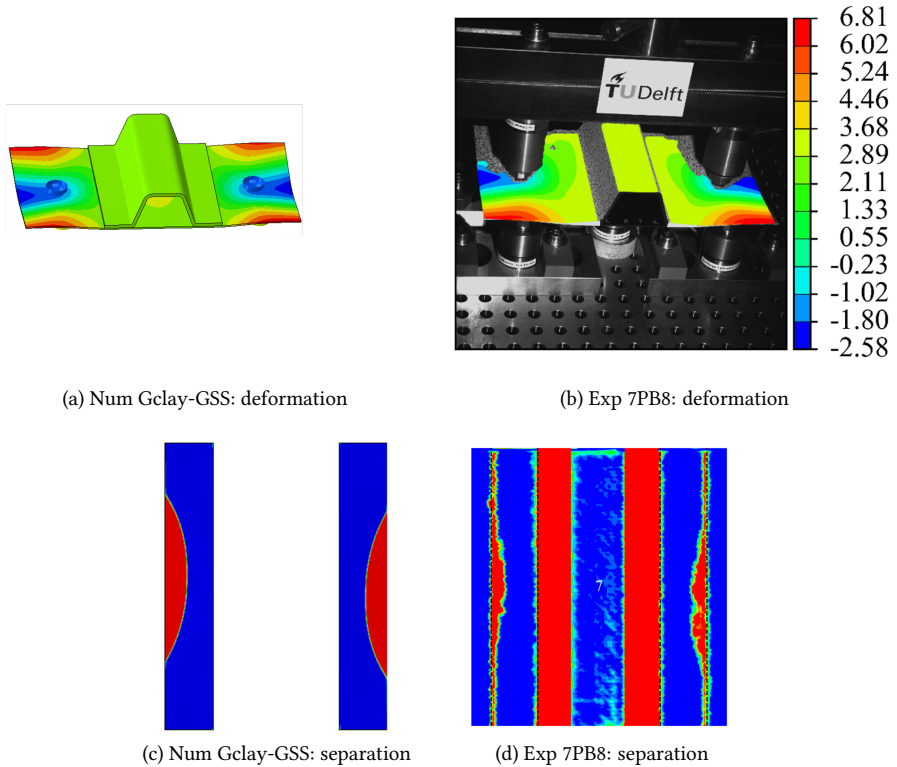


Figure 5.23: Out-of-plane deformation, sharing the same scale, and the corresponding interface separation at 6 mm of applied displacement.

5.6 INITIATION AND PROPAGATION OF SEPARATION IN THE FOUR-STRINGER PANEL

Initiation in the four-stringer panel can now be predicted using the outcome of the numerical and experimental work. Furthermore, the interface properties that best describe the propagation behaviour of a single-stringer specimen in postbuckling-like conditions can be implemented in the four-stringer panel model for a final prediction. Lastly, it can be illustrated that the separation shape of the four-stringer panel is captured within the seven-point bending test.

5.6.1 INITIATION OF SEPARATION AND FORCE/MOMENT DISTRIBUTION.

The results of the single-stringer specimens, numerical and experimental, can be used within the framework of the semi-analytical method. Instead of using the critical strain energy release rate as in the method described in section 5.6.1, the bending moment in the skin close to the stringer edge could be used, similar to [27]. It was also shown in figure 4.7 that the magnitude of the skin bending moment is independent of the mesh size (between 0.1-5.0 mm). The updated failure index calculation is stated in equation (5.1) and the rest of the framework remains the same as described in section 4.3.2.

$$FI = \frac{k_y D_{66}}{M_y^c} = \frac{M_y}{M_y^c} \quad (5.1)$$

From the FE model Gclay-GSS the maximum bending moment along the skin edge at initiation is taken as the new allowable M_y^c . The bending moment at the initiation of skin-stringer separation in the seven-point bending FE model is 107 Nmm/mm. For the tested single-stringer panels, no bending moment could be measured, however, the (mean) initiation force is known, 3.61 kN as presented in table 5.3. Plotting the force versus moment curve of the FE Gclay-GSS model in figure 5.24a, the moment corresponding to the force of 3.61 kN can be found, which is 100 Nmm/mm.

The allowables (107 and 100 Nmm/mm) can be used in the four-stringer panel model without the cohesive elements using equation (5.1) to predict initiation in the FE model and the experimental case. The maximum bending and twisting moments in the skin along the edge of the four-stringer panel is plotted in figure 5.24b.

Initiation in the finite element model of the four-stringer panel with Gclay-Gss properties is expected to occur at 2.38 mm, only 0.4% above what was predicted in section 4.4.1 with Gclay properties. However, it is more likely that the failure load in the experimental case is lower at 2.22 mm. Albeit, this won't be validated as testing the four-stringer panel is outside of the thesis scope.

In order to understand the similarity in the loading distribution around initiation for this optimised seven-point bending configuration, the bending/twisting moments and normal/shear forces are shown in figure 5.25.

Within figure 5.25a all three moment components of the single-stringer specimen match the four-stringer panel. Especially in between the supports, which are located at the top/bottom of the twisting moment (M_{xy}).

Within figure 5.25b only the shear force (N_{xy}) is captured. The force acting orthogonal to the stringer flange (N_y) can add an additional mode II loading of the interface. The normal force in the longitudinal direction (N_x) is higher as the four-stringer panel is directly loaded by this compressive force. At initiation, the influence of N_x is negligible as it is loading a zero-thickness cohesive element, which does not take in-plane forces into account. However, the lack of this compressive force can influence the propagation behaviour as it can cause the stringer flange to buckle as well if it is (partially) separated[119–122].

5

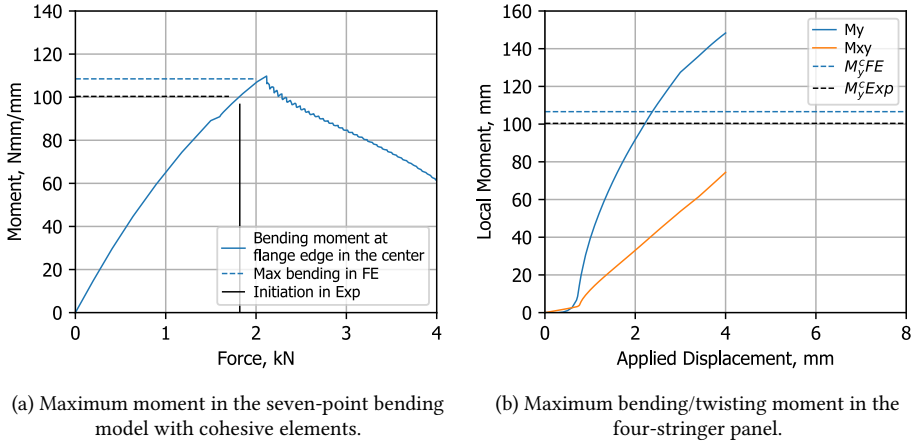


Figure 5.24: Maximum bending moment along the skin-flange edge that can trigger initiation of skin-stringer separation.

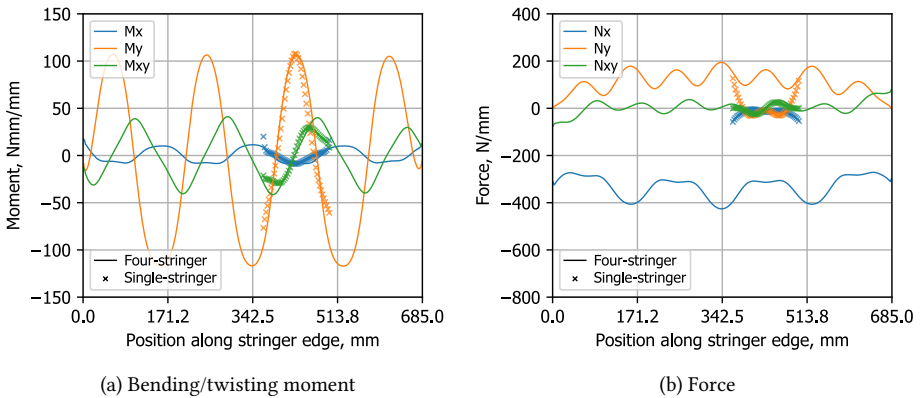


Figure 5.25: The bending/twisting moments and normal/shear forces in the skin along the edge of the four-stringer panel and the single-stringer in 7PB around the expected initiation load.

5.6.2 PROPAGATION AND SHAPE OF SEPARATION.

For the final prediction of failure as well as the verification of the methodology, the Gclay-GSS properties are implemented in the four-stringer panel with cohesive elements. The propagation behaviour, specifically the shape, can be compared to the single-stringer results to show if/that the 7PB configuration captured the behaviour.

The postbuckling shape at 2.9 mm applied compressive displacement and the mode-mixity at the partially separated interface is shown in figure 5.26. Following the same procedure as for the numerical model of the single-stringer specimen (section 2.3.3), the separation front in the four-stringer panel can be approximated as an ellipse. The assumption is made that the centre of the ellipse is 37 mm from the stringer edge as shown in figure 5.26, which is the same distance (v) between the edge and the loading point for the seven-point bending specimen.

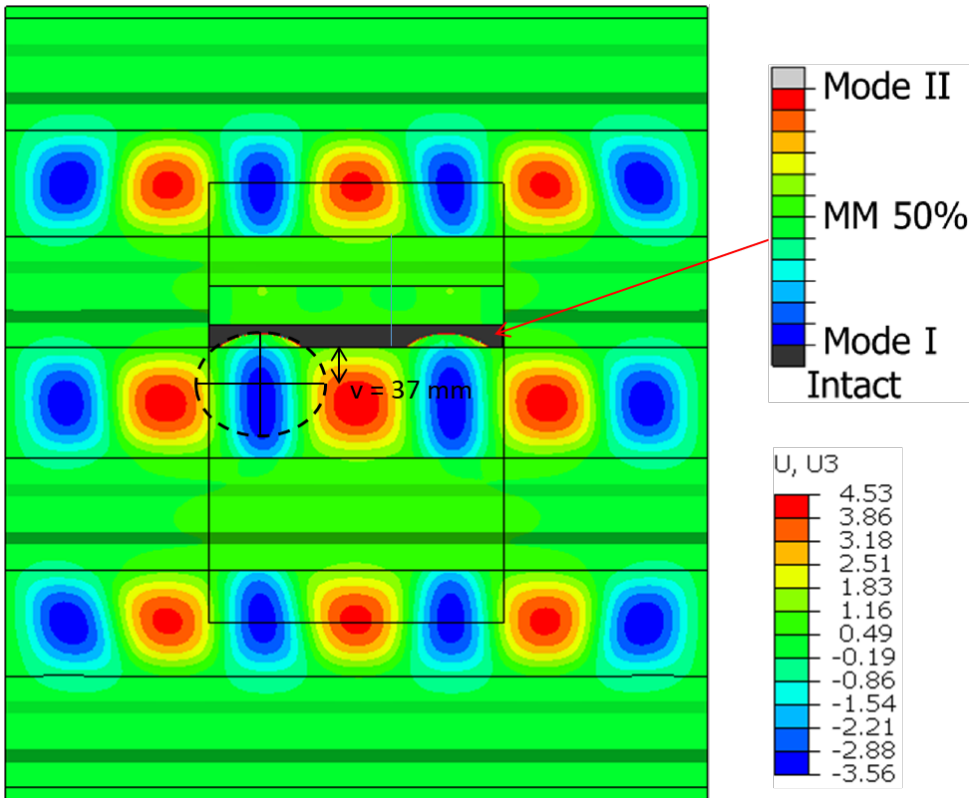


Figure 5.26: Postbuckling deformation of the four-stringer panel at 2.9 mm. A section of the hat-stringer is removed for illustration to show the interface, where the mode-mixity is shown in the cohesive zone. The interface separation is approximated with an ellipse.

The force and the separation width response versus applied displacement is plotted in figure 5.27 for the seven-point bending and four-stringer panel model using the Gclay-GSS interface properties. Note that the x-axis says applied displacement, the four-stringer panel is subjected to in-plane loading as opposed to out-of-plane for the seven-point bending configuration. Even though the results are not comparable in figure 5.27a, it shows that the maximum load for the single-stringer specimen required from the test machine is almost 1% with respect to the four-stringer panel.

In figure 5.27a it can be seen that in the four-stringer panel buckling occurs around 0.8 mm, initiation at approximately 2.35 mm and the stringer has fully separated at 3.4 mm. The load-carrying capabilities are 4x the buckling displacement, or 3x for initiation.

The separation grows to its full length in a millimetre of applied (in-plane) displacement, as opposed to 3.4 mm of applied out-of-plane displacement, from 3.5 to 6.9 mm, for the seven-point bending specimen. This larger increment allows for easier monitoring of separation during testing, which is particularly useful for the development of structural health monitoring methods[123, 124].

5

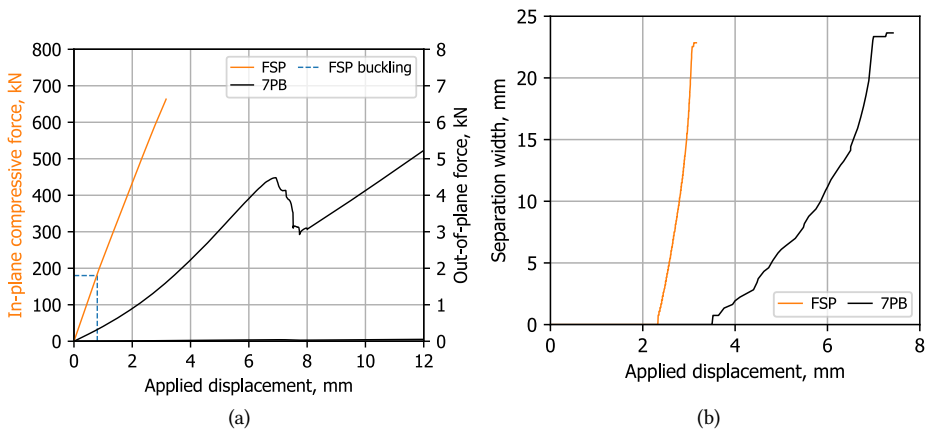


Figure 5.27: Comparing force and separation width versus applied displacement, with in-plane displacement for the panel (FSP) and out-of-plane for the single-stringer model (7PB).

For different separation widths, the actual crack front is compared to the elliptical approximation in figure 5.28. The results show that the skin-stringer separation shape due to postbuckling is perfectly elliptical, even more so than the representative seven-point bending specimen.

The overall separation shape of the four-stringer panel is comparable to what was predicted with the seven-point bending specimens, as can be seen in figure 5.29a. Up to a separation width of 8 mm, the 7PB is able to capture the shape of FSP correctly. It is assumed that at least up to this point the same mixed-mode conditions and the delamination migration observed in the tests will therefore be present in the panel. After a separation width of 12 mm, the shape of 7PB starts to deviate from the FSP, where mainly the separation length is shorter for the same width. However, as observed from figure 5.29b, separation tends to become unstable after a width of 12-15 mm.

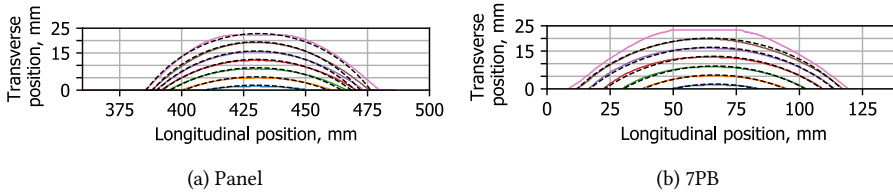


Figure 5.28: Separation front comparison between the four-stringer panel and the single-stringer specimen (7PB).

In the four-stringer panel, separation results in a shortening of the buckling half-wave and causes the inflection points to move closer to each other. For the 7PB, the position of the support points is initially selected to be on the inflection points of the multi-stringer panel. In the single-stringer specimen, the supports define the focal points of the ellipse. The results suggest that in the four-stringer panel, the inflection points of the buckling wave define the focal points of the ellipse. Therefore the shortening of the half-wavelength leads to a decrease in the focal point distance as shown in figure 5.29b. This subsequently leads to an overall decrease in the separation length growth with respect to the single-stringer specimen.

5

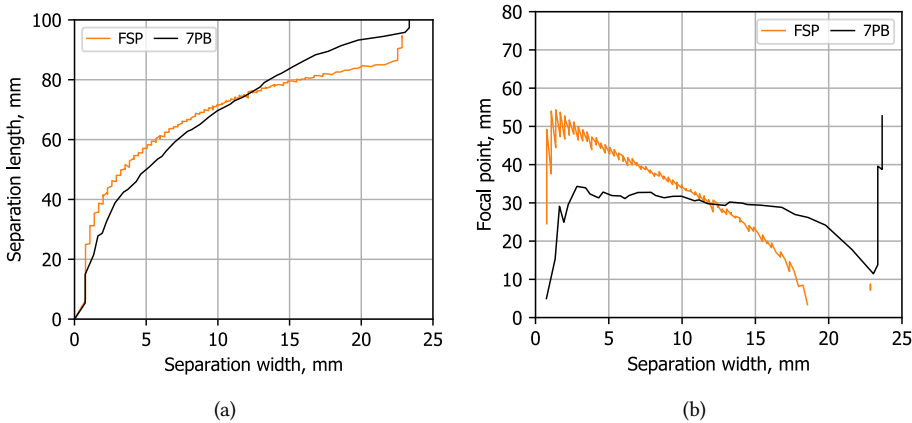


Figure 5.29: Comparing separation length and focal point change per separation width for the panel (FSP) and single-stringer model (7PB).

5.7 CONCLUSIONS

The numerical model of the single-stringer specimen in a seven-point bending configuration is designed to investigate the initiation, maximum load and shape that describes the skin-stringer separation response.

Out of 121 configurations, the model with the supports and loading points at the same distance from the edge and not too close to the stringer flange resulted in the lowest shape difference with respect to the critical region of the panel. Placing only the supports too far inwards causes a three-point bending-like configuration. Oppositely the loading points too far inwards cause local dimpling of the skin instead of a half-wave-like shape. The optimal configuration to match the deformation of the thick stringer panel investigated in chapter 4 has the following design variables: $S_X = 24$ mm, $S_Y = 36$ mm, $L_X = 70$ mm, $L_Y = 36$ mm, $W = 254$ mm, and $L = 140$ mm.

The separation response was predicted with numerical models that included cohesive elements. Five sets of cohesive properties, three of which used a superposed trilinear law to capture the R-curve effect, were investigated for these configurations. The interface properties had a minimal influence on the shape of separation but did affect the propagation speed. Removing the R-curve effect for mode II had a negligible impact on the separation response.

Four specimens were manufactured and tested. Load interruptions were used to track the change of the separated area with C-scans. The centre loadcell gave a good indication of initiation of skin-stringer separation as the load taken up by the centre support decreased. The C-scans also allow for the measurement of the separation length and width. The actual propagation shape changes from the elliptical approximation due to delamination migration. Migration, similar to what was observed in the coupon tests, goes into the skin when the separation front is parallel to the fibres. At the other end of the front, the separation growth was free.

Overall the trilinear interface model that uses the initiation properties of the unidirectional coupon tests and the propagation from the coupon tests of chapter 4 has the best correlation with the tests. This observation considered all metrics: initiation, maximum load and the actual separation response. Furthermore, the maximum load cell force was obtained around a separation width of 12-15 mm after which it plateaued and decreased. This indicated that the separation behaviour becomes unstable when the separation width is 50% of the total flange width.

The semi-analytical approach applied can be updated to include only the critical bending moment obtained from the single-stringer models/tests. With the updated numerical allowable initiation is predicted within 0.4% of initiation in the cohesive four-stringer panel model. The experimentally obtained allowable suggest separation starts even before that. The magnitude of the bending moment that triggers separation at initiation was comparable to the multi-stringer panel. Furthermore, the distribution of the bending and twisting moments along the stringer flange edge was equivalent. The normal compressive force was absent in the specimen due to the applied out-of-plane deformation, however, the effect on initiation can be neglected as the interface is zero-thickness.

The single-stringer specimen was capable to predict the separation shape of the post-buckled four-stringer panel. However, due to the changing postbuckling shape during propagation the focal length of the ellipse changes, which is related to the inflection points of the buckling wave, leading to a more circular separation shape as opposed to the seven-point bending configuration with almost fixed focal points. Nevertheless, above 50% of the flange width separation growth becomes unstable and the exact shape becomes less important.

6

A FOUR-POINT TWISTING CONFIGURATION TO CAPTURE SKIN-STRINGER SEPARATION

In a postbuckled panel with flexible stringers, skin-stringer separation can occur at the locations of highest twisting in between two buckling half-waves. A four-point twisting specimen loaded out-of-plane is developed to mimic the local postbuckling deformation. A study of the supports and loading point placement resulted in a design with the loading points close to the stringer flange. This design reproduces the local twisting moment and shear load distribution along the stringer flange. Additionally, a bending moment component not representative of the loading conditions in the panel was present at the edges. The four corners were physically clamped during the tests to prevent separation at the edges. The numerical models showed predominantly twisting separation, which an ellipse could describe. The effect of interface toughening (R-curve) modelled by a superposed trilinear cohesive law was minimal. The post-mortem interface from the tests also suggested that there were not many toughening mechanisms, no migration and only some matrix cracks. The tests did have a lot of variability and asymmetrical separation patterns. However, the postbuckling deformation and separation patterns did match between the numerical models and the tests. Lastly, the separation shape from the panel is captured around initiation but deviates as the interface damage tends to become more circular in an actual postbuckled panel. Still, it is expected that the single-stringer specimen captures the failure mechanisms in the panel at the start of separation, which drives the design the most.

6.1 INTRODUCTION

IN chapter 4 it was observed that a four-stringer panel with thin stringers can exhibit skin-stringer separation due to high skin twisting between the minima and maxima of a postbuckling half-wave. This chapter serves as a proposition of the use of a single-stringer specimen in the adaptive multi-point bending equipment to bridge the gap between the coupon and panel tests. Specifically, the Edge Crack Torsion[44, 45, 125–130], a coupon test to characterize mode III CSERR, is used for the design basis of this test.

Chapter goals

- **section 6.2:** Determine the design of the single-stringer specimen in four-point twisting to mimic the critical postbuckling conditions.
- **section 6.3:** Observe the initiation and propagation behavior of an out-of-plane loaded panel with different interface properties.
- **section 6.4:** Characterize the interface failure mechanisms in a postbuckling-like induced skin-stringer separation.
- **section 6.5:** Compare the finite element models to the experimental tests to illustrate the effectiveness of the models and to judge the material properties that are used.
- **section 6.6.1:** Compare the forces and moments along the edge of the single-stringer specimen to the four-stringer panel.
- **section 6.6.2:** Verify the ability of the single-stringer specimen to reproduce the skin-stringer separation behaviour by comparing it to the four-stringer panel.

6

6.2 SINGLE-STRINGER SPECIMEN DESIGN

The postbuckling deformation in the four-stringer panel model with thin stringers can lead to skin-stringer separation due to twisting of the skin. This has been observed in figure 4.20. The postbuckling shape around this critical location at an applied in-plane displacement of 3.3 mm is plotted in figure 6.1a. This critical area encompasses the region between the highest and lowest point of a buckling wave, and between the middle of the skin bay to the middle of the stringer itself. The dashed line indicates the edge of the stringer flange.

The optimum four-point twisting configuration, out of 194 combinations of S_X and S_Y , is plotted in figure 6.1b. With a matching legend for the out-of-plane displacement, a qualitative comparison can be made. It can be observed that the trend between the supports and loading points matches well with the four-stringer panel, whereas outside of this region, the approximation starts to diverge. The optimal configuration to approximate the postbuckling deformation, where RSS is the lowest as described in section 2.4, is defined by $S_X = 44$ mm and $S_Y = 50$ mm.

Originally, the optimum was found to be closer to the stringer edge, however, an initial numerical+experimental study [131] has shown that this lead to local peeling of the flange. This peeling is introduced by the direct out-of-plane loading close to the flange. This effect due to the free edge is not present in a multi-stringer panel, which means that the focus should be on the more global twisting deformation. Therefore a limit was set that a minimum distance of 20 mm to the edge should be used. The resulting optimum plot is shown in figure 6.2a.

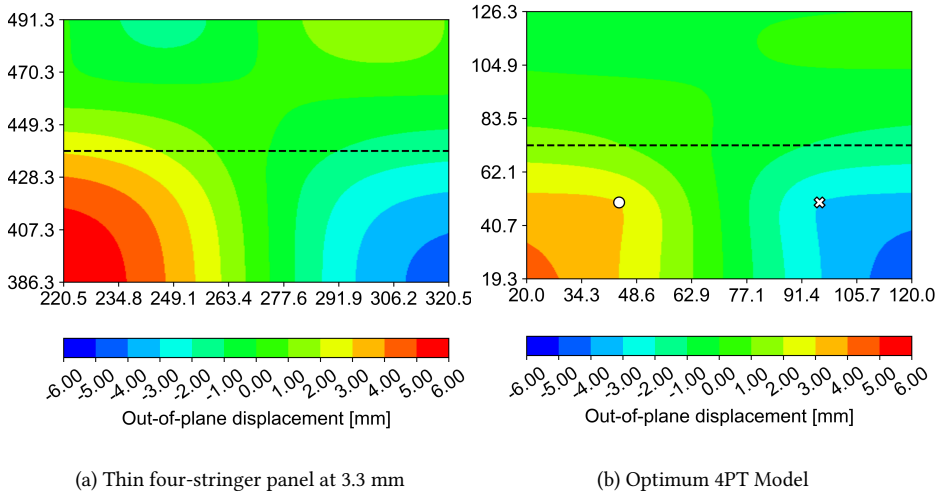


Figure 6.1: Comparing the out-of-plane deformation between a four-stringer panel and a single-stringer specimen in four-point twisting. The cross indicates the loading point and the circle is the support.

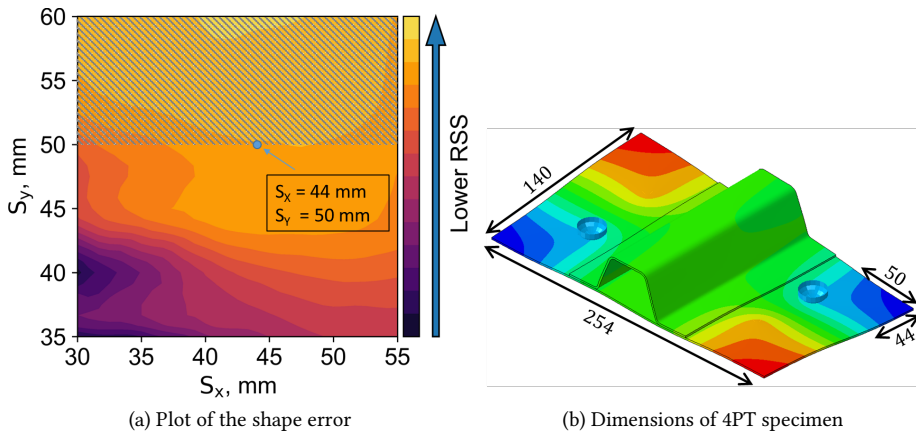


Figure 6.2: Optimum results of the four-point twisting design study.

6.3 PREDICTING SKIN-STRINGER SEPARATION THROUGH COHESIVE ZONE MODELLING

For the prediction of the skin-stringer separation response, a model with cohesive elements has been developed according to the method from section 2.3. In the finite element model, rigid body ties replace the cohesive elements for the first 10 mm at all four corners to not allow separation at the clamped location.

The force-displacement response is plotted in figure 6.3. The initiation can only be identified from the cohesive response as opposed to the seven-point bending configuration where the redistribution of the loads can be observed. The points of initiation as well as the maximum loads are collected in table 6.1. Due to the clamps, which are shown in figure 6.10, there is not a large load drop. The largest difference in the models is observed between Gclay and G0/GSS, where a higher mode II toughness leads to a higher initiation point. Although after the initial load drop, a minimal increase in compliance is observed.

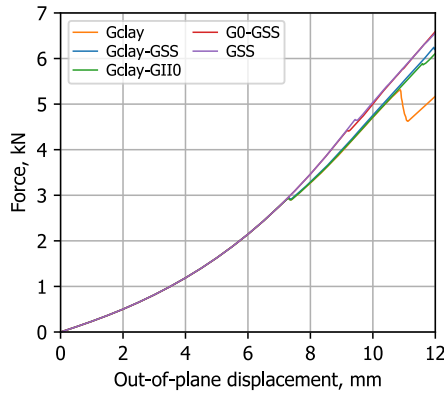


Figure 6.3: Force-displacement curves of the four-point twisting models.

Table 6.1: Initiation and max load of the four-point twisting models.

	Coh init. mm	Force init. kN	disp at max load mm	max load kN
Gclay	7.28	2.94	10.88	5.31
Gclay-GSS	7.30	2.95	>12.00	>6.22
Gclay-GII0	7.17	2.87	>12.00	>6.11
G0-GSS	9.00	4.28	>12.00	>6.59
GSS	9.42	4.65	>12.00	>6.56

The deformation and cohesive results, both for the primary and secondary set of cohesive elements, of 4PT Gclay-GSS are collected in figure 6.4. The deformation field only grows in magnitude, but the shape is not really affected by the separation growth. Separation starts suddenly between 7-7.5 mm, afterwards, it grows quite constant. Around 9 mm, the local bending induced by the loading point also introduces peeling separation. Although at 10 mm the separation width already spans 2/3rd of the flange, none of the elements of the secondary set of elements has failed due to its large processing zone.

An attempt was made to also approximate the separation fronts with ellipses, assuming again that the centre of the ellipse is the same distance from the stringer flange as the supports/loading points. The separation front with the elliptical approximation is shown in figure 6.5. When a single mode is present, separation does grow elliptically. As soon as the shearing failure interacts with peeling failure the shape of the separation front becomes more complex.

The separation width can still be used as a measure of separation size and is shown in figure 6.6. Due to the two different locations of initiation, the length is not a representative value anymore. The separation width can give an idea of the speed of separation growth as well as a way of comparing the FE models to the tests. Similar to the ENF tests, pure mode II separation tends to trigger a sudden rapid separation growth up to 5-7 mm separation widths. Separation triggered by peeling is more gradual.

A large difference is observed in figure 6.6 between using 0.65 and 1.19/1.29 for the (primary) mode II interface toughness. However, there was no effect of adding an R-curve effect, except for the last 5 mm of separation growth.

The mixed-mode conditions in which the energy is being released are shown in figure 6.7. Both initiation and evolution are pure mode II for the primary set of cohesive elements, except for the green region near the load point. For the secondary cohesive elements initiation still occurs mainly in mode II, but more and more mode I energy is present when the separation width reaches the total flange width.

Chronologically the four-point twisting tests were the first to be performed, during the development of the methodology. Only the Gclay properties were available and the outcome of just this model was used as input for the test preparations. It shows that following the order of the building block pyramid, starting with (structural) coupon tests is important.

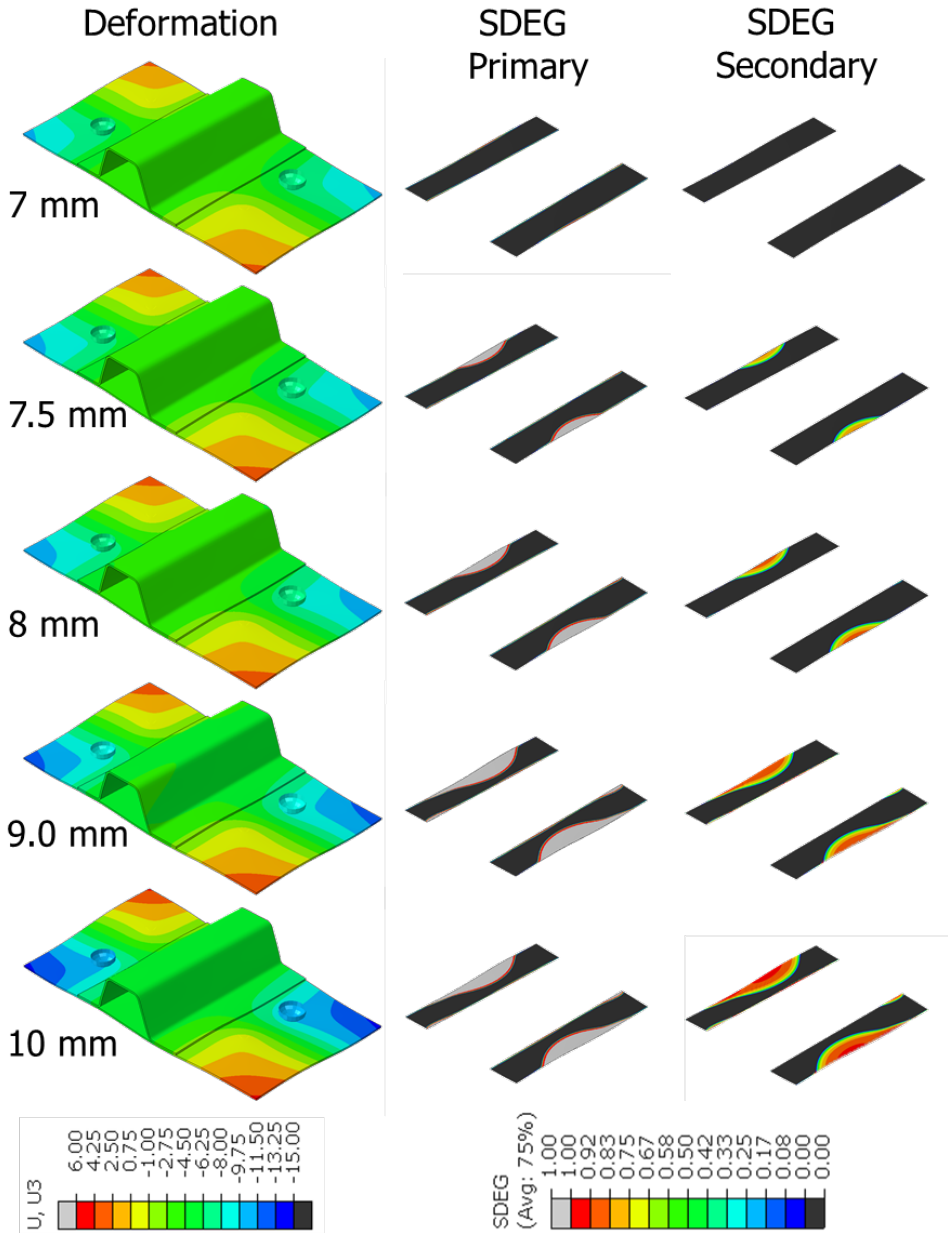


Figure 6.4: Out-of-plane displacement and interface damage of the 4PT specimen with Gclay-GSS properties at different applied displacements.

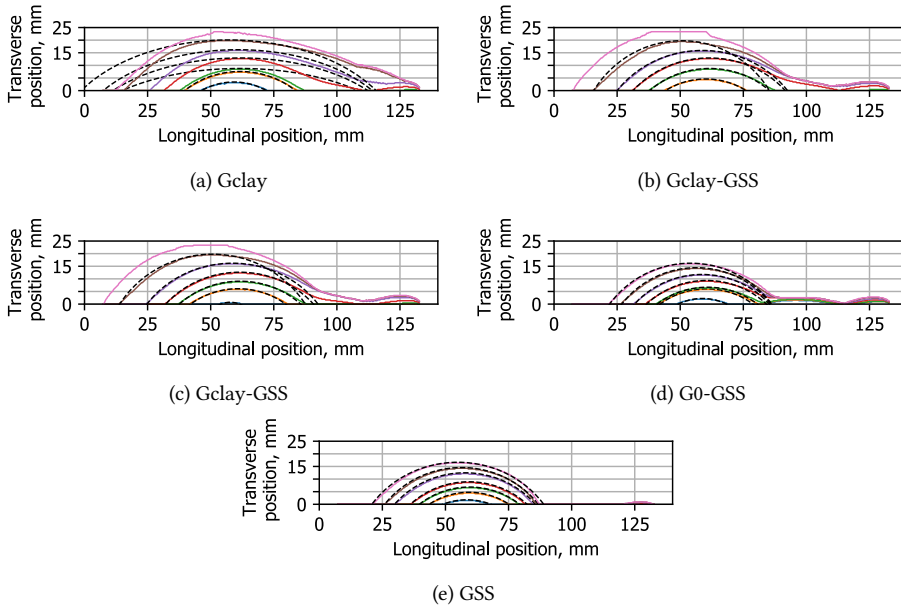


Figure 6.5: Actual separation fronts and elliptical approximations (dashed) of the four-point twisting models.

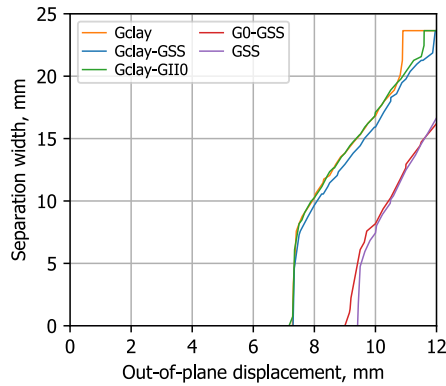


Figure 6.6: Separation width curves of the four-point twisting models.

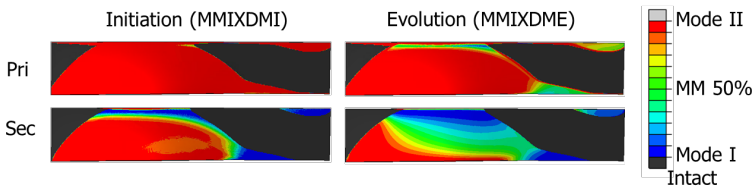


Figure 6.7: Mixed-mode conditions at initiation and full evolution for the pri(mary) Gclay and sec(ondary) GSS set of cohesive elements.

6.4 TESTING OF THE SKIN-STRINGER SEPARATION

In total 8 specimens are manufactured to be tested in this configuration. Specimen 4PT5 and 4PT6 are shown in figure 6.8. The first specimen (4PT1) is loaded in a single loading cycle until failure. Based on the results of 4PT1 and the FE analysis, it was decided to load the remaining specimens until the following displacement: 6 mm, 7 mm, and from 8 to 10 mm with steps of 0.25 mm, resulting in a total of 11 runs. In the end, the clamps at the corners are removed and a 12th load run allows to fully separate the stringer from the skin to investigate the fracture surface.

Specimens 4PT1-4PT4 were tested in early 2019, whereas specimens 4PT5-4PT8 were tested in 2021. For consistency, the exact same load pattern was used in all 7 incrementally loaded specimens. The differences and improvements between those two sets are C-scan capabilities (first the Rollerform probe of 5MHz and later the in-house built one as described in chapter 2), alignment of the specimen, shimming of the load points, and the digital image correlation setup.



Figure 6.8: Specimen 4PT5 and 4PT6.

The alignment and the setup for the four-point twisting configurations are illustrated in figure 6.9. The top bar is rotated to allow for anti-symmetric loading. This anti-symmetric loading creates the inflection deformation, which is portrayed in figure 6.10.

The force-displacement response of 4PT2 for each individual run is shown in figure 6.11a and for each load cell for the total response in figure 6.11b. The first drop in force occurs at an applied force of approximately 1 kN per loading point, or 2 kN of the total force, at an applied displacement of 6 mm. This drop was caused by local delaminations around the loading points. Due to the small misalignment, an upward load jump can be spotted around 7 mm. More frequent drops in force occur at a displacement of approximately 9 mm, which is a result of separation growth.

The same results for 4PT5 are shown in figure 6.11c,d. Due to the placement of 1mm thick steel shims at the loading points, the delaminations were much less severe and only present at very high loads. At each new run, the load returned to the previous maximum load for the same displacement, showing that the alignment works well. All specimens, collected in figure 6.11e, show most of the load drops between 9-10 mm displacement. The separation width is measured for all the separation fronts and plotted in figure 6.11f.

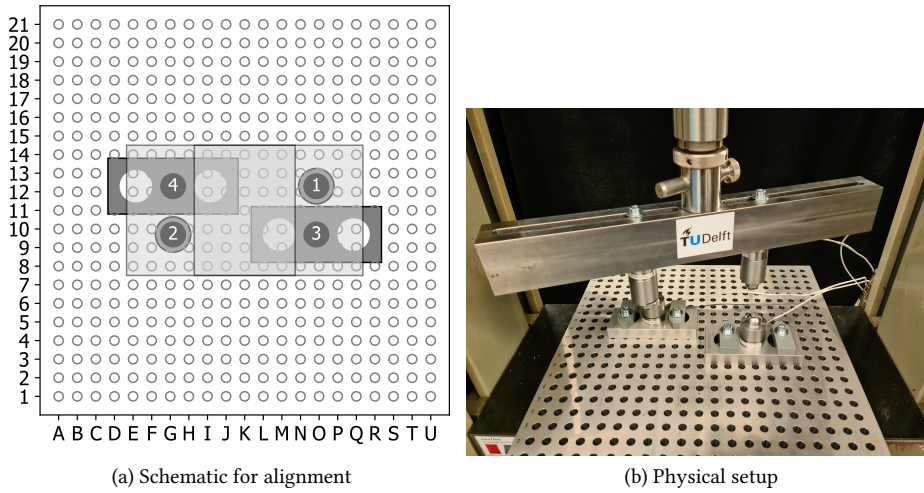


Figure 6.9: Layout of the four-point twisting configuration.

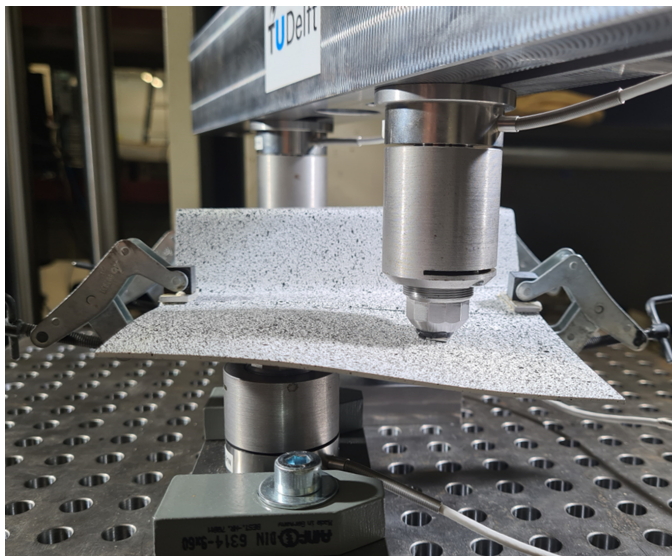
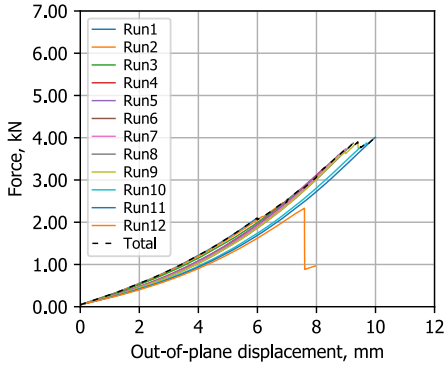
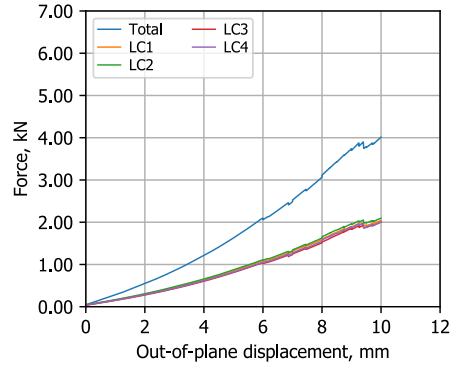


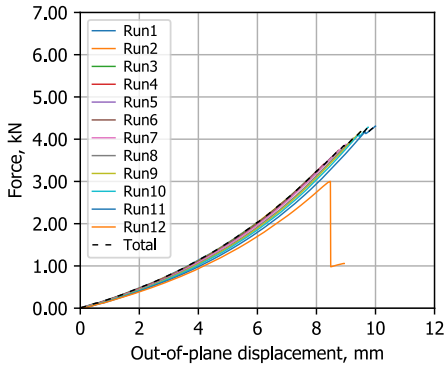
Figure 6.10: Sideview of the 4PT showing the skin inflection.



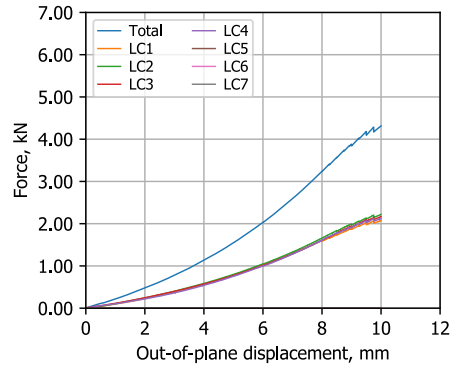
(a) 4PT2: loading runs



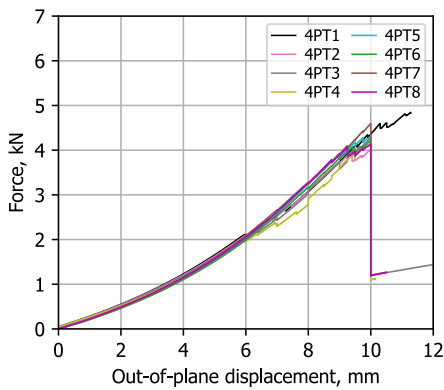
(b) 4PT2: load cell response



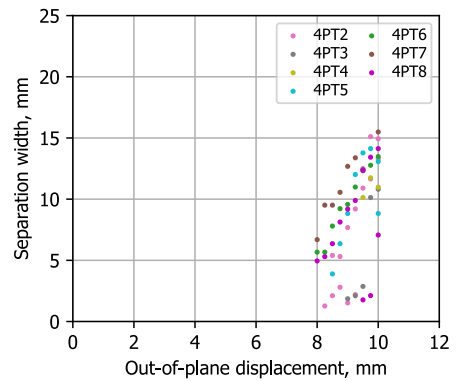
(c) 4PT5: loading runs



(d) 4PT5: load cell response



(e) All: force-displacement



(f) All: separation width

Figure 6.11: Results of the single-stringer tests in four-point twisting.

The raw C-scan images of 4PT2 and 4PT5 are shown in figure 6.12. The indentation delaminations, the four red/white circles close to the centre and the flange are much less severe for 4PT5 compared to 4PT2. The interface separation will be discussed in more detail, showing only the skin-stringer overlap region with post-processed data, using the red-blue colour scheme for consistency.

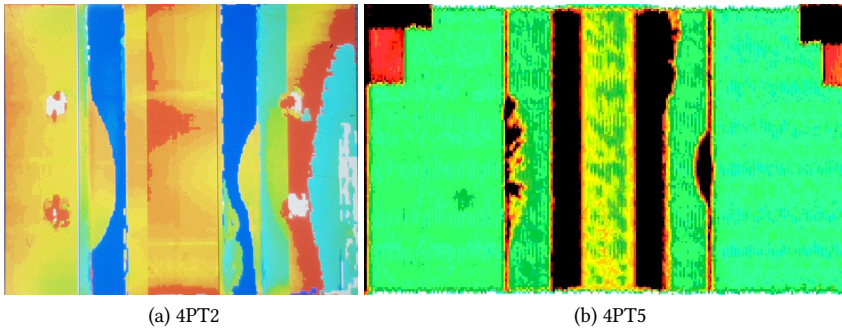


Figure 6.12: Raw 4PT C-scan results.

The separation states, pristine (Run0) and at the end of each run, are given for 4PT2 in figure 6.13. After run 5, 8.5 mm applied displacement, separation starts close to the loading points on one side. The separation shape is somewhat elliptical but extends all the way down to where the clamps are placed. Separation grows slowly asymmetrically until suddenly, the other side separates in a perfect ellipse. Simultaneously the inside of the stringer flange in the corner also starts to separate.

The C-scans of all specimens after run 7 (9 mm) and run 11 (10 mm) are collected in figure 6.14. Although the specimens do not show a lot of consistency, the same pattern can be recognized. Generally, it is asymmetrical with a combined twisting separation and load point-induced peeling at one side, often followed by the inside corner also separating at some point. On the other side, probably due to the increased compliance, the separation is purely twisting. Separation in the corner is accompanied by multiple delaminations through the thickness inside of the hat radius, shown in figure 6.15. This is an effect of the large out-of-plane deformation that tries to straighten the corner leading to the fracture, which can also be seen in T-stiffened panels[132–134].

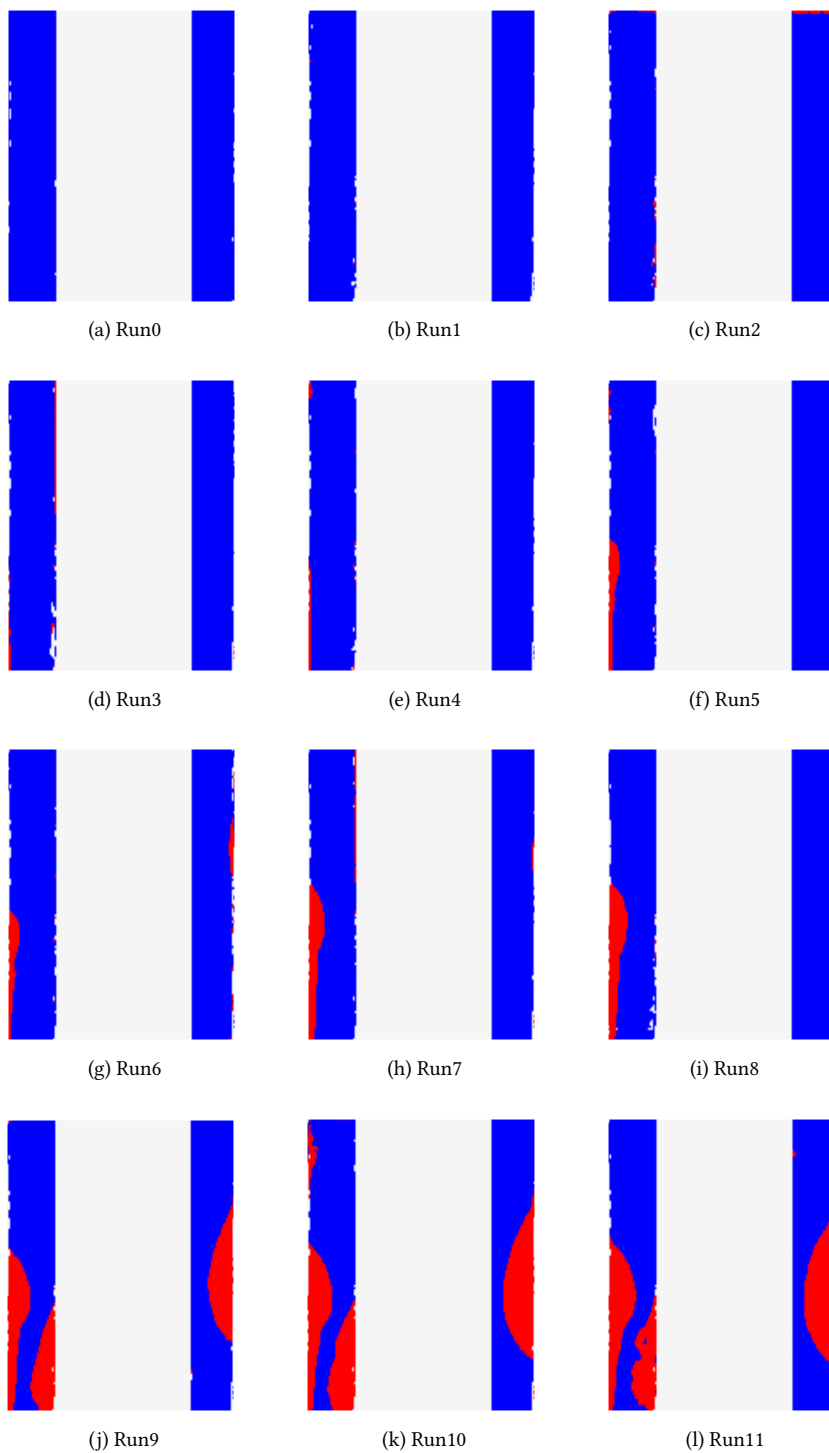


Figure 6.13: C-scan at the end of every run for 4PT2.

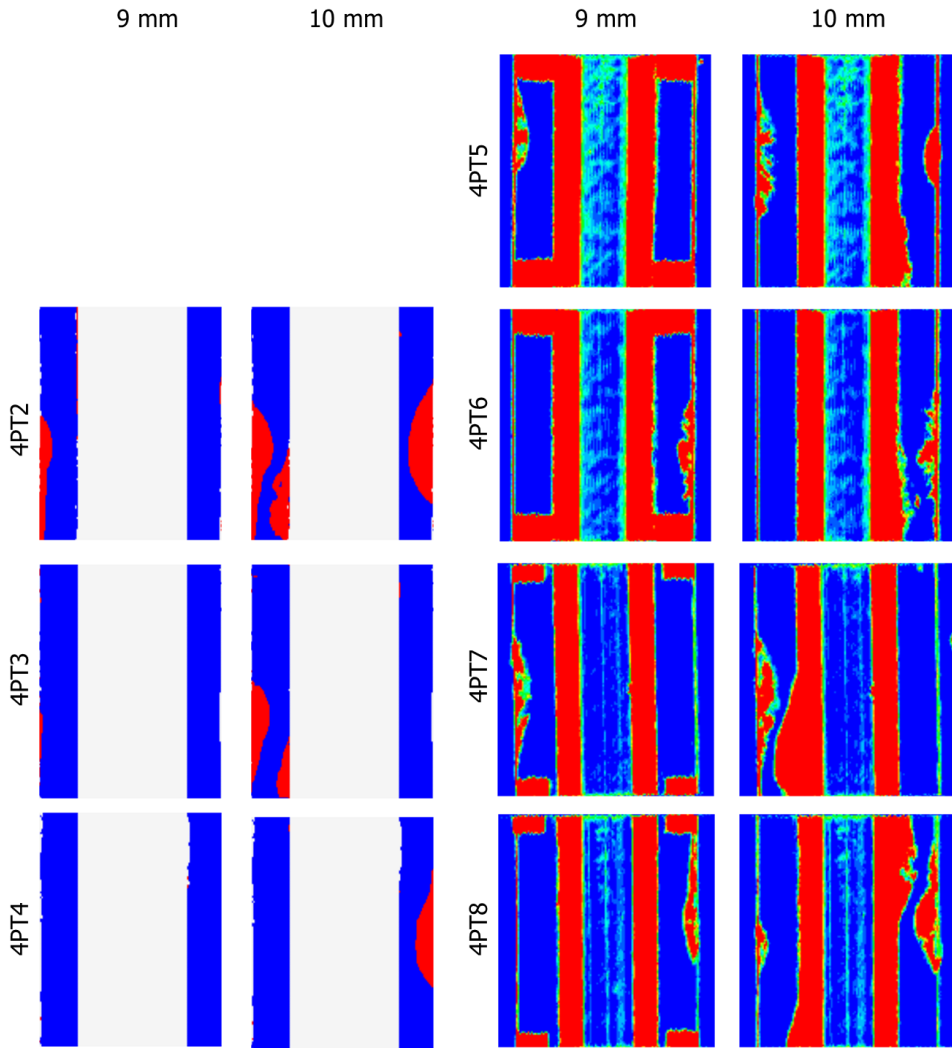


Figure 6.14: C-scans of all four-point twisting specimens.

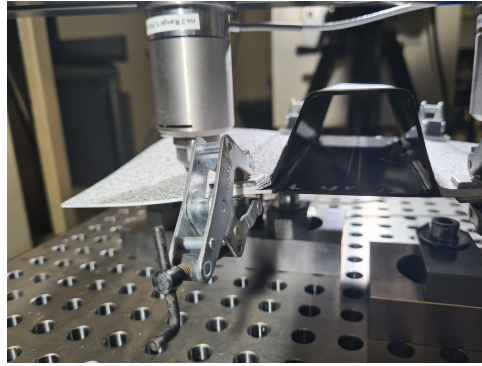


Figure 6.15: Fracture of hat radius in four-point twisting specimen near the clamped edge.

The interface can be investigated by performing a last run without clamps to fully separate the stringer from the skin. The right interface of 4PT2 is shown in figure 6.16 from the skin side where the fibres are oriented in -45 deg. The final separation front is highlighted. A second front can still be seen from the state at the end of run 9, figure 6.13j. Two things can be said with regard to these results. First of all, the separation propagates in jumps instead of continuous as was more common in the seven-point bending tests. Secondly, the fibre bridging and delamination migration is very limited. The surface itself is smooth, only some matrix cracking can be seen where the separation front is parallel to the fibres.

Reflecting back on the coupon tests and the seven-point bending tests, the smooth interface was slightly surprising. However, the large number of migration effects in the coupon tests of MMB and ENF was a result of the free edges that triggered delaminations. The smooth separation front also shows that likely the amount of R-curve effects in mode II/III loading is much smaller compared to more mode I loaded interfaces such as in the seven-point bending test, figure 5.19.

Looking at the literature, Canturri[135] observed migration when G_{III} , considering the fiber direction, is above 22% of the total critical strain energy release rate. In the work of De Morais et al.[136] migration was observed consistently to the 0//45 interface, which led to R-curve effects that were captured by the superposition of the cohesive elements. Adjacently, in the ECT tests of Czabaj, Audd et al[130, 137, 138] migration was only observed in 90//90 and 0//0 interfaces and not in the +45//−45; The mode III CSERR of the +45//−45 interface is 75% of the 0//0 interface. The interface delamination in the 4PT specimens (figure 6.14) is similar to the shape of the +45//−45 ECT specimen in figure 6.17[138].



Figure 6.16: Post-mortem interface seen from skin side of 4PT2.

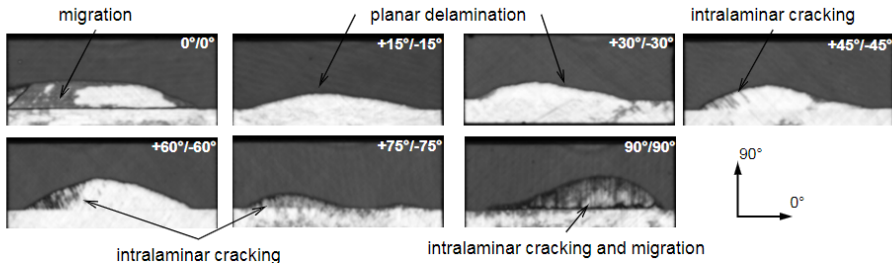


Figure 6.17: Interface delamination of ECT specimens[138].

6.5 NUMERICAL-EXPERIMENTAL COMPARISON

The section describes the comparison between the analyses performed on the single-stringer model and the eight 4PT tests.

It can be seen in figure 6.18a that the stiffness curves of the tests are nicely followed by the numerical models. The change in compliance is very limited in both the numerical models and the tests, which means that the force-displacement itself is not a good metric to compare the damaged state.

Figure 6.18b contains the separation width per applied displacement. The results of the tests fall between the models with a high and low mode II interface toughness. The reason for the difference is a combination of the asymmetrical growth and the fact that mode III separation has not been characterized. Nonetheless, the Gclay-GSS curve follows nicely the upper bound of the experimental results.

For a more one on one comparison, the out-of-plane displacement at 10 mm for Gclay-GSS and 4PT2 are given in figure 6.19. The out-of-plane deformation of the tests is almost indistinguishable from the numerical model. Similarly, the separation shape at this point is shown in figure 6.20. The shape of 4PT2 on the right flange is most similar to the finite element results. However, the left flange shows the other failure modes that are partially captured in the finite element model such as the peeling near the load point and the separating corner.

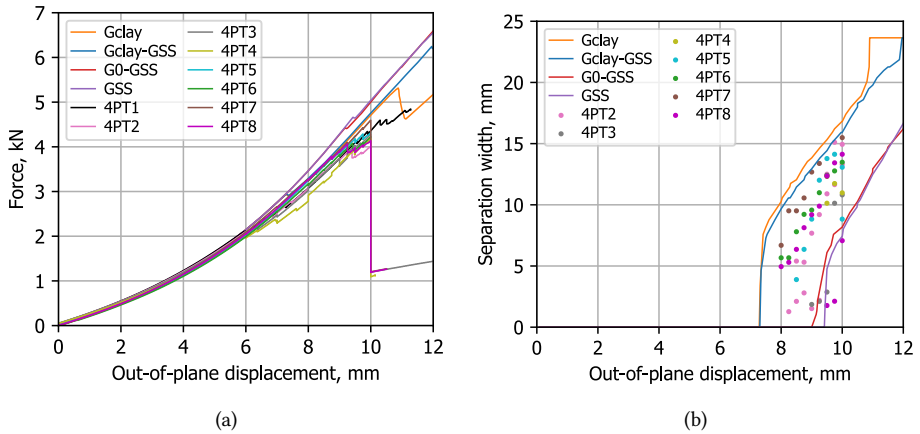


Figure 6.18: Comparing the four-point twisting experimental and numerical curves.

6

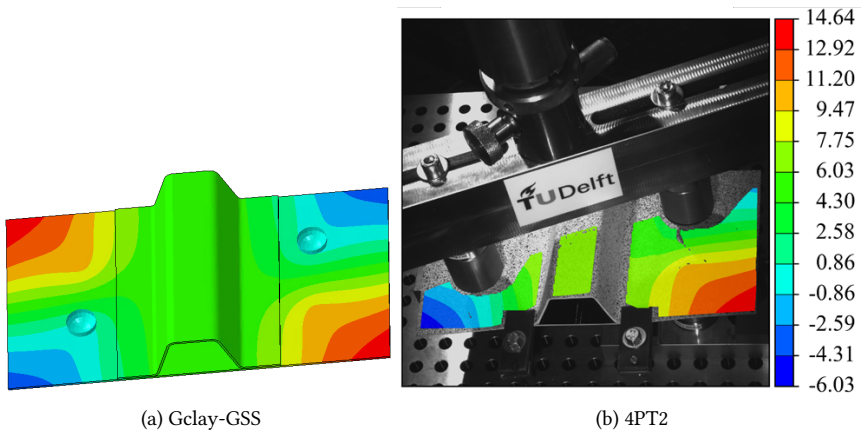


Figure 6.19: Comparing the four-point twisting experimental and numerical out-of-plane deformation at an applied displacement of 10 mm. The numerical model shares the legend with subfigure b.

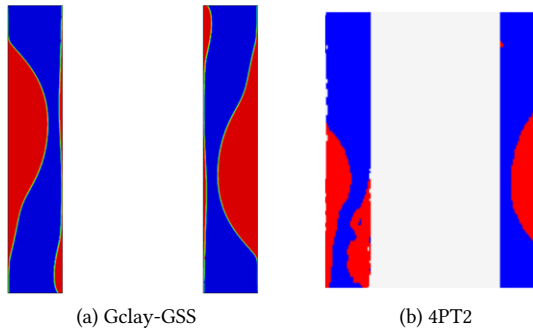


Figure 6.20: Comparing the four-point twisting experimental and numerical separation at an applied displacement of 10 mm.

6.6 INITIATION AND PROPAGATION OF SEPARATION IN THE FOUR-STRINGER PANEL

Although chapter 4 did not include a criterion for twisting, the approach of section 6.6.1 can be adapted for twisting. This makes it possible to predict initiation in the four-stringer panel based on a maximum twisting allowable. The bending/twisting moment and force distribution can be compared between the single-stringer specimen and the panel to show the similarities. Furthermore, the shape of separation in the 4PT specimens can be compared to the four-stringer panel model with the trilinear (Gclay-GSS) superposed cohesive elements.

6

6.6.1 INITIATION OF SEPARATION AND FORCE/MOMENT DISTRIBUTION

The twisting moment is extracted from the 4PT model and plotted against the applied force in figure 6.21a. The force at initiation from the experimental mean is used to approximate the critical twisting moments. These result in a numerical and experimental allowable for initiation due to twisting: 97.6 Nmm/mm and 108.4 Nmm/mm.

The maximum bending and twisting moments in the four-stringer panel with thin stringers without cohesive elements is shown in figure 6.21b. The bending moment plateaus around 35 Nmm/mm, but the twisting moment exceeds the allowable at 3.57 mm for FE, +8% with respect to the cohesive results of figure 4.20, and 4.0 mm for experimental.

The local bending/twisting moments and normal/shear forces in the skin-only elements closest to the skin-flange edge are shown in figure 6.22a,b.

From figure 6.22a it can be seen that the twisting moment in the panel around initiation is captured by the single-stringer specimen. Also the bending moment M_x is captured, and indeed zero at the inflection point. The bending moment M_y is high in magnitude close to the loading points, which leads to the mode I peeling, despite the increased distance from the flange.

The compressive load is not captured as can be seen in figure 6.21b, but as in the seven-point bending configuration, it is also assumed to not play a role for the initial part of the initiation. The magnitude of the shear force is negligible in the panel and the specimen.

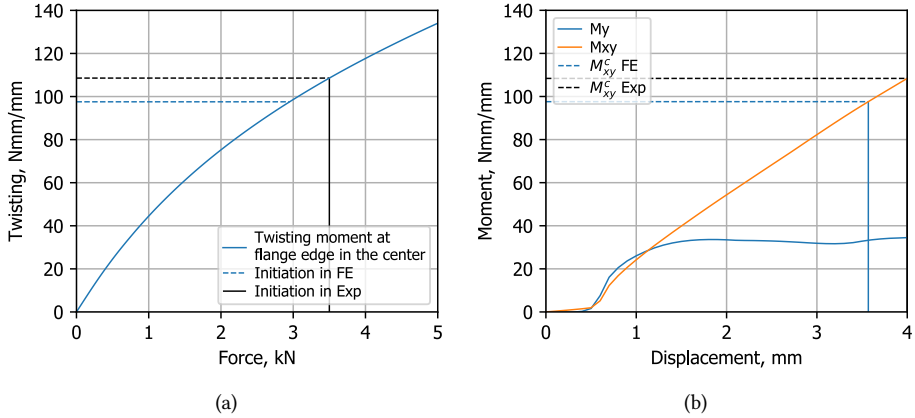


Figure 6.21: Maximum twisting moment along the skin-flange edge that can trigger initiation of skin-stringer separation.

6

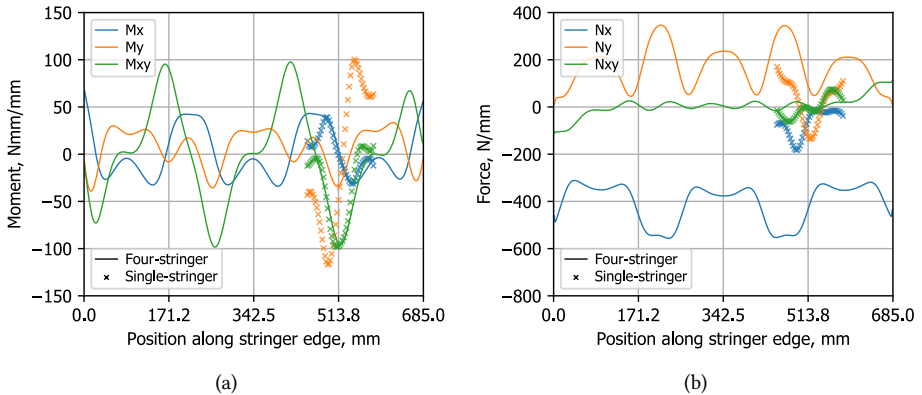


Figure 6.22: The bending/twisting moments and normal/shear forces in the skin along the edge of the four-stringer panel and the single-stringer in 4PT around the expected initiation load.

6.6.2 PROPAGATION AND SHAPE OF SEPARATION

The trilinear cohesive properties (Gclay-GSS) are implemented in the four-stringer panel with thin stringers. The postbuckling deformation and the approximation of the elliptical separation front at 3.4 mm are shown in figure 6.23. The distance of the centroid of the edge of 22.5 mm corresponds to the distance between the load/supports points and the edge in the 4PT configuration.

Separation occurs solely at the inflection point, as opposed to the maximum negative out-of-plane displacement in the thick-stringer panel, despite the higher deformation magnitude. As a result, pure mode II separation occurs for the primary interface, which agrees with the 4PT models.

The force-displacement response is presented in figure 6.24a. Initiation starts around 3.3 mm (440 kN) and the interface separation is fully developed at 3.5 mm (460 kN). With buckling occurring around 0.62 mm (100 kN) the load-carrying capabilities are 560% above buckling. After initiation, the panel can only withstand 6% higher displacement before full separation, even with the R-curve effects accounted for.

The approximated separation length and width of the elliptical fronts is presented in figure 6.24b. In both cases, initiation is abrupt, where the delamination jumps directly to 4 mm in separation width and 30 mm in length.

The actual separation fronts during propagation are shown in figure 6.25. The separation length is clearly larger in the single-stringer specimen than in the panel for the same separation widths. Furthermore, the local peeling around 125 mm in figure 6.25b due to the loading point is not present in figure 6.25a.

The separation behaviour in twisting tends to be more unstable compared to the bending case from chapter 5. In the thick-stringer panel, the displacement could be increased by 44% after initiation to reach full separation, as opposed to the 6% in the thin-stringer panel. This is even though, locally the magnitude of the bending in the thick-stringer panel is approximately the same as the twisting moment around initiation in the thin-stringer panel at 100 Nmm/mm. Even more so, the mode II CSERR is 2.5 times mode I for initiation. However, at a separation width of 15 mm, the separation length due to twisting is only 50 mm and in bending with its lower eccentricity is 80 mm. Hypothetically, if the thin-stringer panel would separate in bending with five half-waves, the separation length would be even longer than 80 mm as they are defined by the distance between the adjacent inflection points, which is higher for a smaller number of half-waves. The smaller separation length for twisting corresponds to a smaller total area releasing energy.

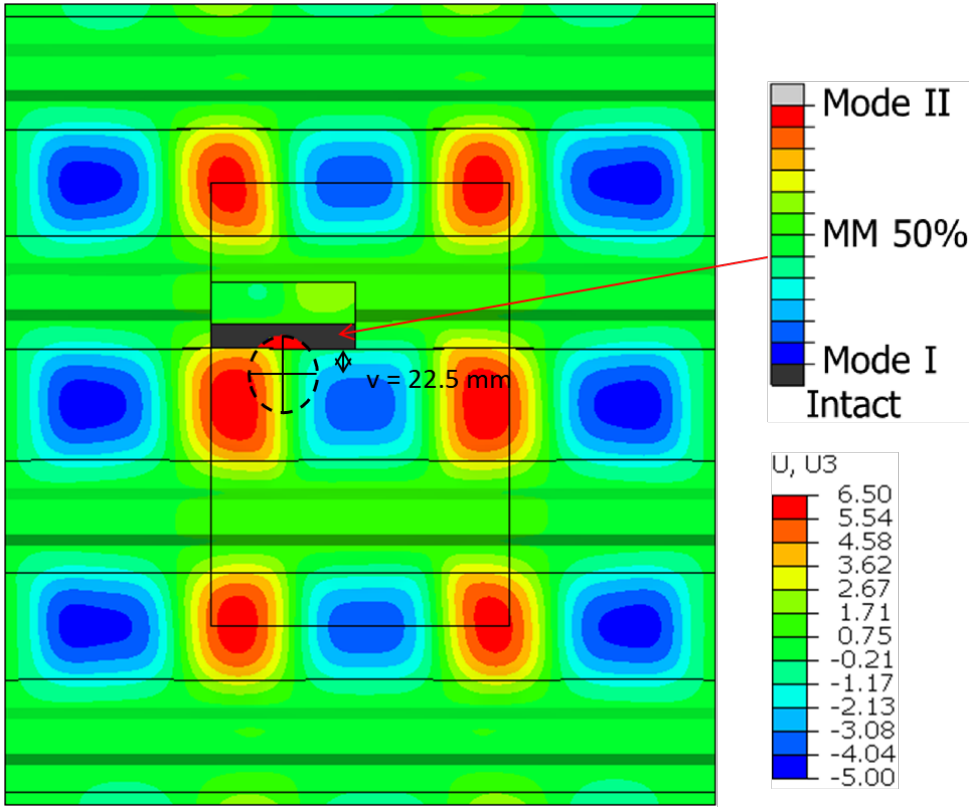


Figure 6.23: Buckling deformation and twisting induced separation in the panel at 3.4 mm. The elliptical centre is assumed at the same distance from the edge as the loading points in the 4PT configuration

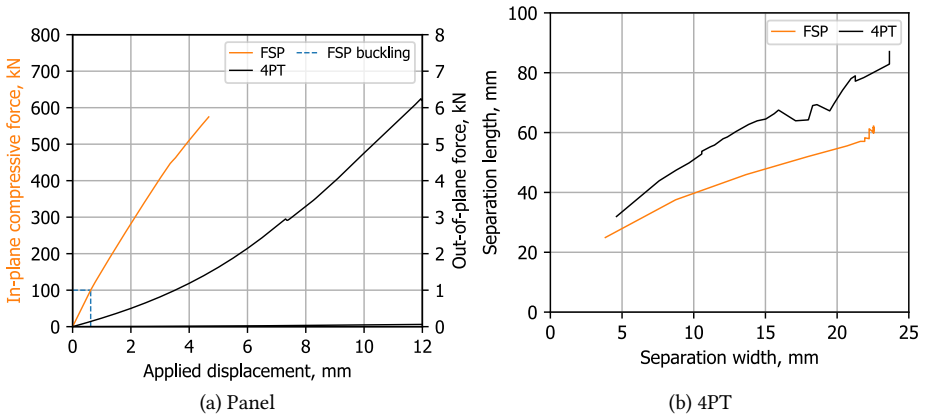


Figure 6.24: Comparing force and separation width versus applied displacement, with in-plane displacement for the panel (FSP) and out-of-plane for the single-stringer model (4PT).

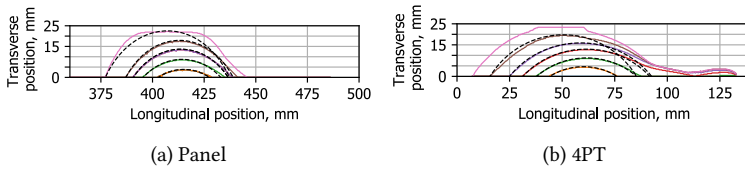


Figure 6.25: Elliptical approximation of skin-stringer separation front for thin-stringer panel specimen comparison.

6.7 CONCLUSIONS

A four-point twisting configuration is obtained that can reproduce the postbuckling deformation of a multi-stringer panel prone to fail due to high skin twisting. By comparing the out-of-plane displacement of the panel, it was observed that the loading points needed to be close to the edge of the stringer flange and the centre of the specimen. The final design is $S_X = 44$ mm, $S_Y = 50$ mm, $W = 254$ mm, and $L = 140$ mm.

A numerical model with cohesive elements with five different interface properties was considered, obtained from the coupon tests in chapter 3. The twisting deformation was captured throughout the entire separation process. Separation occurs primarily due to twisting in pure mode II/III. From the inside corner, there is also some mode I opening, which was limited by replacing the cohesive elements along the edge to model clamp-like conditions used during the tests. As long as separation is caused by pure shearing, the separation front follows an ellipse with the centre at the same distance from the edge as the loading points. The numerical models showed a difference between using 0.65 and 1.19/1.29 for the (primary) mode II/III interface toughness. However, there was no significant influence of a mode II R-curve effect.

Eight specimens were tested, seven with load interruptions between 8-10 mm every 0.25 to track the separation front. The separation started abruptly, common in shear-loaded interfaces, and propagated stably. Generally, separation occurred asymmetrically and often only in one of the two flanges. The primary failure mode was the shearing-induced separation, but secondary separation also occurred. The peeling load was more predominant than in the numerical models, as the clamps did not prohibit everything. The corner radius also fractured at high twisting deformation of around 10 mm.

Overall the four-point twisting specimens capture the out-of-plane deformation and show the twisting separation observed in the numerical models. The Gclay-GSS trilinear interface model best captured the test results but was on the conservative side. Variability is a lot higher for shear-loaded interfaces, and mode III properties are still not well known. Nonetheless, there will not be a sizeable R-curve effect as the post-mortem scans showed a clean interface without any delamination migration or fibre bridges.

By overlaying the forces and moment distribution along the flange edge, it was verified that the twisting moment that triggers separation was identical. Additionally, a bending moment was presented near the supports and loading points, similar to the ECT coupon tests. Using this twisting moment as an allowable for initiation predicted separation within 8% of the numerical model of the four-stringer panel with cohesive elements. It is expected

that considering purely delaminations, this is exceeded in a physical test of a four-stringer panel at 4.0 mm.

The 4PT models and some specimens capture the panel's initiation behaviour. In all cases, the initiation is sudden, with a jump of 5 mm in separation width. However, during propagation, the delamination shapes start to diverge, wherein the panel tends to become more circular, i.e. shorter length for the same width. It is a promising start for the characterization of twisting-induced separation in a postbuckled panel, but further development is still needed.

7

CONCLUSIONS AND RECOMMENDATIONS

Reducing the structural weight is crucial in aircraft to lower fuel consumption. Therefore, it is essential to understand the limits of the structures and their materials. Especially for composite materials, which allow weight reduction compared to metals but also have complex failure mechanisms. This thesis presents the methodology to study one of the possible failure mechanisms: postbuckling-induced delaminations that can lead to skin-stringer separation. During postbuckling conditions, high deformations lead to interface stresses, eventually causing the separation of the stringers. Hence, postbuckling is often not allowed in structures and thus their load-carrying potential is not fully utilized. The methodology follows a typical building block approach: coupon levels at the bottom for material characterization, element-level single-stringer specimens, and full panels. Different perspectives were used: analytical, numerical and experimental. The goal was to characterize skin-stringer separation induced by postbuckling conditions in large panels on the single-stringer level.

The main advantages of the methodology presented throughout this thesis can be summarized as follows:

- The interface properties can be characterized effectively as the coupons represent the larger structure and thus also consider delamination migration, fibre bridging and other toughening effects that might occur in the panel.
- The toughening behaviour of the interface leading to an R-curve effect is implemented in the numerical models through two superposed cohesive laws that operate independently and consider thermodynamic consistency.
- A semi-analytical framework can quickly assess possible skin-stringer separation due to bending using an energy-based criterion. The framework allows being updated to use a moment-based allowable, obtained from the single-stringer tests, to better predict initiation.

- The failure response can be studied using single-stringer specimens representing the multi-stringer panels. The single-stringer specimens are considerably less expensive to test due to their smaller size and complexity.
- The skin-stringer separation due to twisting and bending is investigated in two separate tests, the four-point twisting and seven-point bending respectively, allowing a better understanding of the dominant mode.
- Separation can be characterized and tracked more accurately in a single-stringer specimen subjected to out-of-plane loads as the deformation is controlled directly.
- The shape of the deformation of these single-stringer specimens is imposed by the location of the loading points, so it is not affected by geometrical imperfections or non-uniformity in the compressive loading distribution.

7.1 CONCLUSIONS

A methodology was presented following a building block pyramid, encompassing the coupon, single-stringer and panel level, using a combination of experimental tests and numerical models. The approach makes it possible to reduce the number of tests required in each consecutive level of the building block pyramid. The coupon tests provide material properties. A numerical model of a multi-stringer panel shows the possible postbuckling deformation. On the single-stringer level, skin-stringer separation due to postbuckling conditions can be investigated in detail. To develop the numerical models, a pre-processor was created in Python. The pre-processor allows various loading conditions, such as three-point bending, four-point twisting, seven-point bending, mixed-mode bending, and compression (for buckling), to be defined. A comprehensive guideline was presented encompassing the design, modelling, testing, and post-processing of a single-stringer specimen in an adaptive multi-point test configuration.

It was found that the coupons designed with an anti-symmetric layup captured delamination migrations accurately. It is necessary to consider mode I, II and mixed mode I/II to capture mode interactions if relationships such as the B-K relation are to be used. In mode I dominated tests, the toughening during propagation, also known as the R-curve effect, can be accurately identified. Increasing the mode II component reduced the amount of fibre bridging but induced delamination migration. The finite element implementation of the R-curve effect was adapted; the superposed element that considers the toughening effects only starts failing once the primary cohesive element has completely degraded. In this method, the fictitious mode II interface strength can be calculated directly from the thermodynamic consistency requirement in the superposed cohesive element. After these modifications, the numerical models of the mode I double cantilever beam specimen were able to predict the experimental response. The mixed-mode bending models did not capture the R-curve effects observed in the tests. A large processing zone led to the strain energy being released under (pure) mode I instead of the assumed mixed-mode condition, invalidating the mixed-mode bending R-curve results. Nevertheless, sets of functional interface properties were found, which can be implemented in the models higher up the building block pyramid.

A developed semi-analytical criterion can be used to estimate the initiation of separation in a postbuckled panel using a critical strain energy release rate allowable. The framework

only requires the bending moment perpendicular to the skin as the output of a finite element model. The failure index can be directly calculated along the entire length of the flange at each load stage. The criterion is sensitive only to the mesh size of the first element in the skin-flange overlap, allowing a coarse mesh everywhere else, keeping the model efficient. Two panel designs were analyzed: a thick-stringer panel with stringers twice the thickness of the skin and a thin-stringer panel with skin and stringer of equal thickness. The criterion predicted that failure would occur at the maximum out-of-plane displacement locations for the thick-stringer panel, while the thin-stringer panel did not exceed the allowable limit. Further analysis using a cohesive model of the thin-stringer panel revealed that separation occurs due to twisting between the half-waves.

The design of a single-stringer specimen in a seven-point bending configuration successfully recreated the postbuckling conditions of the thick-stringer panel. By matching the specimen's out-of-plane deformation to the panel's critical area, a set of support/load point variables can be established. A numerical model with cohesive elements in this optimal configuration can then be used to study the resulting skin-stringer separation behaviour. The R-curve had a limited effect on initiation or the separation shape but slowed down separation speed. Removing the mode II R-curve has a negligible effect on the response. In the experiments, separation migration occurred when the propagation path was orthogonal to the fibre direction. Furthermore, propagation speeds parallel to the fibre are higher due to the absence of R-curve effects. Propagation became unstable after a separation width of 50% of the total flange width. The numerical model with unidirectional initiation properties and the steady-state properties from the coupons with matching layup is the best predictor for the experimental tests. The maximum bending moment observed in the numerical model and the experimental tests can be used to establish a new allowable for the semi-analytical criterion. The new allowable bending moment was exceeded in the panel model with the criterion within 1% of the displacement in the cohesive model. The distribution of the bending and twisting moments in the numerical analyses of the panel also closely matched those in the single-stringer specimen model around initiation, demonstrating the power of the design strategy. The separation shape in the panel was correctly predicted until 13 mm, after which the separation shape in the panel deviates due to the change in postbuckling shape. The sizable separated area causes the inflection points to move closer to each. Nevertheless, tracking the shape becomes obsolete at this point, as separation tends to become unstable.

A four-point twisting configuration can be used to investigate skin-stringer separation due to twisting, which was present in the thin-stringer panel. Two supports and two loading points in opposing corners, similar to the edge crack torsion test, recreate the inflection shape. Separation caused by pure shearing results in an elliptical separation front. Typically in separation due to mode II+III, initiation is abrupt and, in these cases, asymmetrical. There are limited R-curve present, as seen in the smooth fracture interface, without any visible fibre bridging or migrations. The twisting moment measured in the skin of the specimens and numerical models can be used to predict initiation in the four-string panel, although the results show an 8% over-prediction. Initiation in the panel is sudden, with a distinct and nearly circular separation shape. While promising, further development is needed to increase accuracy in characterizing twisting-induced separation in a postbuckled panel.

An adaptive multipoint bending testing configuration based on a combination of numerical and experimental analyses provides a useful and accurate tool to study postbuckling behaviour in a variety of carbon fibre-reinforced composite panel structures. Using numerical and experimental tests for the lower levels of the building block pyramid while assessing the larger specimens predominantly numerically results in a process that is both accurate and efficient.

7.2 OBSERVATIONS THROUGHOUT THE BUILDING BLOCK PYRAMID

Observations that were made throughout this entire thesis are listed below. A comparison is made between the single-stringer and multi-stringer panel, the coupon and the single-stringer specimen, and between bending and twisting separation. Understanding the similarities and differences because of assumptions and simplifications will aid in translating the results from one level of the pyramid to the next. Furthermore, noticing the difference between twisting-induced and bending-induced separation will give a better understanding of postbuckling-induced separation.

Between the single- and multi-stringer panels:

- Out-of-plane deformations were equivalent, leading to also the same bending/twisting moment distribution.
- The separation shape was similar up to 50% of the flange width.
- Initiation was abrupt for the panel and specimens that showed separation due to twisting.
- The force acting perpendicular to the skin flange in the panel is not captured by the single-stringer specimen.
- The normal compressive force is absent in the single-stringer specimens.

From the list above, it can be seen that the adaptive multi-point test configuration works well for reproducing the postbuckling shape and, consequently, the moment distribution and the separation shape. Hence, the bending/twisting moment observed in the single-stringer specimen can be a good indicator for initiation in the multi-stringer panel. Due to the lack of a normal compressive force in the single-stringer specimen, the deformation shape does not change when a large part of the stringer has separated. The absence of the perpendicular force needs to be investigated further.

Between the coupon tests and the single-stringer specimens:

- The mixed-mode bending showed the same delamination migration pattern as the seven-point bending single-stringer specimen in the centre of the specimen.
- The mode II R-curve did not affect the response in coupon or single-stringer specimens.
- Initiation was abrupt in the ENF mode II test, similar to the mode III four-point twisting test.
- Migrations were more severe in the coupons due to the free edge.

In a coupon specimen that is designed to reflect the layup of the single-stringer specimen, the migration effects are also captured. Therefore, the interface properties obtained from these tests can directly be applied to the models of the single-stringer specimens. However, migration was too severe in the coupon tests due to the free edges and these should be limited to make it even more representative of the larger specimens. The mode II R-curve did not influence the single-stringer specimen, thus it would not be directly necessary to characterize this on coupon level. Note that this might only pertain to the designs of this thesis.

Between bending and twisting separation:

- Separation shape was elliptical and became more circular while propagating in both cases.
- For the same separation width, the length was shorter for twisting separation, leading to a smaller total separated area.
- Twisting separation propagates faster despite the higher interface toughness.

Separations tend to grow from an elliptical to a circular shape for bending and twisting, which can be used to define the growth path. The shorter separation length in the twisting separation compensates for the larger interface toughness, as the total energy released at full separation is a combination of the separated area and strain energy release rate. As also observed on the coupons and single-stringer specimens, initiation due to twisting often occurs as a sudden jump, whereas it is more gradual for bending. Therefore a higher margin of safety is required for panels that are twisting-critical as opposed to bending-critical panels.

7.3 RECOMMENDATIONS FOR FUTURE RESEARCH

The methodology encompasses three levels of the building block pyramid to study the skin-stringer separation at different complexities and sizes. In order for the methodology and its tests to become a standard in the development of composite structures more work is required. Some recommendations for improvement of the method or future research are mentioned here.

Currently, a simple optimisation is used to design the single-stringer specimen in the adaptive multi-point test equipment. A proper optimization technique, such as gradient descent method, should be used such that more variables can be considered. For example, such additional variables could be specimen length and width or additional supports/load points.

Investigate a six-point bending test configuration. The central support point in seven-point bending allows for stable separation propagation. Consequently, this makes the separation shape less representative when the separation front moves towards the centre. In a multi-stringer panel, when the stringer fully separates, a tunnel between is formed, extending from one bay to the next [7]. By removing this central support, the same can be achieved. This has been tested, showing promising initial results. The requirement of the corner supports to be on the inflection points should stay.

With the methodology, it is now easy to investigate the effect of different postbuckling shapes within the same panel design. The hypothesis is that for a shorter half-wave, a

smaller area will be separated before the skin starts to tunnel. The inflection points will be closer to each other, which defines the maximum length of the elliptical separation shape. This does not mean that it will be more critical due to the different moment distributions. These cases can be explored through the seven-point bending tests with different specimen lengths and positions for the supports and load points. Furthermore, shear-loaded postbuckling[139] which can also trigger separation can be investigated further using the seven-point bending test[79].

Implement other failure mechanisms in the models, such as Hashin or the subroutine CompDam[140]. To implement the latter, the mesher needs to be updated as the method requires fibre-aligned meshes to model matrix cracks and delamination migrations.

Further use of the test configurations would be very interesting for the development of structural health monitoring tools[77], fatigue characterization of skin-stringer separation[141] possibly in combination with (indentation) damages[142], or characterizing novel toughening mechanisms such as Z-pins[143, 144], stitching[145–147] or carbon nanotubes[148].

BIBLIOGRAPHY

REFERENCES

- [1] J. H. Starnes and M. Rouse. Postbuckling and failure characteristics of selected flat rectangular graphite-epoxy plates loaded in compression. In *AIAA/ASME/ASCE/AHS/ASC Structures, Structural Dynamics and Materials Conference*, pages 423–434, 1981.
- [2] J. Action, U. Palliyaguru, W. Jackson, and J. Zalameda. Testing of a multi-stringer post-buckled panel with incremental damage detection. In *AIAA Scitech 2020 Forum*, 1480, 2020.
- [3] J. Action and F. A. Leone. Progressive damage analysis of a multi-stringer post-buckled panel. In *AIAA Scitech 2020 Forum*, 1481, 2020.
- [4] C. Bisagni. Progressive delamination analysis of stiffened composite panels in post-buckling. In *Collection of Technical Papers - AIAA/ASME/ASCE/AHS/ASC Structures, Structural Dynamics and Materials Conference*, volume 10, pages 6972–6983, 2006.
- [5] A. Raimondo and C. Bisagni. Fatigue analysis of a post-buckled composite single-stringer specimen taking into account the local stress ratio. *Composites Part B: Engineering*, 193:108000, 2020.
- [6] E. Greenhalgh, C. Meeks, A. Clarke, and J. Thatcher. The effect of defects on the performance of post-buckled CFRP stringer-stiffened panels. *Composites Part A: Applied Science and Manufacturing*, 34(7):623–633, 2003.
- [7] K.S. van Dooren, B.H.A.H. Tijs, J.E.A. Waleson, and C. Bisagni. Skin-stringer separation in post-buckling of butt-joint stiffened thermoplastic composite panels. *Composite Structures*, 304(2):116294, 2023.
- [8] K. N. Anyfantis and N. G. Tsouvalis. Post buckling progressive failure analysis of composite laminated stiffened panels. *Applied Composite Materials*, 19(3-4):219–236, 2012.
- [9] C. G. Dávila, P. P. Camanho, and C. A. Rose. Failure criteria for FRP laminates. *Journal of Composite Materials*, 39(4):323–345, 2005.
- [10] C. J.R. Kosztowny and A. M. Waas. Postbuckling response of unitized stiffened textile composite panels: Experiments. *International Journal of Non-Linear Mechanics*, 137:103814, 2021.

- [11] P. P. Camanho, C. G. Dávila, S. T. Pinho, L. Iannucci, and P. Robinson. Prediction of in situ strengths and matrix cracking in composites under transverse tension and in-plane shear. *Composites Part A: Applied Science and Manufacturing*, 37(2):165–176, 2006.
- [12] S. Lauterbach, A. C. Orifici, W. Wagner, C. Balzani, H. Abramovich, and R. Thomson. Damage sensitivity of axially loaded stringer-stiffened curved CFRP panels. *Composites Science and Technology*, 70(2):240–248, 2010.
- [13] J. E. Yetman, A. J. Sobey, J. I.R. Blake, and R. A. Shenoi. Investigation into skin stiffener debonding of top-hat stiffened composite structures. *Composite Structures*, 132:1168–1181, 2015.
- [14] S. N. Masood, R. Vishakh, S. R. Viswamurthy, K. M. Gaddikeri, and I. Sridhar. Influence of stiffener configuration on post-buckled response of composite panels with impact damages. *Composite Structures*, 194:433–444, 2018.
- [15] Department of Defense. *Composite Materials Handbook: Volume 3*, volume MIL-HDBK-17-3F. 2002.
- [16] C. Bisagni and R. Vescovini. Analytical formulation for local buckling and post-buckling analysis of stiffened laminated panels. *Thin-Walled Structures*, 47(3):318–334, 2009.
- [17] G. A. O. Davies and R. Olsson. Impact on composite structures. *The Aeronautical Journal*, pages 541–563, 2004.
- [18] S. Wanthal, J. Schaefer, B. Justusson, I. Hyder, S. Engelstad, and C. Rose. Verification and validation process for progressive damage and failure analysis methods in the NASA advanced composites consortium. In *American Society for Composites 32nd Technical Conference*, pages 3020–3035, West Lafayette, IN, 2017.
- [19] S. Zhu, J. Yan, Z. Chen, M. Tong, and Y. Wang. Effect of the stiffener stiffness on the buckling and post-buckling behavior of stiffened composite panels - Experimental investigation. *Composite Structures*, 120:334–345, 2015.
- [20] S. N. Masood, S. R. Viswamurthy, and K. M. Gaddikeri. Composites airframe panel design for post-buckling – An experimental investigation. *Composite Structures*, 241:112104, 2020.
- [21] C. Bisagni and C. G. Dávila. Experimental investigation of the postbuckling response and collapse of a single-stringer specimen. *Composite Structures*, 108(1):493–503, 2014.
- [22] P. J. Minguet and T. K. O’Brien. Analysis of test methods for characterizing skin/stringer debonding failures in reinforced composite panels. *Composite Materials: Testing and Design: Twelfth Volume*, 1274:105–124, 1996.
- [23] Dassault Systemes. Abaqus 2019 Manual , 2019.

- [24] E. Cosentino and P. M. Weaver. Approximate nonlinear analysis method for debonding of skin/stringer composite assemblies. *AIAA Journal*, 46(5):1144–1159, 2008.
- [25] J. G. Williams. On the calculation of energy release rates for cracked laminates. *International Journal of Fracture*, 36:101–119, 1988.
- [26] J. C. F. N. Van Rijn. Failure criterion for the skin-stiffener interface in composite aircraft panels. *Technical report*, NLR-TP-98264, 1998.
- [27] J. C. F. N. Van Rijn. Design guidelines for the prevention of skin-stiffener debonding in composite aircraft panels. *Technical report*, NLR-TP-2000-355, 2000.
- [28] J. C. F. N. Van Rijn and J. F. M. Wiggendaad. A seven-point bending test to determine the strength of the skin-stiffener interface in composite aircraft panels. *Technical report*, NLR-TP-2000-044, 2000.
- [29] S. Hühne, J. Reinoso, E. Jansen, and R. Rolfes. A two-way loose coupling procedure for investigating the buckling and damage behaviour of stiffened composite panels. *Composite Structures*, 136:513–525, 2016.
- [30] E. Pietropaoli and A. Riccio. A global/local finite element approach for predicting interlaminar and intralaminar damage evolution in composite stiffened panels under compressive load. *Applied Composite Materials*, 18(2):113–125, 2011.
- [31] J. Reinoso, A. Blázquez, A. Estefani, F. París, and J. Cañas. A composite runout specimen subjected to tension-compression loading conditions: Experimental and global-local finite element analysis. *Composite Structures*, 101:274–289, 2013.
- [32] M. H. Nagaraj, M. Petrolo, and E. Carrera. A global–local approach for progressive damage analysis of fiber-reinforced composite laminates. *Thin-Walled Structures*, 169:108343, 2021.
- [33] M. Akterskaia, E. Jansen, and R. Rolfes. Progressive failure analysis of stiffened composite panels using a two-way loose coupling approach including intralaminar failure and debonding. In *2018 AIAA/ASCE/AHS/ASC Structures, Structural Dynamics, and Materials Conference*, page 0735, 2018.
- [34] M. Akterskaia, E. Jansen, S. R. Hallett, P. M. Weaver, and R. Rolfes. Progressive failure analysis using global-local coupling including intralaminar failure and debonding. *AIAA Journal*, 57(7):3078–3089, 2019.
- [35] M. Akterskaia, P. P. Camanho, E. Jansen, A. Arteiro, and R. Rolfes. Progressive delamination analysis through two-way global-local coupling approach preserving energy dissipation for single-mode and mixed-mode loading. *Composite Structures*, 223:110892, 2019.
- [36] T. E. Tay. Characterization and analysis of delamination fracture in composites: An overview of developments from 1990 to 2001. *Applied Mechanics Reviews*, 56(1):1–32, 2003.

- [37] T. K. O'Brien. Fracture mechanics of composite delamination. *Composites*, pages 241–245, 2001.
- [38] J. Brunet, B. Pierrat, and P. Badel. Review of current advances in the mechanical description and quantification of aortic dissection mechanisms. *IEEE Reviews in Biomedical Engineering*, 14:240–255, 2021.
- [39] Standard Test Method for Mode I Interlaminar Fracture Toughness of Unidirectional Fiber-Reinforced Polymer Matrix Composites. *ASTM International*, D552813, 2013.
- [40] Standard Test Method for Determination of the Mode II Interlaminar Fracture Toughness of Unidirectional Fiber-Reinforced Polymer Matrix Composites. *ASTM International*, D7905/D7905M19, 2019.
- [41] Standard Test Method for Mixed Mode I-Mode II Interlaminar Fracture Toughness of Unidirectional Fiber Reinforced Polymer Matrix Composites. *ASTM International*, D6671/D6671M19, 2019.
- [42] J. R. Reeder and J. H. Crews. Mixed-mode bending method for delamination testing. *AIAA Journal*, 28(7):1270–1276, 1990.
- [43] M. L. Benzeggagh and M. Kenane. Measurement of mixed-mode delamination fracture toughness of unidirectional glass/epoxy composites with mixed-mode bending apparatus. *Composites Science and Technology*, 56(4):439–449, 1996.
- [44] J. G. Ratcliffe. Characterization of the Edge Crack Torsion (ECT) test for mode III fracture toughness measurement of laminated composites. *Technical report*, NASA/TM-2004-213269, 2004.
- [45] A. B. de Morais and A. B. Pereira. Mode III interlaminar fracture of carbon/epoxy laminates using a four-point bending plate test. *Composites Part A: Applied Science and Manufacturing*, 40(11):1741–1746, 2009.
- [46] D. J. Nicholls and J. P. Gallagher. Determination of GIC in angle ply composites using a cantilever beam test method. *Journal of Reinforced Plastics and Composites*, 2(1):2–17, 1983.
- [47] P. Robinson and D. Q. Song. A modified DCB specimen for mode I testing of multidirectional laminates. *Journal of Composite Materials*, 26(11):1554–1577, 1992.
- [48] B. F. Sørensen and T. K. Jacobsen. Large-scale bridging in composites: R-curves and bridging laws. *Composites Part A: Applied Science and Manufacturing*, 29(11):1443–1451, 1998.
- [49] N. S. Choi, A. J. Kinloch, and J. G. Williams. Delamination fracture of multidirectional carbon-fiber/epoxy composites under mode I, mode II and mixed-mode I/II loading. *Journal of Composite Materials*, 33(1):73–100, 1999.
- [50] B. W. Kim and A. H. Mayer. Influence of fiber direction and mixed-mode ration on delamination fracture toughness of carbon/epoxy laminates. *Composites Science and Technology*, 63(5):695–713, 2003.

- [51] J. Andersons and M. König. Dependence of fracture toughness of composite laminates on interface ply orientations and delamination growth direction. *Composites Science and Technology*, 64(13-14):2139–2152, 2004.
- [52] A. B. Pereira and A. B. de Morais. Mode I interlaminar fracture of carbon/epoxy multidirectional laminates. *Composites Science and Technology*, 64(13-14):2261–2270, 2004.
- [53] A. B. Pereira, A. B. De Morais, M. F.S.F. De Moura, and A. G. Magalhães. Mode I interlaminar fracture of woven glass/epoxy multidirectional laminates. *Composites Part A: Applied Science and Manufacturing*, 36(8):1119–1127, 2005.
- [54] A. B. Pereira and A. B. de Morais. Mixed mode I + II interlaminar fracture of glass/epoxy multidirectional laminates - Part 2: Experiments. *Composites Science and Technology*, 66(13):1896–1902, 2006.
- [55] A. B. de Morais and A. B. Pereira. Application of the effective crack method to mode I and mode II interlaminar fracture of carbon/epoxy unidirectional laminates. *Composites Part A: Applied Science and Manufacturing*, 38(3):785–794, 2007.
- [56] C. G. Dávila, C. A. Rose, and P. P. Camanho. A procedure for superposing linear cohesive laws to represent multiple damage mechanisms in the fracture of composites. *International Journal of Fracture*, 158(2):211–223, 2009.
- [57] Y. Gong, B. Zhang, L. Zhao, J. Zhang, N. Hu, and C. Zhang. R-curve behaviour of the mixed-mode I/II delamination in carbon/epoxy laminates with unidirectional and multidirectional interfaces. *Composite Structures*, 223:110949, 2019.
- [58] S. M. Jensen, M. J. Martos, B. L.V. Bak, and E. Lindgaard. Formulation of a mixed-mode multilinear cohesive zone law in an interface finite element for modelling delamination with R-curve effects. *Composite Structures*, 216:477–486, 2019.
- [59] M. Heidari-Rarani and A.R. Ghasemi. Appropriate shape of cohesive zone model for delamination propagation in ENF specimens with R-curve effects. *Theoretical and Applied Fracture Mechanics*, 90:174–181, 2017.
- [60] A.B. de Morais. Evaluation of a trilinear traction-separation law for mode II delamination using the effective crack method. *Composites Part A: Applied Science and Manufacturing*, 121:74–83, 2019.
- [61] N. Pichler, M. Herráez, and J. Botsis. Mixed-mode fracture response of anti-symmetric laminates: Experiments and modelling. *Composites Part B: Engineering*, 197:108089, 2020.
- [62] A. Raimondo, I. Urcelay Oca, and C. Bisagni. Influence of interface ply orientation on delamination growth in composite laminates. *Journal of Composite Materials*, 55(27):3955–3972, 2021.

- [63] Y. Gong, X. Chen, W. Li, L. Zhao, J. Tao, J. Zhang, and N. Hu. Delamination in carbon fiber epoxy DCB laminates with different stacking sequences: R-curve behavior and bridging traction-separation relation. *Composite Structures*, 262:113605, 2021.
- [64] F. Pereira, N. Dourado, J. J. L. Morais, and M. F. S. F. de Moura. A new method for the identification of cohesive laws under pure loading modes. *Engineering Fracture Mechanics*, 271:108594, 2022.
- [65] B.H.A.H. Tijs, S. Abdel-Monsef, J. Renart, A. Turon, and C. Bisagni. Characterization and analysis of the interlaminar behavior of thermoplastic composites considering fiber bridging and R-curve effects. *Composites Part A: Applied Science and Manufacturing*, 162:107101, 2022.
- [66] G. Alfano. On the influence of the shape of the interface law on the application of cohesive-zone models. *Composites Science and Technology*, 66(6):723–730, 2006.
- [67] S. Yin, Y. Gong, W. Li, L. Zhao, J. Zhang, and N. Hu. A novel four-linear cohesive law for the delamination simulation in composite DCB laminates. *Composites Part B: Engineering*, 180:107526, 2020.
- [68] C. Bisagni, R. Vescovini, and C. G. Dávila. Single-stringer compression specimen for the assessment of damage tolerance of postbuckled structures. *Journal of Aircraft*, 48(2):495–502, 2011.
- [69] V. K. Goyal, A. Pennington, and J. Action. Damage Prediction of Post-Buckled Composite Single Hat-Stringer Panel Subject to Compression After Impact. In *AIAA SciTech Forum 2022*, 2394, 2022.
- [70] M. A. Sadiq. The post-buckling response of stiffened CFRP panels using a single-stringer compression specimen (SSCS): a numerical investigation. *Computational Methods and Experimental Measurements XVII*, 59:507–516, 2015.
- [71] C. Bisagni, R. Vescovini, and C. G. Davila. Assessment of the damage tolerance of post-buckled hat-stiffened panels using single stringer specimens. In *51st AIAA/ASME/ASCE/AHS/ASC Structures, Structural Dynamics, and Materials Conference*, 2696, 2010.
- [72] V. K. Goyal, A. Pennington, and J. Action. Progressive damage failure analysis of post-buckled composite single-stringer panel with Teflon inserts. In *American Society for Composites 36th Conference*, pages 429–443, 2021.
- [73] D. C. Jegley. Experimental behavior of fatigued single stiffener PRSEUS specimens. *Technical report*, NASA/TM–2009-215955, 2009.
- [74] D. C. Jegley, A. Velicki, and D. Hansen. Structural efficiency of stitched rod-stiffened composite panels with stiffener crippling. In *49th AIAA/ASME/ASCE/AHS/ASC Structures, Structural Dynamics, and Materials Conference*, 2170, 2008.

- [75] N. R. Kolanu, G. Raju, and M. Ramji. Experimental and numerical studies on the buckling and post-buckling behavior of single blade-stiffened CFRP panels. *Composite Structures*, 196:135–154, 2018.
- [76] N. R. Kolanu, G. Raju, and M. Ramji. A unified numerical approach for the simulation of intra and inter laminar damage evolution in stiffened CFRP panels under compression. *Composites Part B: Engineering*, 190:107931, 2020.
- [77] A. A. R. Broer, G. Galanopoulos, D. Zarouchas, T. Loutas, and R. Benedictus. Damage diagnostics of a composite single-stiffener panel under fatigue loading utilizing SHM data fusion. In *European Workshop on Structural Health Monitoring - Special Collection of 2020 Papers*, volume 127, pages 616–625, 2021.
- [78] A. Raimondo, J. Paz Mendez, and C. Bisagni. Experimental study on post-buckled composite single-stringer specimens with initial delamination under fatigue loads. In *American Society for Composites, Thirty-Sixth Technical Conference*, pages 418–428, 2021.
- [79] J. Bertolini, B. Castanié, J. J. Barrau, J. P. Navarro, and C. Petiot. Multi-level experimental and numerical analysis of composite stiffener debonding. Part 2: Element and panel level. *Composite Structures*, 90(4):392–403, 2009.
- [80] C. J. R. Kosztowny, C. G. Dávila, K. Song, C. A. Rose, and W. Jackson. Experimental and numerical analysis of skin-stiffener separation using a seven-point bend configuration. In *ALAA Scitech Forum 2019, 1767*, 2019.
- [81] W. Seneviratne, V. Saseendran, M. Shafie, and J. Tomblin. Skin/stringer interface damage characterization of stiffened composite structures. In *ASC 36th Technical Conference*, pages 2505–2527, 2021.
- [82] C. G. Dávila, F. A. Leone, K. Song, J. G. Ratcliffe, and C. A. Rose. Material characterization for the analysis of skin/stiffener separation. In *American Society for Composites 33rd technical conference, 128*, 2017.
- [83] Q. Ye and P. Chen. Prediction of the cohesive strength for numerically simulating composite delamination via CZM-based FEM. *Composites Part B: Engineering*, 42(5):1076–1083, 2011.
- [84] J. Bertolini, B. Castanié, J. J. Barrau, and J. P. Navarro. An experimental and numerical study on omega stringer debonding. *Composite Structures*, 86(1-3):233–242, 2008.
- [85] Ronald Krueger, Michael K Cvitkovich, T. Kevin O'Brien, and Pierre J. Minguet. Testing and Analysis of Composite Skin/Stringer Debonding Under Multi-Axial Loading. *Composite Materials*, 34(15):1263–1300, 2000.
- [86] J. Bertolini, B. Castanié, J. J. Barrau, and J. P. Navarro. Multi-level experimental and numerical analysis of composite stiffener debonding. Part 1: Non-specific specimen level. *Composite Structures*, 90(4):381–391, 2009.

- [87] F. A. Leone, K. Song, W. Johnston, C. A. Rose, W. C. Jackson, C. J. Kosztowny, and C. G. Dávila. Test/analysis correlation of damage states in post-buckled stiffened validation building block specimens. In *American Society for Composites 34th Technical Conference*, page 28086, 2019.
- [88] B. P. H. van den Akker, M. V. Donadon, R. Loendersloot, L. A. de Oliveira, and M. A. Arbelo. The influence of hygrothermal aging on the fatigue behavior and residual strength of post-buckled co-bonded stiffened panels subjected to compressive loading. *Composites Part B: Engineering*, 194:108023, 2020.
- [89] C. Meeks, E. Greenhalgh, and B. G. Falzon. Stiffener debonding mechanisms in post-buckled CFRP aerospace panels. *Composites Part A: Applied Science and Manufacturing*, 36(7):934–946, 2005.
- [90] R. Vescovini, C. G. Dávila, and C. Bisagni. Simplified models for the study of post-buckled hat-stiffened composite panels. *Technical report*, NASA/TM–2012-217336, 2012.
- [91] K. A. Stevens, R. Ricci, and G. A. O. Davies. Buckling and postbuckling of composite structures. *Composites*, 26:189–199, 1995.
- [92] A. C. Orifici, R. S. Thomson, I. Herszberg, T. Weller, R. Degenhardt, and J. Bayandor. An analysis methodology for failure in postbuckling skin-stiffener interfaces. *Composite Structures*, 86(1-3):186–193, 2008.
- [93] R. Vescovini, C. G. Dávila, and C. Bisagni. Failure analysis of composite multi-stringer panels using simplified models. *Composites Part B: Engineering*, 45(1):939–951, 2013.
- [94] B. Wang, X. Chen, W. Wang, J. Yang, and R. Zhang. Post-buckling failure analysis of composite stiffened panels considering the mode III fracture. *Journal of Composite Materials*, 56(20):3099–3111, 2022.
- [95] C. G. Dávila, P. P. Camanho, and A. Turon. Effective simulation of delamination in aeronautical structures using shells and cohesive elements. *Journal of Aircraft*, 45(2):663–672, 2008.
- [96] R. Krueger. The virtual crack closure technique: history, approach, and applications. *Applied Mechanics Reviews*, 57(2):109–143, 2004.
- [97] G. E. Mabson, N. V. De Carvalho, and R. Krueger. VCCT with progressive nodal release for simulating mixed-mode delamination: formulation, algorithmic improvements and implications. In *American Society for Composites 33rd Technical Conference*, 137, 2018.
- [98] P. P. Camanho, C. G. Dávila, and M. F. De Moura. Numerical simulation of mixed-mode progressive delamination in composite materials. *Composite Materials*, 37(16):1415–1438, 7 2003.
- [99] J. C. Brewer and P. A. Lagace. Quadratic stress criterion for initiation of delamination. *Journal of Composite Materials*, 22(12):1141–1155, 1988.

- [100] P. W. Harper and S. R. Hallett. Cohesive zone length in numerical simulations of composite delamination. *Engineering Fracture Mechanics*, 75(16):4774–4792, 2008.
- [101] A. Turon, C. G. Dávila, P. P. Camanho, and J. Costa. An engineering solution for mesh size effects in the simulation of delamination using cohesive zone models. *Engineering Fracture Mechanics*, 74(10):1665–1682, 2007.
- [102] S. B. Clay and P. M. Knuth. Experimental results of quasi-static testing for calibration and validation of composite progressive damage analysis methods:. *Journal of Composite Materials*, 51(10):1333–1353, 2016.
- [103] J. J. Polaha, B. D. Davidson, R. C. Hudson, and A. Pieracci. Effects of mode ratio, ply orientation and precracking on the delamination toughness of a laminated composite. *Journal of Reinforced Plastics and Composites*, 15(2):141–173, 1996.
- [104] L. A. Carlsson, J. W. Gillespie, and B. R. Trethewey. Mode II interlaminar fracture of graphite/epoxy and graphite/PEEK. *Journal of Reinforced Plastics and Composites*, 5(3):170–187, 1986.
- [105] Y. Wang and J. G. Williams. Corrections for mode II fracture toughness specimens of composites materials. *Composites Science and Technology*, 43(3):251–256, 1992.
- [106] A. Turon, E. V. González, C. Sarrado, G. Guillaumet, and P. Maimí. Accurate simulation of delamination under mixed-mode loading using a cohesive model with a mode-dependent penalty stiffness. *Composite Structures*, 184:506–511, 2018.
- [107] P. W. Harper, L. Sun, and S. R. Hallett. A study on the influence of cohesive zone interface element strength parameters on mixed mode behaviour. *Composites Part A: Applied Science and Manufacturing*, 43(4):722–734, 2012.
- [108] V. Q. Bui, L. Iannucci, P. Robinson, and S. T. Pinho. A coupled mixed-mode delamination model for laminated composites. *Journal of Composite Materials*, 45(16):1717–1729, 2011.
- [109] A. Turon, P. P. Camanho, J. Costa, and C. G. Dávila. A damage model for the simulation of delamination in advanced composites under variable-mode loading. *Mechanics of Materials*, 38(11):1072–1089, 2006.
- [110] A. Turon, P. P. Camanho, J. Costa, and J. Renart. Accurate simulation of delamination growth under mixed-mode loading using cohesive elements: Definition of interlaminar strengths and elastic stiffness. *Composite Structures*, 92(8):1857–1864, 2010.
- [111] C. Sarrado, A. Turon, J. Renart, and I. Urresti. Assessment of energy dissipation during mixed-mode delamination growth using cohesive zone models. *Composites Part A: Applied Science and Manufacturing*, 43(11):2128–2136, 2012.
- [112] M. F. S. F. de Moura, J. P. M. Gonçalves, and F. G. A. Silva. A new energy based mixed-mode cohesive zone model. *International Journal of Solids and Structures*, 102-103:112–119, 2016.

- [113] J. G. Williams. The fracture mechanics of delamination tests. *Journal of Strain Analysis*, 24(4):207–214, 1989.
- [114] D. Cohen and M. W Hyer. Calculation of skin-stiffener interface stresses in stiffened composite panels. *Technical report*, NASA-CR-184682, 1987.
- [115] I. L. Paris, R. Krueger, and T. K. O'Brien. Effect of assumed damage and location on delamination onset for skin-stiffener debonding. *Journal of the American Helicopter Society*, 49(4):501–507, 2004.
- [116] F. A. Leone, K. Song, C. A. Rose, and W. C. Jackson. Progressive damage analysis of post-buckled stiffened panels under static compressive loading. In *AIAA Scitech 2020 Forum*, 1479, 2020.
- [117] C. Canturri, E. S. Greenhalgh, S. T. Pinho, and J. Ankersen. Delamination growth directionality and the subsequent migration processes - The key to damage tolerant design. *Composites Part A: Applied Science and Manufacturing*, 54:79–87, 2013.
- [118] L. Carreras, E. Lindgaard, J. Renart, B. L.V. Bak, and A. Turon. An evaluation of mode-decomposed energy release rates for arbitrarily shaped delamination fronts using cohesive elements. *Computer Methods in Applied Mechanics and Engineering*, 347:218–237, 2019.
- [119] J. W. H. Yap, M. L. Scott, R. S. Thomson, and D. Hachenberg. The analysis of skin-to-stiffener debonding in composite aerospace structures. *Composite Structures*, 57(1-4):425–435, 2002.
- [120] J. W. H. Yap, R. S. Thomson, M. L. Scott, and D. Hachenberg. Influence of post-buckling behaviour of composite stiffened panels on the damage criticality. *Composite Structures*, 66:197–206, 2004.
- [121] A. Raimondo and A. Riccio. Inter-laminar and intra-laminar damage evolution in composite panels with skin-stringer debonding under compression. *Composites Part B: Engineering*, 94:139–151, 2016.
- [122] A. Raimondo, S. A. Doesburg, and C. Bisagni. Numerical study of quasi-static and fatigue delamination growth in a post-buckled composite stiffened panel. *Composites Part B: Engineering*, 182:107589, 2020.
- [123] G. Galanopoulos, D. Milanoski, A. Broer, D. Zarouchas, and T. Loutas. Health monitoring of aerospace structures utilizing novel health indicators extracted from complex strain and acoustic emission data. *Sensors*, 21(17):5701, 2021.
- [124] A. Broer, G. Galanopoulos, R. Benedictus, T. Loutas, and D. Zarouchas. Fusion-based damage diagnostics for stiffened composite panels. *Structural Health Monitoring*, 21(2), 2022.
- [125] S. M. Lee. An edge crack torsion method for mode III delamination fracture testing. *Journal of Composites Technology & Research*, 15(3):193–201, 1993.

- [126] J. Li, S. M. Lee, E. W. Lee, and T. K. O'Brien. Evaluation of the Edge Crack Torsion (ECT) test for mode III interlaminar fracture toughness of laminated composites. *Journal of Composites Technology and Research*, 19(3):174–183, 1997.
- [127] D. Zhao and Y. Wang. Mode III fracture behavior of laminated composite with edge crack in torsion. *Theoretical and Applied Fracture Mechanics*, 29:109–123, 1998.
- [128] G. Browning, L. A. Carlsson, and J. G. Ratcliffe. Modification of the edge crack torsion specimen for mode III delamination testing. Part II-experimental study. *Journal of Composite Materials*, 45(25):2633–2640, 2011.
- [129] R. Marat-Mendes and M. de Freitas. Characterisation of the edge crack torsion (ECT) test for the measurement of the mode III interlaminar fracture toughness. *Engineering Fracture Mechanics*, 76(18):2799–2809, 2009.
- [130] C. Audd, B. D. Davidson, J. G. Ratcliffe, and M. W. Czabaj. Reexamination of the edge crack torsion test for determining the mode III delamination toughness of laminated composites. *Engineering Fracture Mechanics*, 215:138–150, 2019.
- [131] L. J. Kootte and C. Bisagni. A methodology to investigate skin-stringer separation in postbuckled composite stiffened panels. In *AIAA Scitech 2020 Forum*, 477, volume 1 PartF, 2020.
- [132] J. Chen and D. Fox. Numerical investigation into multi-delamination failure of composite T-piece specimens under mixed mode loading using a modified cohesive model. *Composite Structures*, 94(6):2010–2016, 2012.
- [133] Z. Sápi, R. Butler, and A. Rhead. High fidelity analysis to predict failure in T-joints. *Composite Structures*, 225:111143, 2019.
- [134] D. Qiao. *Manufacturing and Mechanical Testing of Composite T-Joints with Carbon Nanotube Interleaves*. PhD thesis, Delft University of Technology, Delft, 2022.
- [135] C. Canturri, E. S. Greenhalgh, and S. T. Pinho. The relationship between mixed-mode II/III delamination and delamination migration in composite laminates. *Composites Science and Technology*, 105:102–109, 2014.
- [136] A. B. De Morais, A. B. Pereira, and M. F.S.F. De Moura. Mode III interlaminar fracture of carbon/epoxy laminates using the Six-Point Edge Crack Torsion (6ECT). *Composites Part A: Applied Science and Manufacturing*, 42(11):1793–1799, 2011.
- [137] M. W. Czabaj, J. G. Ratcliffe, and B. D. Davidson. Observation of intralaminar cracking in the edge crack torsion specimen. *Engineering Fracture Mechanics*, 120:1–14, 2014.
- [138] M. W. Czabaj, B. D. Davidson, and J. G. Ratcliffe. A modified edge crack torsion test for measurement of mode III fracture toughness of laminated tape composites. In *American Society for Composites 31st Technical Conference*, 1706, 2016.
- [139] R. Krueger, J. G. Ratcliffe, and P. J. Minguet. Panel stiffener debonding analysis using a shell/3D modeling technique. *Composites Science and Technology*, 69(14):2352–2362, 2009.

- [140] F. Leone, M. Ramnath, I. Hyder, S. Wanthal, J. D Schaefer, and G. Mabson. Benchmarking mixed mode matrix failure in progressive damage and failure analysis methods. In *American Society for Composites 33rd Technical Conference*, 72, 2018.
- [141] C. G. Dávila and J. Ratcliffe. Quasi-static and fatigue delamination at tape/fabric interfaces. In *AIAA Scitech 2020 Forum*, 1384, 2020.
- [142] C. G. Dávila and C. Bisagni. Fatigue life and damage tolerance of postbuckled composite stiffened structures with indentation damage. *Journal of Composite Materials*, 52(7):931–943, 2018.
- [143] E. Greenhalgh, A. Lewis, R. Bowen, and M. Grassi. Evaluation of toughening concepts at structural features in CFRP-Part I: Stiffener pull-off. *Composites Part A: Applied Science and Manufacturing*, 37(10):1521–1535, 2006.
- [144] Vipul Ranatunga and Stephen B Clay. Cohesive modeling of damage growth in z-pinned laminates under mode-I loading. *Journal of Composite Materials*, 47(26):3269–3283, 2012.
- [145] V. S. Papapetrou, A. Y. Tamijani, and D. Kim. Preliminary wing study of general aviation aircraft with stitched composite panels. *Journal of Aircraft*, 54(2):704–715, 2017.
- [146] V. Ranatunga, S. M. Crampton, and D. Jegley. Impact damage tolerance of composite laminates with through-the-thickness stitches. In *AIAA Scitech 2019 Forum*, 1045. American Institute of Aeronautics and Astronautics Inc, AIAA, 2019.
- [147] D. A Drake, R. W Sullivan, and S. Clay. On the use of a trilinear traction-separation law to represent stitch failure in stitched sandwich composites. *Journal of Sandwich Structures & Materials*, 24(2):1367–1384, 2022.
- [148] N. Subramanian and C. Bisagni. Multiscale damage in co-cured composites - Perspectives from experiments and modelling. *Composites Ingenuity Taking on Challenges in Environment-Energy-Economy*, 3:1479–1492, 2021.
- [149] J. Jumelet. diagNNose: A Library for Neural Activation Analysis. In *Third Black-boxNLP Workshop on Analyzing and Interpreting Neural Networks for NLP*, pages 342–350, 2020.
- [150] E. van Krieken, T. Thanapalasingam, J. M. Tomczak, F. van Harmelen, and A. ten Teije. A-NeSI: A Scalable Approximate Method for Probabilistic Neurosymbolic Inference. 2022.

GLOSSARY

3PB Three-Point Bending.

4PB Four-Point Bending.

4PT Four-Point Twisting.

7PB Seven-Point Bending.

B-K Benzeggagh-Kenane.

CSERR Critical Strain Energy Release Rate.

CSS8 Continuum Solid Shell element.

DCB Double Cantilever Beam.

DIC Digital Image Correlation.

ECT Edge-Crack Torsion.

ENF End-Notched Flexure.

FE Finite Element.

FSP Four-Stringer Panel.

MMB Mixed-Mode Bending.

R-curve Resistance curve.

RSS Residual Sum of Squares.

S4R Conventional Shell element.

SC8R Continuum Shell element.

SSC Single-Stringer Compression.

LIST OF PUBLICATIONS

3. *Kootte, L.J.*, Bisagni, C., Ranatunga, V., Clay, S.B., Dávila, C.G., and Rose, C.A., “Effect of Composite Stiffened Panel Design on Skin-Stringer Separation in Postbuckling”, AIAA Scitech 2021 Forum, 0441, 2021. doi: 10.2514/6.2021-0441
 -  2. *Kootte, L.J.*, and Bisagni, C., “A Methodology to Investigate Skin-Stringer Separation in Postbuckled Composite Stiffened Panels”, AIAA Scitech 2020 Forum, 0477, 2020. doi: 10.2514/6.2020-0477
 1. *Kootte, L.J.*, Bisagni, C., Dávila, C.G., and Ranatunga, V., “Study of Skin-Stringer Separation in Postbuckled Composite Aeronautical Structures”, American Society for Composites 33rd Technical Conference, 1750-1761, 2018. doi: 10.12783/asc33/26048
-  Won a best paper, tool demonstration, or proposal award.

ACKNOWLEDGMENTS

On the last day of my PhD contract a PhD from the new generation asked me: what motivated you to dress up every morning and to come to the office? My answer was: it wasn't the work, but the people I worked with. Everyone mentioned here has contributed either to my work, the project, my well-being and life joy, or to the improvement of the work culture around me. The acknowledgements are long because every one of you mentioned deserves it; I wouldn't have survived the PhD without you. My biggest regrets during the PhD will always be the moments when I skipped vacations with friends, did not go out with colleagues, or did not give the attention to my girlfriend and family that they deserved. For anyone reading this while still doing their PhD, don't be like me, appreciate everyone you care for, deadlines can wait.

First and foremost, I would like to thank Prof. Chiara Bisagni, my promotor and daily supervisor. We have worked intensively together for over five years, and I've grown tremendously under your mentoring. You brought me in contact with many brilliant people, through the project, at conferences, and by taking on other excellent researchers. Although heavily biased, I think you led a group that did exciting research, especially from an experimental point of view, and always with industry relevance. It will be a pity for the university to lose you. Still, I am sure you will thrive even more at your Alma Mater. Hopefully, you will keep fighting to improve diversity and be an example for future female professors.

I would also like to thank my promotor Prof. Christos Kassapoglou. Already at my 2nd bachelor year, you were a major motivator to go into structures. Your lectures and stories from the industry were always captivating. You were always tough and fair, and for students often scary to approach. However, as my promotor, you were always on-point with questioning my work during our yearly meetings. More importantly, you made sure that personal development and well-being were discussed. You even supported me when I was at the lowest point for my motivation at the end of the PhD to finish strong.

I would like to thank the committee members: Bert, Bruno, Carlos, Carol, Chiara, Christos, Rinze and Vipul, for showing their interest in my work and taking the time to read my dissertation carefully. Hopefully, many will follow your example! I am looking forward to all our fun discussions during my PhD defence.

I would also like to thank my project members: Vipul, Carlos, Cheryl, Stephen and Steve. I had the opportunity to present to you my work and progress for over 50 monthly meetings. All of you had a tremendous amount of feedback, which is reflected by the quality and quantity of performed work. Carlos, you were already early on involved in the direction of the research, you showed important research gaps. You were also always available to discuss interesting findings or problems. Vipul, you were always extremely supportive of my work and always did your best to motivate me to keep doing good work. Your interest in my Python tools and how I model showed appreciation for my efforts. Additionally thanks to all other people that contributed to the project: Edgars and Steven

for creating a beautiful design for the adaptive multi-point test equipment. Thank you to Flores for all the numerical work and fun discussions and to Javier for all the experimental work for the industry-manufactured panels.

Kevin, friend, colleague, Kootte and van Dooren consultancy partner, and former housemate, you had a tremendous impact on my PhD. Our office was, from day 1, known as the Dutch-talking office, with an emphasis on talking. PhD is supposedly a lonesome road, but even during Covid a day didn't go by that we didn't share our findings, methods, code, experiences or provide a helping hand in the lab. You would stay with me on Friday evenings to ensure I wasn't alone in the lab. But your most important role was to motivate all of us to participate in the PhD Drinks, Vrijmibo's, Tuesday's jazznights, ASM drinks, or any other reason to socialize and gossip.

The most enjoyable time during the PhD was always when I could work in the lab. Mainly because of all the technical and emotional support I received there from Gertjan, Berthil, Dave, Alexander, Victor, Fred, Chantal, Johan, Johan and Misja. Taking time to drink coffee with Gertjan, Ana, and Linda led to a friendship where we still enjoy our coffee even after leaving the faculty. This experience made me feel comfortable and at home in the lab and showed me the importance of work relations. That's why from the first working days of Dave and Alexander, we immediately clicked. During my difficult times, you two were always there to pause your work and talk to me to see how I was doing.

I want to thank my PhD colleagues for contributing to my work and for all the fun times we had. But also a sincere apology to all my officemates, Kevin, Bas, Arne, Jens, Merjem, Andres, Allesandro and Carmen, for me never being quiet. I will miss all the fun and discussions we had. Thank you to the cool kidz office: Ines, Marta, Javier and Yuqian for mentoring me throughout the PhD. To the other offices for the engaging discussions during lunch: Giorgio, Panos, Natalia, Srikanth, Hauke, Victor, Siddharth, Alf. And thank you to the PhD's downstairs, despite the rivalry between our sections, I always enjoyed our talks: Camila, Ioannis, Davide, Chantal. A special thanks to Eva, for being a good friend and listener; you are an example for the new generation of PhDs, always speaking up for injustice. We are not PhD students nor candidates; we are researchers and employees and should be treated as such.

Additionally, I appreciated the funniest room in the department full of Post-Docs and researchers: Javier, Antonio, Nithya, Jing, Xavier, Alex. You showed us that the future after the PhD is bright and full of enjoyment! A special thank you for Javier, who has been the light of the department; Always joking, yet always serious. The day hasn't started or ended before getting a hug from you. We've spent many days in the lab working from opening to closing and many more having fun and drinking coffee. You'll be an amazing ass-prof!

Most of my personal development occurred as part of the PhD council with Agnes, Bieke, Christoph, Colin, Dora, Gitte, Pieter-Jan and Sven. We've organized amazing events and always had a lot of fun. Together with the amazing aerospace graduate school, Laurike and Piero, we've improved the working conditions for the PhDs. An additional thank you to our dean Henri for taking our issues seriously and his proactiveness in the continuous improvements needed for the future generations of PhDs.

A thank you to my colleagues of ASM: Laura, Sergio, Roeland, Bianca, Boyang, Daniel, Julien, Jurij, Saullo, Eddy, George, Xueri, Santiago, Calvin, Sofia and many more. Roeland,

you were an amazing section leader; when it is time for a new era, I hope you will lead ASM and bring them back to great heights. Sergio, you are an amazing researcher and the funniest lecturer. Julien, thank you for all the lovely cakes, the restaurant recommendations, and for helping me to get the best internship at ATG, where I learned the skills that is the foundation of this dissertation. Prof. Rothwell, Alan, your help in writing, positive feedback, and interest in my work motivated me to finish my draft. Last and most, I would like to thank Laura, the MVP of our department, it isn't the same without you. You've cared for all of us, made sure we were okay and supported us if not. You taught us to enjoy our beers and not talk shop.

Thank you to all my friends from high school: Marc, Jaap, Emile, Joris, Olaf, Jurriaan, Lennart and Nino, and since elementary school: Martin; Who would've expected us 20 years later to be PhD colleagues. Jaap and Emile, sharing our different experiences on the PhD were always insightful, many respect for all the actual work you guys do on AI[149, 150]. Joris, Vampire-Ramen nights were the perfect distraction away from the PhD. Marc, thank you for always being available on-call for meaningful advice.

Willem, Thijs, Ilja, Davey, Bram and Jaap, starting my PhD meant leaving the house with you guys, but luckily we are still very close. Hopefully watching shows and eating pompelkoren will be around for another couple of years.

Thank you to my friends from my bachelor's: Tom, Tijmen, Joost en Aalok, who've all motivated me to work hard during my studies, which laid the foundation of my PhD. As well as to my friends from my masters: Guyonne, Bram, Katleen and Lander.

I would like to share my greatest appreciation to my strong and loving family, my parents, Gerrit and Jeannie, and brothers and sister Bob, Marieke and Bart as well as their partners Nienke and Roos. They've always pushed me and were ever so supportive. As the youngest of the bunch, you all were and will always be a great inspiration and I couldn't be more prouder.

All my love and gratefulness to Linda. Spending time with your family, Jos, Lenie and Joeri was always heart-warming and relaxing. Linda and I have been through the most difficult years together and came out stronger than ever. Your hands were the best for DIC calibration and for being the editor of all my written reports and presentations. You always cared for my mental health and made sure that I actually worked the hours I was paid for, evening and weekends are to relax and to spend with friends and loved ones.

BIOGRAPHICAL NOTE

Lucas Johan Kootte was born on March 26 1995 in Breda, Netherlands. After finishing grammar school at the Stedelijk Gymnasium Breda, he followed his brother and sister to Delft. Here he spent almost 10 years, The first 5 years as a student during the bachelor's and master's and after as an employee during the 4 years of PhD research.

During his bachelor, his interest in the course of structural analysis led him to join the Human Power Team as a structural engineer. Here the basis of design, modelling, manufacturing and testing of composites started. A composite faired recumbent bicycle was built, capable of exceeding 100+ kph purely on manpower, which was raced at Battle Mountain, USA. On the same day of coming back from the US, a following flight was taken to the UK for a semester abroad at Coventry University to learn about finance and corporate investments.

During the master's in aerospace structures and computational mechanics, he joined ATG Europe as part of the internship. Here he worked on the development of Python scripts for the automising input and output for Finite Element software FEMAP.

The theoretical knowledge from the master's courses, the practical experience in composite manufacturing, and the passion for automation are combined in this thesis. During the PhD, Luc joins the Faculty and University PhD Council, to represent the needs of his colleagues.

